Hoist the flag:
A boundary rip current case study on swimmer safety in the Scheveningen harbour area

ASOR MUSTAFA

Cover photo:
The Great Wave off Kanagawa by Katsushika Hokusai. Retrieved from https://en.wikipedia.org/wiki/The_Great_Wave_off_Kanagawa#/media/File:Tsunami_by_hokusai_19th_century.jpg

Hoist the flag: A boundary rip current case study on swimmer safety in the Scheveningen harbour area

by

Asor Mustafa

in partial fulfillment of the requirements for the degree of Master of Science in Hydraulic Engineering at the Delft University of Technology, to be defended publicly on Monday August 26, 2021 at 12:00 AM.

Graduation committee:

Dr. ir. Matthieu de Schipper	TU Delft
Dr. ir. Ad Reniers	TU Delft
Dr. ir. Marion Tissier	TU Delft
ir. Roeland de Zeeuw	Shore Monitoring

Preface

With this report my studies at the TU Delft come to an end. It was a journey during which I learnt a lot and was able to meet some wonderful people. Although the specialization I chose to graduate in is Coastal Engineering, I also enjoyed courses focusing on River Engineering and other subjects offered at the faculty.

During the whole graduation process, I had guidance from a great committee, which provided me with much valuable input and were always prepared to discuss questions or difficulties I was facing. I would like to thank my daily supervisor Matthieu de Schipper for his help with my many questions. Ad Reniers taught me a lot on modelling and sparked my interest on the subject. During committee meetings Marion was always able to help me refocus on the problem at hand. This proved to be a valuable lesson. Lastly, I would like to thank Roeland de Zeeuw. Unfortunately performing field measurements was not possible, but the questions on the model you posed required me to think critically on the subject.

Finally, I would like to thank my family and friends for their support and patience during this ordeal of sorts.

Asor Mustafa
Delft, August 2021

Abstract

Each year several fatalities due to rip currents are reported in the Netherlands. One of these accidents was during May 11th in 2020 near the Scheveningen harbour, were several surfers lost their lives. During the hydrodynamic and meteorological accident were quite severe, with a significant wave height of 3.0m and wind speeds of 11 m/s, which is likely to have resulted in a boundary rip at the northern mole. On top of that extraordinary amounts of sea foam amassed at the northern harbour mole, disorienting anyone who got trapped in the area. It is likely that due to the wind and wave conditions and the resulting rip current it was near impossible for the surfers to exit the vicinity of the mole, especially with thick layer of foam.
In order to obtain insight in the rip current behaviour at the Scheveningen harbour and the influence thereon by tide, waves and wind this research has been set up, with the research question posed as follows:

What combinations of wind-waves, tide and wind lead to offshore boundary rip transport and what combinations lead to retentive boundary rip transport at the Scheveningen harbour moles?

The Scheveningen harbour area was modelled in Delft3D. Wind and wave conditions to be used were used on the basis of frequency of occurrence, and the tidal motion was obtained from the Delft Dashboard software. Bathymetric data was obtained from the JARKUS measurements, which is a yearly measurement campaign of the Dutch shoreline by the Dutch ministry of infrastructure. The model was set to output Lagrangian velocity fields.
In order to check the model behaviour on the several forcing types it was first subjected to each forcing individually. It was found during this stage that the model was best suitable for with a significant wave height of at least 1.0m as otherwise the grid would be too coarse to properly account for wave breaking. Additionally, Neumann boundaries were found to have the best performance with respect to boundary perturbations.

After an assessment in which the model outputs were checked against findings from literature, the model was subjected to individual wind, wave and tidal conditions and to combinations thereof, which yielded flow fields for every run. Per forcing condition transport patterns were obtained by releasing virtual drifters in the resulting flow fields. To classify the transport pattern three types of transport patterns have been defined: retention, exit and overshoot. In previous research retention is defined as particles remaining inside the surf zone and exits as particles exiting the surf zone. In this study however the offshore extent of northern mole tip was used as divisive line between these two transport types. Overshoots are defined as drifters that travel south of the northern mole as to make a distinction between mainly offshore directed transport and particles entering or bypassing the harbour.
Detecting rips inside the model was done by measuring the flow velocity in the vicinity of the breakwater. At selected points in time this yielded velocities in the selected grid cells. To account for the spatial variation in velocity a rip is defined as having a median velocity of 0.1 m/s and a potentially hazardous rip having a velocity of 0.3 m/s.
Assessment of the influence of wind, waves and tide on rip current intensity was performed by comparing the model results from a combined run with the rip velocities obtained by superimposing rip velocities per individual forcing condition. Lastly, the model was run with conditions resembling the aforementioned accident as to check whether the model was able hindcast this situation.

Results of single forcing showed that rips during wind, waves and tide. However, the only single forcing mechanism which formed rips with velocities of 0.3 m/s and higher was found to be waves in the range of 30

to 70 degrees relative to shore normal with a significant wave height of at least 2.0m. These conditions were also found to yield most exits and overshoots. Runs with multiple conditions showed that the highest rip velocities were found for forcing from 30 to 70 degrees relative to shore normal and spring tide. Spring tide also showed a significant amount of exits during forcing from southern directions, even though rip velocities were relatively low during these cases.
Comparison of runs with single conditions and runs with multiple conditions showed that the strongest component is wave forcing. The tidal current was found to be important as well as it either strengthens or weakens the longshore current which feeds the rips. Wind forcing seems to play a minor role in forcing the longshore currents. The combination of single runs which best approximated the full model were the superimposed tide and waves when the tidal water level was below mean water level.
As for hindcasting the accident drifter trajectories were found to end up at different locations than were the victims were found. Reasons for this are likely the lack of windage affecting virtual drifters as well as the fact that drifters are practically unable to get stuck in the harbour mole due to its spatial interpolation method.

In conclusion, the main wind and wave directions found to lead to offshore directed rip transport come from 30-70 degrees relative to shore normal. Due to tidal currents overshoots are most likely to occur during low water and exits during low water. As for the other forcing directions rip currents also occur, especially during spring tide when the tidal current is strongest. Retentive rips also occur, mainly when the wind-wave forcing comes from -70 to 0 degrees relative to shore normal, although rips occur less frequently in this range.

Contents

List of Figures

List of Tables

Symbols

Symbol	Description	Unit
a	Wave amplitude	m
B	Frictional stress	$\mathrm{N\,m^{-2}}$
C	Chézy coefficient	$\mathrm{m^{1/2}s^{-1}}$
c	Wave celerity	$\mathrm{m\,s^{-1}}$
c_g	Wave group celerity	$\mathrm{m\,s^{-1}}$
c_0	Wave group celerity, deep water	$\mathrm{m\,s^{-1}}$
d	Water depth	$\mathrm{m\,s^{-1}}$
E	Wave energy	$\mathrm{N\,m^{-1}}$
F	Wave energy flux	$\mathrm{N\,s^{-1}}$
g	Gravitational acceleration	$\mathrm{m\,s^{-2}}$
h	Water surface elevation	$\mathrm{m\,s^{-1}}$
H	Wave height	m
k	Wave number	$\mathrm{rad\,m^{-1}}$
n	Manning coefficient	$\mathrm{sm^{-1/3}}$
s	Water level slope	$\mathrm{m\,m^{-1}}$
S	Wave momentum flux	$\mathrm{N\,m^{-1}}$
t	Time	s
u	Velocity in cross shore direction	$\mathrm{m\,s^{-1}}$
v	Velocity in longshore direction	$\mathrm{m\,s^{-1}}$
x	Position in cross shore direction	m
y	Position in longshore direction	m
ζ	Water level	m
θ	Wave angle of incidence	$^\circ$
θ_0	Wave angle of incidence, deep water	$^\circ$
ρ	Density	$\mathrm{kg\,m^{-3}}$
τ	Wave stress	$\mathrm{N\,m^{-2}}$
$\bar{\tau}_b$	Bottom friction	$\mathrm{N\,m^{-2}}$
ω	Angular velocity	$\mathrm{rad\,s^{-1}}$

1. Introduction

1.1 Problem Description and Motivation

In the Netherlands alone each year several casualties are reported due to rip currents. Typically rip currents have velocities of 0.5 m/s and higher (Castelle, Scott, Brander, & McCarroll, 2016). With such velocities it is often impossible for an adult human to swim against the current. People caught in a rip often panic and try to swim against the current possibly leading to exhaustion, and in worst case scenarios to drowning.
Most of these rip currents occur on sandy beaches and their occurrence is dependent on the bathymetry and the hydrodynamic conditions. This can make them hard to predict as both these features change over time and space. For example, after a storm the bathymetry is more alongshore uniform and existing bars are moved to deeper waters. After the storm has passed the bathymetry is reshaped by wave action and currents redistributing sediments, creating an irregular bathymetry and moving the bar back to shore (R. A. Dalrymple et al., 2010).

Other rip currents are the effect of the interaction between waves and geological features or human built structures (e.g. headlands, harbour moles and groynes). Such features act as a boundary, hence they are classified as boundary controlled rip currents. These boundary induced rip currents can be divided into deflection rips and shadow rips, of which deflection rips are sometimes referred to as headland rips as they occur near headlands, or topographic rips (Castelle et al., 2016). The difference between the two types lies in the forcing mechanisms. Shadow rips occur at the down-wave side of a structure and are driven by a difference in wave energy. At the shadow side of the structure there is a limited penetration of wave energy, which results in a difference of wave setup and hence an alongshore water level gradient. As a result a flow occurs to compensate for the difference in pressure which forms the rip current R. A. Dalrymple et al. (2010). Deflection rips however occur at the up-wave side. As the waves move toward the shore under an angle they break and induce an alongshore current. When this current reaches the structure the water level rises. With this rise of water level comes a pressure gradient in cross-shore direction deflecting the flow offshore and forming the deflection rip (R. A. Dalrymple et al., 2010). Such a deflection rip may carry far outside the surf zone, possibly several times the width of the surf zone (Mouragues et al., 2020).

The combination of the high exit rates and flow velocities makes boundary rips possibly a dangerous rip type for both swimmers and surfers. Although other rip types also pose a potential threat to swimmer safety, the difference between boundary rips with other rip types lies mainly in the flow pattern that occurs. Rips that are dependent on mainly the hydrodynamic conditions and bathymetry, or a combination thereof, often behave like a rip cell. With cell-like behaviour suspended matter is more likely to be retained inside the surf zone.
As there are many beaches with impermeable structures the formation of boundary rips is inevitable. The danger of these rips was realized again on may 11^{th} 2020 when five surfers lost their lives at the northern harbour moles (Trouw, 2020). The potential of this work to gain more insight and spread this among the wider public is the main motivation of this work. With more insight on the processes that drive these currents it may be possible to predict the type of current and its transport pattern. Additionally, if the predictions are reliable enough there is even the possibility of developing tools that are able to inform people better on the hazardous situations that may occur on this place. Also it may aid the Scheveningen lifeguard association helping people in need.
Another outlook, outside of the scope of this thesis, is on the effect of impermeable structures on sediment

retention.

1.2 Research Objective and Scope

The goal of this research is to identify and quantify the forcing mechanisms influencing boundary rip current behaviour. From literature it is for example known that during obliquely incident high waves deflection rips are likely to occur at hard structures/geographic features (Castelle et al., 2016; Mouragues et al., 2020; Pattiaratchi, Olsson, Hetzel, & Lowe, 2009). There are indications that the wave height may be of influence on the formation of either a circulation cell or an offshore directed jet (Murray, 1974; Scott, Austin, Masselink, & Russell, 2015). What is not known however is the influence of these forcing mechanisms on the rip current pattern and the consequent transport pattern. Here the transport pattern is defined as the path traveled by an object in the flow field.
To the author's knowledge however it is not yet known what the threshold of the wave height is to induce rip transport. Also it is not known what the influence from the tide and wind is on rip transport. Additionally the relative importance of these three factors as well as the structure characteristics are to be investigated, including the effects they have on each other.

The scope for this research is mainly focused on the Scheveningen harbour area in the direct vicinity of the harbour moles as this is a location with ample beach recreation. As for rip currents the focus lies on both shadow rips and deflection rips which are generated by the interaction of wind-waves, tide and wind with the harbour moles.

1.3 Research Question

The main research question in this study is:

What combinations of wind-waves, tide and wind lead to offshore boundary rip transport and what combinations lead to retentive boundary rip transport at the Scheveningen harbour moles?

The sub questions supporting the research question are:

I Which factors are known to be involved in boundary rip formation?

II What are the known conceptual models for deflection rips and shadow rips?

III How can wind-waves, tide and wind and a combination thereof at the Scheveningen harbour moles be modeled in Delft3D?

IV What are the relative contributions of these factors in each boundary rip transport configuration?

V Which configurations of factors lead to a circular rip pattern and which to offshore directed flow?

VI What is the relation between the rip flow pattern and the transport pattern?

1.4 Methodology

In this section the methodology will be presented. The methodology is used to describe the modus operandi and the choices made in the process.

1.4.1 Literature Review

The first goal in obtaining the research goal is the literature review. Here the factors involved, both expected and observed will be identified. Potentially rip currents can be driven by wind-waves, tide and wind. Wind-waves are known to generate boundary rips and the tide is a known amplification factor of the rip velocity. Wind driven longshore currents have not been reported as a direct factor in rip current formation although they naturally influence wind-waves. It is known however that the wind is an important factor in the behaviour of rips at the Scheveningen harbour moles.
Therefore one of the focal points of the literature review is to identify the key hydrodynamic conditions that occur due to wind-waves, tide, wind and structures such that these can be tested in the Delft3D model and which combinations of these gives either an offshore directed transport pattern or a circular transport pattern.

The second goal from the literature review is the investigation of known conceptual models for boundary rips and transport pattern these models predict. Influence of wind-waves, tide, wind and structure characteristics under consideration will then be checked against the existing conceptual models and possibly integrated. The resulting conceptual model gives a basis against which the outcomes from the (numerical) Delft3D model can be analyzed. Additionally this part of the literature review gives a theoretical framework contextualizing the outcomes from the field experiment at the Scheveningen harbour moles.

The third goal of the literature study is to review prior modeling efforts in Delft3D of boundary rips. This gives a perspective on the possibilities and limitations of the model.

1.4.2 Modeling Stage

The next stage is the modeling stage. A model of the Scheveningen harbour and a small portion of its surroundings will be constructed. The most important static features in this model are:

- The bathymetry
- The harbour moles

The time scale of bathymetric changes with respect to the time scale of the hydrodynamic forcing is large. Therefore the bathymetry will be assumed to remain constant, even though small variations might occur in reality. The harbour moles will also be modeled as static as only little damage may occur during the conditions applied in the model which will not alter the general behaviour of the structure.
In this model several scenario's with only one variable factor will be carried out to validate the program, to identify whether or not a rip current occurs and which transport pattern it yields. Once the behaviour per factor is known combinations of different factors can be made to test the relative importance and to identify the combined effects on boundary rip formation.

1.4.3 Data Acquisition

Datasets on the wave characteristics, tidal movement and wind measurements will be obtained from `https://noos.matroos.rws.nl/`, `https://getij.rws.nl/` and `https://www.meteoblue.com/nl/weer` respectively. These datasets will be used to validate the model and set up hydrodynamic and meteorological conditions.

1.4.4 Theoretical Model Assessment

Model assessment will be performed by testing several scenarios in the Delft3D model itself. There is no exact data available for rip currents in the location under consideration, but forcing by for example the tide can be checked against findings from literature. Additionally the model will be checked on its consistency and behaviour, such as overall flow patterns and boundary behaviour.
Furthermore literature will be checked for prior modeling efforts in Delft3D. This should provide some preliminary insight in the possibilities of modeling rip currents in Delft3D and similar software packages. The validation of the model should thus give insight in its strong and weak points. With the obtained results the model can be adjusted such that it can provide more accurate predictions.

1.5 Potential Outlook and Work Plan

The potential outlook of this research is a broader understanding of boundary rips in general as well as deeper insight in the factors which affect their transport behaviours. As the research is focused on the Scheveningen harbour area it may yield useful, or even vital information for a broader public including surfers and swimmers. With further knowledge on the behaviour of boundary rips at the harbour moles in several conditions people may be taught what conditions to be aware of and what to do when in trouble. It may also provide the lifeguard with additional information on how to act under given circumstances.

2. Literature Review

In this chapter the existing literature on rip currents and their interaction with impermeable structures and geological features will be discussed, beginning with the two types of rip currents that are associated with such impermeable structures. Following this a basic model for the alongshore flow and structure interaction will be investigated. Thereafter follows a review of the known factors influencing the formation and behaviour boundary rips and an evaluation of the current modeling knowledge and possibilities of rips and nearshore currents in Delft3D. The literature review concludes with the current knowledge gap and the answer to sub questions I and II.

2.1 Hydrological and Metereological Conditions at the Dutch Coast

The Dutch coast is located at the North Sea. The North Sea is a Shelf Sea, meaning that it is relatively shallow (Emeis et al., 2015). Tidal motion is mainly due to the M2 and S2 tidal components Bosboom and Stive (2015). Other Astronomical components are also present but have only a small impact on the tidal motion.
Tidal propagation in the North Sea is characterized by the interaction between the geostrophic balance, which is the balance between the Coriolis acceleration a water level gradient (Bosboom & Stive, 2015, p. 130):

$$fv = g\frac{\partial \zeta}{\partial x} \tag{2.1}$$

In which f the Coriolis acceleration and v the alongshore velocity. The geostrophic balance is of importance because it gives rise to a Kelvin wave and an amphidromic point. This leads to a wave that in the North Sea the tidal wave enters the basin in the north and makes an anti-clockwise rotation until it leaves the basin, again in the north. The amphidromic point is the point in which the tidal amplitude is zero and increases with distance. Several of these points are present in the North Sea due to reflection of Kelvin waves, but the most important one for the tidal range at the Scheveningen Harbour is the southern amphidromic point (Bosboom & Stive, 2015, p. 128). A schematization of the North Sea amphidromic points and tidal movement can be found in fig. 2.1a.
The tidal range around Scheveningen is about 2m during spring tide and during neap tide it is around 1.2m. Flow velocities are of order 0.5 m/s, but differ between spring and neap tides. Spring tides show stronger longshore flow velocities as due to the increased differences in water levels between ebb and flood. Neap tide shows relatively low flow velocities. This means that depending on the tide influences of waves, wind and tide may differ substantially between neap and spring tide.

The Dutch coast lies in a storm wave environment (Bosboom & Stive, 2015, p. 148). This means that the wave climate mainly consists of short wind waves from the South West and West. These waves are generated by storms relatively close to the coast and are characterized by their small wave lengths, wave periods between of 5-6 seconds, and have large directional spreading de Schipper et al. (2016). Swell waves also occur from the North and North West, but less often. Such waves have a small directional spreading and large wave length and period. The occurrence of waves at the dutch coast can be found in the wave rose in fig. 2.2

Wind conditions are dominated by landward winds, mainly varying from Southern to Western direction.

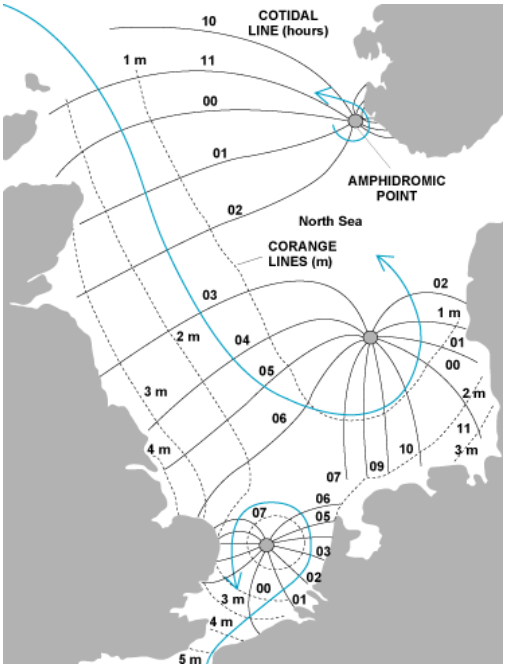

(a) Tidal motion through the North Sea Basin including amphidromic points. From Kvale (2009), modified from D. Dalrymple (1992).

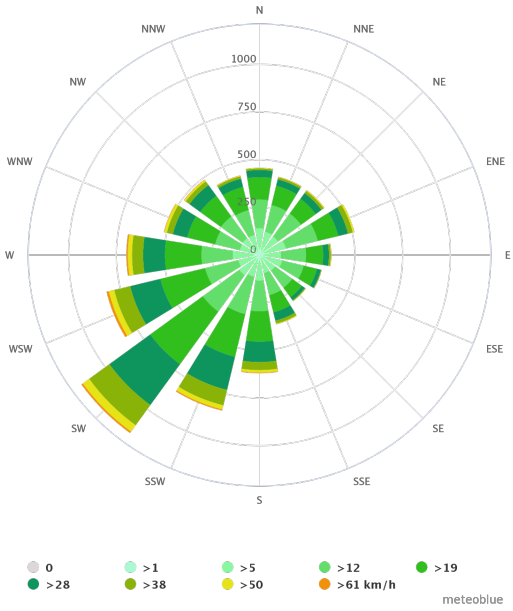

(b) Wind rose at Scheveningen with the wind direction, wind velocity (km/h) and the amount of hours per direction. From Meteoblue.

Figure 2.1: North Sea amphidromic points and wind distribution at Scheveningen

Mostly these winds are between 1.5 and 10 m/s, but during storm conditions wind speeds over 20 m/s are measured. These extreme conditions mainly originate from the South West (KNMI, n.d.).

2.2 Rip Currents near Structures

Three different kinds of rip currents near structures are known. These are headland rips, deflection rips and shadow rips, where deflection and headland rips are very similar but differ in scale. The main focus of this study however is on deflection rips and shadow rips.
Shadow rips mainly occur when incoming waves are slightly oblique (Scott et al., 2015). If the wave incidence deviates further from shore normal the rip is more likely to become a deflection rip. From the measurements at a groyned coast it followed that the deflection type was the most dominant rip type. When both types were present in the study performed by Scott et al. (2015) the effects of the shadow rip were hardly noticeable due to the deflection rip exerting a much stronger current than the shadow rip. Basic configurations on shadow and deflection rips can be found in fig. 2.3.

2.2.1 Deflection Rips

Deflection rips occur at the up-wave side of an impermeable structure (fig. 2.3a). Such rips are formed when a longshore current reaches an impermeable structure and gets deflected offshore. According to R. A. Dalrymple et al. (2010) a deflection rip is driven by a water level gradient which forms due to the longshore current hitting the structure. This water level gradient then feeds a current directed along the structure. Another driver of longshore currents can be the longshore variability of wave energy as suggested by Scott et al. (2015).
The velocities and amount of deflection are dependent on the length of the structure with respect to the width of the surf-zone, structure-structure spacing, wind-wave characteristics, tide, wind speed and wind direction (Castelle et al., 2016). As Deflection rips are often associated with strong currents and high exit

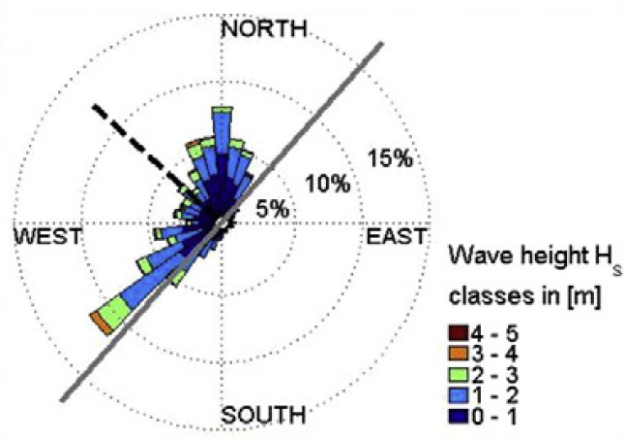

Figure 2.2: Offshore wave rose from the Europlatform measurement location, from de Schipper et al. (2016)

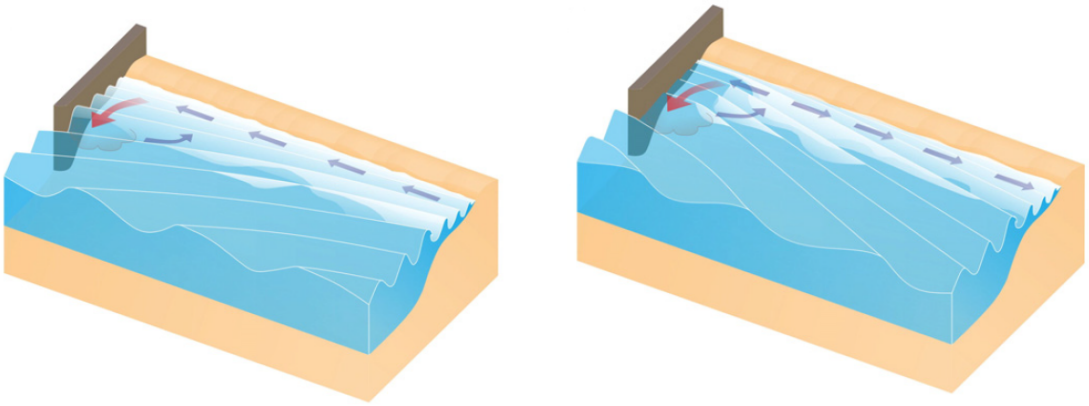

(a) Deflection rip

(b) Shadow rip

Figure 2.3: Boundary rip current patterns. From R. A. Dalrymple et al. (2010). a) Deflection rip type: this rip type is caused by the deflection of the longshore current, which is directed towards the structure. b) Shadow rip type: wave shadowing in the lee of a structure results in a pressure gradient which drives a current. Longshore current is directed away from the structure

rates this may indicate seaward transport patterns.

2.2.2 Shadow Rips

Shadow rips form at the lee side of a structure. Due to the difference in wave set-up between the shadow zone and the rest of the surf zone a set-up gradient forms. This water level gradient acts as a pressure gradient which forces a flow in the direction of the structure Scott et al. (2015). A mathematical description explaining such currents is given by Longuet-Higgins and Stewart (1964) theory of radiation stresses. This mechanism is discussed in section 2.3.1. Pattiaratchi et al. (2009) found from field measurements that the intensity of Shadow rips is mainly dependent on the spreading of the wave field, the angle of wave incidence and the directional spreading of the wave field (Jackson & Short, 2015).
The main differences with the deflection type rips are the current strengths, current patterns and exit rates. Scott et al. (2015) found that Shadow rips have much lower exit rates than Deflection rips. He also found that the current pattern is mostly circulating. This may is a strong indication of the transport pattern for Shadow rips also being circulatory.

2.3 Factors and Processes Influencing Rip Behaviour

Several factors and processes are of influence in rip formation and rip behaviour. In this section the physical processes and other factors influencing the rip behaviour will be discussed. These are waves, tide, wind and structure characteristics.

2.3.1 Waves

Waves are the primary forcing mechanism for both deflection and shadow rip formation. A longshore current can either be generated by a obliquely incident waves or longshore differences in wave energy. Longuet-Higgins (1970a) described the longshore current for a longshore uniform coast with obliquely incident waves in terms of Momentum conservation. His reason for choosing the momentum balance was that energy dissipates due to wave breaking whereas momentum does not. The Momentum flux driving an alongshore current is defined by:

$$S_{xy} = F_y \left(\frac{sin\theta_0}{c_0} \right) \tag{2.2}$$

In this equation F_y is the energy flux in alongshore direction, c_0 the deep water wave celerity and θ_0 the deep water angle of incidence with respect to the coast. The energy flux is defined as:

$$F_y = \frac{1}{2} E_0 c_0 cos\left(\theta_0\right) \tag{2.3}$$

With the local wave energy given by:

$$E = \frac{1}{2} \rho g a^2 \tag{2.4}$$

Where rho the density, g the gravitational acceleration and a the amplitude of the incoming waves. The longshore current can then be fully described using the equation of motion proposed by Longuet-Higgins (1970b) as given by eq. 2.5.

$$\tau_y + \frac{\partial}{\partial x} \left(\mu h \frac{\partial v}{\partial x} \right) - \bar{\tau}_b = 0 \tag{2.5}$$

In which τ_y the longshore radiation stress per unit area, μ the horizontal eddy viscosity, h the local depth, v the longshore velocity and $\bar{\tau}_b$ the mean bottom friction. In eq. 2.5 the horizontal eddy viscosity determines how much of the momentum is spread out over the surf zone.
Currents induced by the physical process as described in eq. 2.5 are linked to the formation of deflection rips, which are oftentimes stronger than shadow rips. An estimate of the longshore flow velocity can be obtained by simplifying the equation of motion. A simplification of eq. 2.5 obtained by omitting horizontal mixing yields a momentum balance with only the longshore radiation stress and the longshore bottom friction:

$$\tau_y - \tau_b = 0 \tag{2.6}$$

This simplified equation results in the following equation for the mean longshore current velocity inside the surf zone:

$$\bar{v} = \frac{h}{h_b} \times \begin{cases} v_0 & h < h_b \\ 0 & h > h_b \end{cases} \tag{2.7}$$

With:

$$v_0 = \frac{5\pi\alpha}{C} s \sin\theta_b \sqrt{g h_b} \tag{2.8}$$

In which C a friction coefficient of $\mathcal{O}(0.01)$, α a parameter describing the wave amplitude for a given depth by $a = \alpha h$ with a value between 0.3-0.6, h_b the depth at the edge of the surf zone, s the surface level gradient in cross shore direction and θ_b the wave angle of incidence at the edge of the surf zone. Equation 2.7 allows for very crude estimate of the mean velocity. The problem however is that in reality mixing takes place in the surf zone. A comparison between the velocity profiles can be found in fig. 2.4

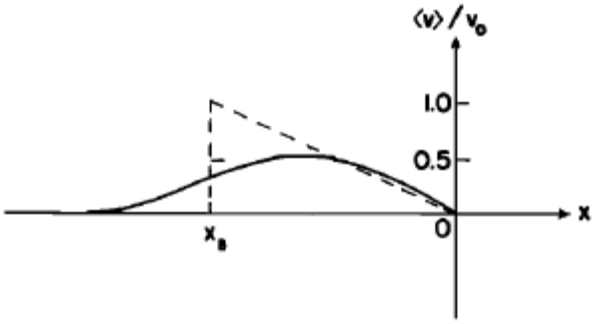

Figure 2.4: Longshore mean velocity profile with (full line) and without (dotted line) horizontal mixing of momentum. From Longuet-Higgins (1970a).

From fig. 2.6 it is clear that such an incontinuity at the cannot take place, meaning that at least some horizontal mixing of momentum takes place within the surf zone. (Longuet-Higgins, 1970b) used dimensionless parameters for the velocity, mixing and distance, V, P and X respectively to describe the longshore velocities including horizontal mixing. Equation 2.5 is then rewritten to

$$P\frac{\partial}{\partial X}\left(X^{\frac{5}{2}}\frac{\partial V}{\partial X}\right) - X^{\frac{1}{1}}V = \begin{cases} -X^{\frac{3}{2}} & 0 < X < 1 \\ 0 & X > 1 \end{cases} \tag{2.9}$$

With the parameters defined as:

$$\begin{aligned} V &= \frac{v}{v_0} \\ X &= \frac{x}{x_b} \\ P &= \frac{\pi}{2}\frac{sN}{\alpha C} \end{aligned} \tag{2.10}$$

In which x the distance from the shore, x_b the distance of the breaker line and N a dimensionless constant. Solving eq. 2.10 results in a mean dimensionless flow velocity of:

$$\bar{V} = \begin{cases} \frac{B_1}{p_1+1} + \frac{A}{2} & P \neq 0.4 \\ \frac{55}{196} & P = 0.4 \end{cases} \tag{2.11}$$

For a maximum flow velocity is found:

$$V_{max} = \left(1 - \frac{1}{p_1}\right) A X_{max} \tag{2.12}$$

With the location of the maximum defined as:

$$X_{max} = \left(\frac{p_1 - p_2}{p_1\left(1 - p_2\right)}\right)^{\frac{1}{p_1}-1} \tag{2.13}$$

With non-dimensional parameters A, B_1, p_1 and p_2. The three parameters are dependent on P as follows:

$$\begin{cases} A & = \frac{1}{1-0.4P} \\ p_1 & = 0.75 + \left(0.5625 + \frac{1}{P}\right)^{\frac{1}{2}} \\ p_2 & = 0.75 - \left(0.5625 + \frac{1}{P}\right)^{\frac{1}{2}} \\ B_1 & = \left(P\left(1 - p_1\right)\left(p_1 - p_2\right)\right)^{-1} \end{cases}$$

Table 2.1: Behaviour of dimensionless parameters on a varying value of P. From Longuet-Higgins (1970b).

$\log_{10}P$	V_B	$\langle V \rangle$	$V_{\max}$	X_m
$-\infty$	0.5000	0.5000	1.0000	1.0000
−3.0	0.4735	0.4847	0.8835	0.9108
−2.5	0.4544	0.4733	0.8254	0.8699
−2.0	0.4233	0.4542	0.7456	0.8148
−1.5	0.3754	0.4230	0.6422	0.7422
−1.0	0.3077	0.3736	0.5173	0.6466
−0.5	0.2226	0.2992	0.3786	0.5198
0.0	0.1333	0.2000	0.2400	0.3600
0.5	0.0628	0.1024	0.1246	0.1984
1.0	0.0240	0.0408	0.0524	0.0861
1.5	0.0081	0.0141	0.0191	0.0316
2.0	0.0026	0.0046	0.0064	0.0107

Longuet-Higgins (1970b) showed the dependence of the flow velocity on the mixing length by taking extreme values for P. Doing so results in the values as shown in table 2.1 from Longuet-Higgins (1970b).
From table 2.1 it is clear that for very low values of the mixing parameter P there is less distribution of Momentum over the surf zone. Increasing this parameter results in the spreading of Momentum over the surf zone and therefore lowers the velocity at the breaker line, the mean velocity and the maximum velocity. It also changes the location of the maximum velocity shoreward. A clear depiction of the the cross shore velocity profile for different values of the mixing parameter can be found in fig. 2.5.

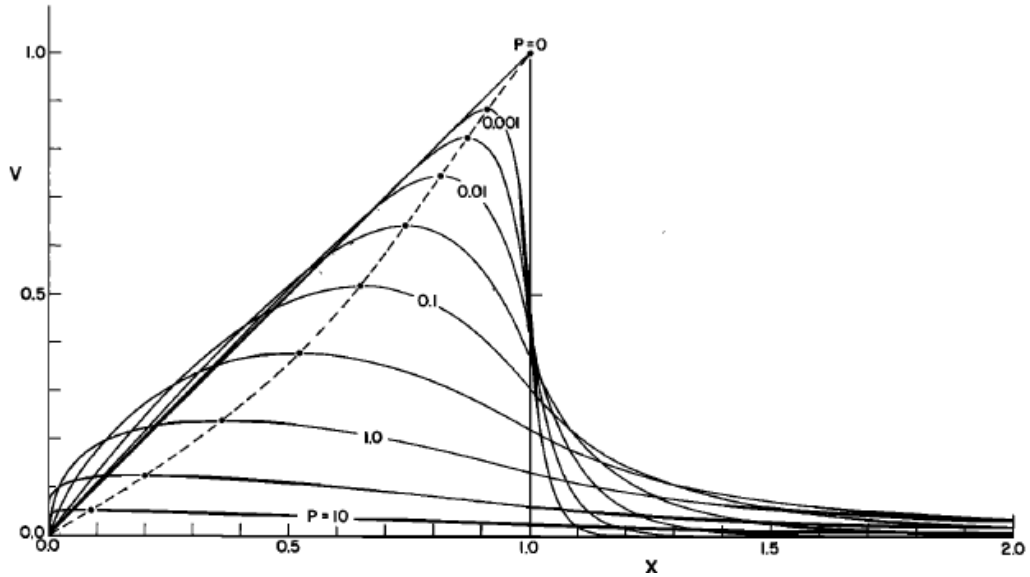

Figure 2.5: Cross shore velocity profile for varying values of P. From (Longuet-Higgins, 1970b).

As seen in fig. 2.4 and fig. 2.5 for P=0 there is no mixing, resulting in a triangular profile. Such a discontinuity in the cross shore flow velocity profile is physically impossible as well as there being no distribution of Momentum over the rest of the surf zone. Increasing the mixing parameter shows more reasonable behaviour:

even for very low values of P there is no longer a discontinuity at the breaker line.
Looking at the influence of mixing on the cross shore velocity from a physical point of view the behaviour in fig. 2.5 seems plausible. First, as momentum is distributed in cross shore direction this means that the velocity must be slightly lower than in the case without momentum distribution. Second, in order to account for continuity at the border of the surf zone it is physically impossible for the maximum velocity to be at the edge of the surf zone. Additionally, the waves breaking at the edge of the surf zone are only the largest, which is a relatively small portion with respect to the rest of the incoming waves. An illustration of the nearshore wave height probability density function is given in fig. 2.6. It shows that the probability of the largest waves, i.e. the waves at the edge of the surf zone is, is smaller than the probability of the smaller waves. This means that the larger part must break within the surf zone, hence the maximum longshore velocity must also be inside the surf zone.

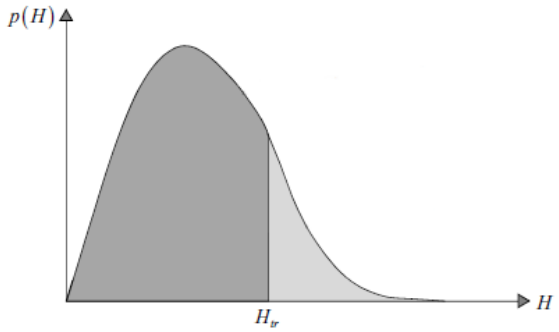

Figure 2.6: Form of the probability density function of nearshore wave heights, from Holthuijsen (2009, p.73). Due to wave transformation the tail of the probability density function (light grey) is no longer of the Rayleigh distribution (dark grey), but becomes a Weibull distribution. This happens around the transition wave height H_{tr}. From (Holthuijsen, 2009, pp.73-74).

Another note on the behaviour of the velocity profile is on the upper value of P. (Longuet-Higgins, 1970b) found that for values of $P \geq 0.4$ the velocity profile becomes infinite in cross shore direction. Therefore the mixing parameter cannot have a value of 0.4 or larger. This means that the physical restraints on the dimensionless mixing parameter P can be defined as:

$$0 < P < 0.4$$

Even though horizontal mixing is an important factor in the distribution of the flow velocity over the width of the surf zone it is less important than the bed shear. (Longuet-Higgins, 1970b) noted that through the dependence of the mixing parameter P on the drag and the dependency of the flow velocity on both drag and mixing, the velocity is mainly dependent on drag it experiences from the bed.

(Longuet-Higgins, 1970b) tested the formulas with laboratory experiments, which gave an overall good fit for values below P=0.4, which was expected from theory. The waves in this experiment however were very small, ranging from breaker heights of 0.05 foot (1.5 cm) to 0.191 foot (5.8 cm).

Example
Using eq. 2.8 *and for the breaker depth* $h_b = \gamma H_b$*, with* γ *a breaker parameter of* $\approx$ *0.7, a wave height at the breaker line of* H_b*=2m, a slope s=1/100 m/m, C=0.01 and an angle of incidence at the breaker line of* θ*=15 degrees yields* v_0*=0.59 m/s. With the relations given by Longuet-Higgins (1970b) and using P=0.10 this results a maximum flow velocity of* $v_{max} = V_{max} \cdot v_0$*=0.33 m/s, a mean flow velocity of* $v_{mean} = V_{mean} \cdot v_0$*=0.22 m/s and a flow velocity at the breaker line of* $v_b = V_b \cdot v_0$ *= 0.18 m/s. These outcomes seem plausible, the dimensionless viscosity parameter must of course be calibrated per case.*

Another wave induced forcing mechanism for longshore currents is the inhomogeneity of radiation stress in alongshore direction. Spatial differences in wave forcing lead to differences in wave setup as the distribution

of Momentum in alongshore direction varies. Longuet-Higgins and Stewart (1964) described this physical process using the following formula:

$$\frac{\partial S_{xx}}{\partial x} + \rho g \left(\zeta + h\right) \frac{\partial \zeta}{\partial x} = 0 \tag{2.14}$$

Equation 2.14 shows that the change in radiation stress in alongshore direction drives the alongshore water level gradient. Gradients in the alongshore Momentum distribution can for example be caused by sand bars or at the lee side of groynes. These pressure gradients give rise to flows in the direction of the lower pressure, which is from the higher to the lower water level. Currents caused by alongshore differences in wave induced Momentum are more localized currents such as the above described shadow rips or morphologically induced rips.

2.3.2 Tidal Influence

The main features of the tide are, as discussed in section 2.1, the tidal amplitude and the tidal velocities. During a tidal cycle the water level will rise and fall. This change in water level changes the location of the surf zone and possible its width and depth profile as well. This means that the behaviour of a rip current may differ between high and low water, and especially between neap and spring tidal cycles depending on the bathymetry. Furthermore, the effect of location of breakwaters or groynes on the longshore current may also change. For example, if the breakwater is short with respect to the surf zone the incoming current may deflect offshore or in a circular pattern during high water, and during low water the current may bypass the groyne.

As for the tidal flow velocity, Scott et al. (2015) found that a slow but persistent tidal flow is able to adjust the longshore wave driven current. Magnitudes of this flow differ between ebb and flow due to relatively shallow water depth with respect to the tidal wave length. With the depth of the near North Sea coast being approximately 20 m and the length of the tidal wave of approximately $L = cT_{tide} = \sqrt{gh}T = 1.25{\cdot}10^6$ m the shallow water criterion $\frac{d}{L} < \frac{1}{20}$ is easily met. As the water depth changes with ebb and tide the flow velocities must therefore also change as $h = d + \zeta$. Estimating the ebb and flood tidal wave celerities with a depth $d = 20$ m, ζ_{low}=-1 m and ζ_{high}=+1 m gives $c_{low} = 13.7$ m/s and $c_high = 14.4$ m/s. This means that the trailing edge of the wave must lag behind. This is also clear from the tidal range as shown in fig. 2.7. The water rises faster than it falls, meaning that the flood flow velocity is faster than the ebb flow velocity.

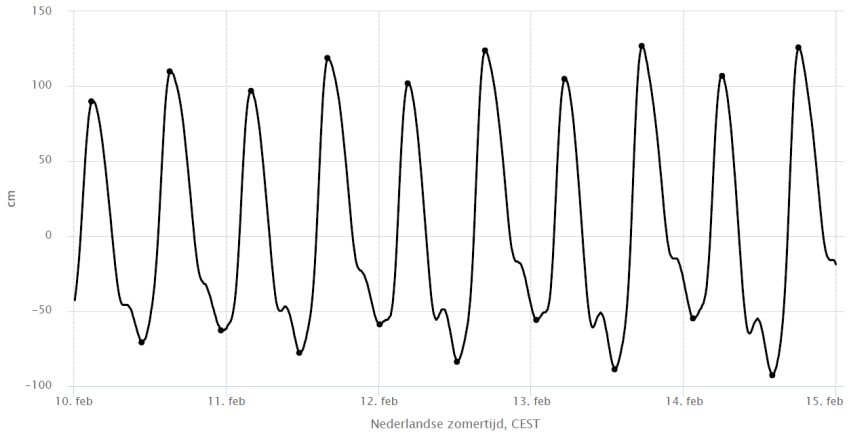

Figure 2.7: Tidal Signal at Scheveningen from 10 February 2021 to 15 February 2021. From https://waterinfo.rws.nl/

Additionally, an important effect caused by the tidal current is the formation of turbulent eddies near large protrusions such as harbours, groynes and mega nourishments (Radermacher et al., 2017). These eddies are created by acceleration due to streamline contraction and may be amplified by a simultaneously occurring water level gradient (Black & Gay, 1987).

The shape of turbulent eddies and their stability for large structures can best be described by the Keulegan-Carpenter number K_C and the dimensionless aspect ratio α as proposed by Radermacher et al. (2017) and Signell and Geyer (1991):

$$K_C = \frac{U_P T}{L_a} \qquad \alpha = \frac{L_c}{L_a} \tag{2.15}$$

In the equation for K_C U_p is the peak of the tidal flow velocity offshore, T the tidal period and L_a the alongshore length scale of the disturbance. In the equation for the aspect ratio L_C is the disturbance length in cross shore direction. Large values of the Keulegan-Carpenter number indicate that the eddy is small with respect to the tidal excursion whereas small values imply a large eddy with respect to the tidal excursion.

modeling efforts for a mega nourishment by Radermacher et al. (2017) have shown that five cases of eddy formation can be distinguished depending on the values of α and K_C as shown in fig. 2.8.

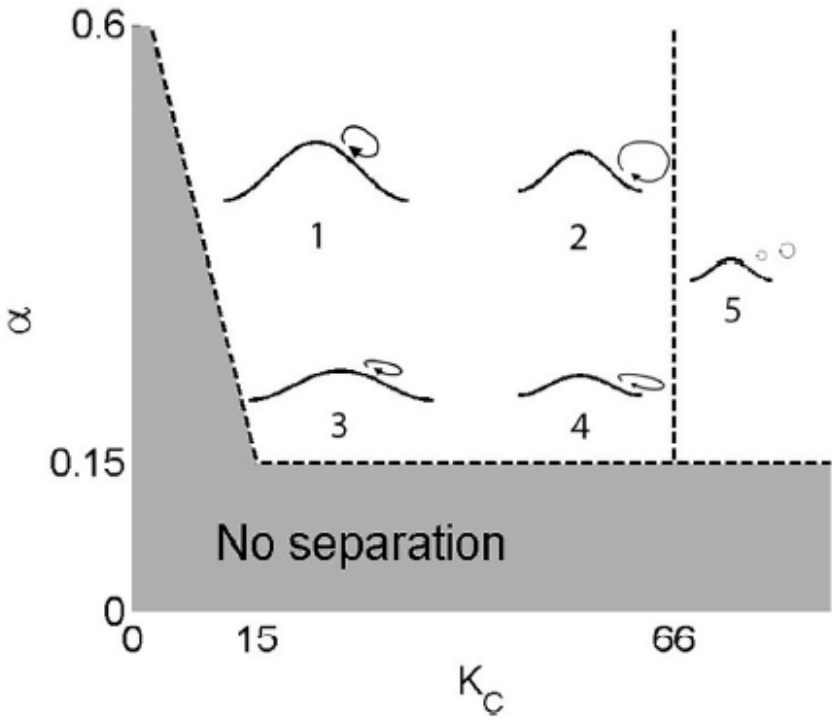

Figure 2.8: Influence of the Keulegan-Carpenter number and the dimensionless aspect ratio on the shape of turbulent eddies. From Radermacher et al. (2017).

The eddies shown in fig. 2.8 for the smaller values of K_C show a relatively small eddy in comparison with the perturbation whereas for larger values of K_C but below K_C=66 show a large eddy with respect to the protrusion. Values above K_C=66 are subject to shedding of eddies. Furthermore there will be no formation of eddies for values of α smaller than 0.15.
To assess the importance of advection with respect to bottom friction the shallow water Reynolds number Re_z can be used. This parameter was defined by Tomczak (1988) to determine the relative importance of bottom friction for wakes in shallow water near islands.

$$Re_z = \frac{UH^2}{K_z W} \tag{2.16}$$

In which U the flow velocity, H the water depth, K_z the kinematic eddy viscosity and W the width of an island. The applicability of the shallow water Reynolds number is not limited to islands and was also applied

to classify the roughness of the Dutch coast at the Sand motor mega nourishment (Radermacher et al., 2017) and headlands (Signell & Geyer, 1991). In these cases the width W must be replaced with the disturbance length L_c.

As the Scheveningen harbour is in close vicinity (i.e. 6.5 km north of the nourishment) the shallow water Reynolds number and therefore the relative contribution of the friction are expected to be close to the value of the Sand Motor, which is $\mathcal{O}(1)$. The differences in the sediment grain size and tidal behaviour such as the flow velocities and water level elevation are expected to be similar enough to compare the two cases.
Regarding the shape of the harbour moles it is best compared to a slender headland. With a length of 530 m and a width of 360 m this results in L_c=530 m, L_a=360/2=180 m and an aspect ratio of $\alpha \approx 3$. This value is high in comparison with the graph in fig. 2.8, meaning that on the basis of the aspect ratio flow separation will occur. As said above the type of separation is dependent on the Keulegan-Carpenter number. With a tidal period of 24hr and 50min and a peak tidal velocity of $\mathcal{O}(0.5)$ m/s this results in $K_C \approx 300$. This is a much higher value than the threshold for vortex shedding found by Radermacher et al. (2017). It is therefore expected that tidal flow separation will occur with a vortex that sheds over time from the moles.

An important note on the Keulegan-Carpenter number is that it is mainly used for the assessment of oscillatory flow. Tidal flows are not purely oscillatory motions due to interaction with the bathymetry. As said above the magnitudes of ebb and flood flows differ, with the latter being faster. This means that strictly speaking the Keulegan-Carpenter number as calculated above is only applicable to the flood flow as ebb flow has lower flow velocities. A lower bound for vortex shedding is found by rewriting eq. 2.15 to solve the peak flow velocity:

$$U_p = \frac{K_C L_a}{T}$$

Inserting KC=66 results in a minimum peak flow velocity of 0.13 m/s. As tidal flow velocities around the Dutch coast are typically higher this means that there must be vortex shedding during ebb flow.

2.3.3 Wind

Currents in the nearshore also can have wind as a driving mechanism. When the wind blows over the water surface it drives a current. Depending on the direction of the wind different types of flow patterns can occur. These are onshore-offshore flow and alongshore flow. As found in experiments by Murray (1974) an onshore-offshore pattern occurs when the wind is directed onshore within a range of ten degrees to shore normal. Outside of this range the wind drives a flow along the coast.
Under moderate conditions the strength of the alongshore current generated by the wind is dependent on both the wind speed and its angle with the coast, with the wind angle being the dominant factor. For wind directions in the range of 10 degrees from shore normal to parallel to the coast the wind speed and angle have a minimal effect on the movement of the flow. In this range the flow pattern is predominantly along the coast with only minor deviations (Murray, 1974). From fig. 2.9 this relation can clearly be seen for the upper 2m of a water column of 6 to 12m. Murray (1974) obtained the contour plots by using constant eddy viscosity theory and included results from Murray (1974), Saylor (1966) and Wiseman et al. (1973).
Though the result in fig. 2.9 depicts situation at the beginning of the surf zone it is also indicative of wind influence inside the surf zone. Just outside the surf zone bottom friction does not play a major role in damping the fluid motion as mainly the top of the water column is influenced by the wind. Inside the surf zone however the influence of the wind will be over a larger part of the water column, increasing the velocities near the bed and thereby increasing the bottom friction, which is proportional to the velocity squared. Therefore, it is likely that the higher flow velocities are found at the edge of the surf zone.

When quantifying the alongshore current velocities the current is also forced by the radiation stress from incoming waves (Snedden & Nummedal, 1990). A modeling attempt was performed by Whitford and Thornton (1993) to find the importance of wind forcing with respect to wave forcing for varying beach slopes and wind speeds. Under the assumption that wind-wave were generated locally found that the wind force was not only a function of the wind speed and the direction of the wind relative to the coastline, but also of

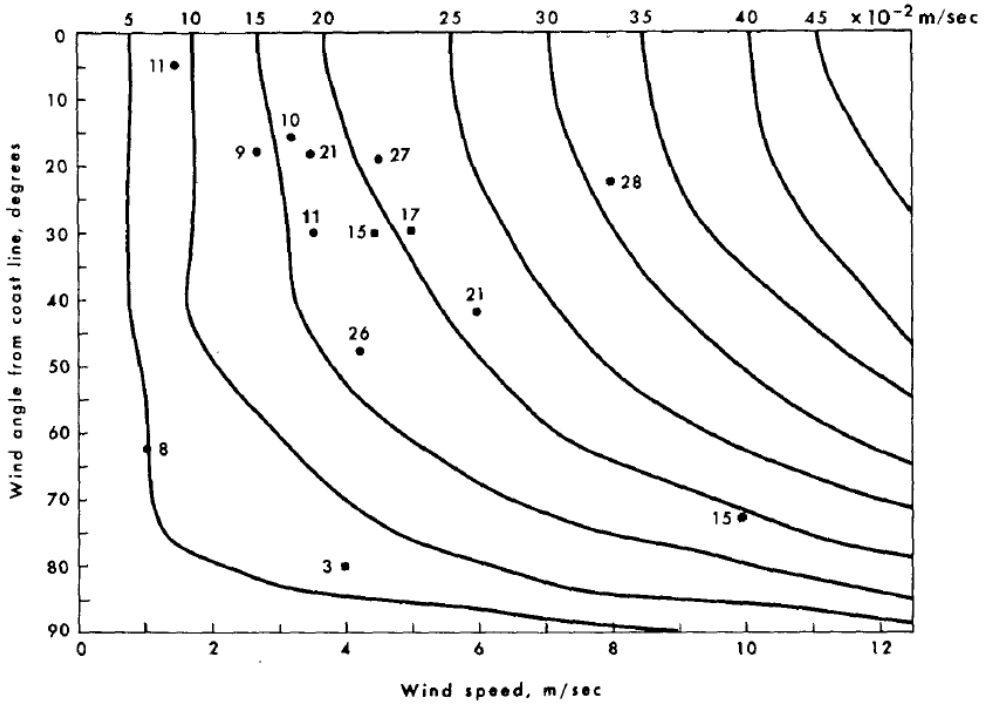

Figure 2.9: Contours of flow velocities in the upper 2m of a 6 to 12m deep water column. From Murray (1974).

the beach slope. They also found that as the beach became steeper the wind forcing became less, and vice versa for mildly sloping beaches. For beaches with a steep slope ($tan(\beta) = 0.10$) the wind forcing was less than ten percent of the wave forcing, whereas for mildly sloping beaches this was found to be between ten and hundred percent for wind speeds between 10 and 30 m/s (Whitford & Thornton, 1993). Although the results are not in longshore current velocities they are highly indicative on the importance of wind-forcing in longshore currents.

Another indication on the importance of wind on longshore currents was found by Nummedal and Finley (1978). They compared the influence of wave characteristics (breaker height, period and breaker) with the wind velocities on the total longshore current velocity. In a statistical data analysis on longshore current velocities at Debidue Island beach in South Carolina they found that the longshore wind component caused most of the velocity fluctuations (Nummedal & Finley, 1978).
The beach at which the measurements were performed has a mild slope. The combination of the mild beach slope with the high dependency of the longshore current on the longshore wind component seems to agree with the findings of Whitford and Thornton (1993) as well as with Murray (1974).
Comparing Whitford and Thornton (1993) and Murray (1974) reveals a more implicit relation. As Murray (1974) found that the flow velocities become more cross-shore directed in deeper water the total velocity vector becomes also more cross-shore directed. This may be related to the steepness of the surf zone as there simply being a smaller portion of the flow in longshore direction in steep cases.

A quantification of the wind shear stress is given by (Bosboom & Stive, 2015, p.221). In alongshore direction the wind shear is balanced by bed friction as shown in eq. 2.19. As said above only for very small angles from shore normal there is a water level setup due to wind with a negligible longshore current. In this case there is however a flow circulation over the depth in cross shore direction. Flow velocities in such cases are $\mathcal{O}(0.01)$ m/s, which is too low for the scope of this research. The equations for the wind shear and the bed

shear stress are as follows:

$$\tau_{wind} = C_d \rho_a W^2 \quad and \quad \tau_b = \rho c_f |u| u \tag{2.17}$$

The assumption in eq. 2.17 is that the wind driven current is well developed, which is after approximately a day (Bosboom & Stive, 2015, p. 221). In this formula C_d is a dimensionless friction coefficient, W the wind speed and c_f also a dimensionless friction coefficient which depends on both the bed material and bed form (i.e. for example sand dunes or ripples). The relation between the dimensionless friction factor c_f to the Chézy and Manning friction factors is through the following formulae:

$$c_f = \frac{g}{C^2} \qquad c_f = \frac{n^2 g}{\sqrt[3]{R}} \tag{2.18}$$

In which C the Chézy coefficient, n the manning coefficient and R the hydraulic radius. The full equation of motion for wind induced flow is as follows:

$$\tau_{wind} + \tau_b = 0 \tag{2.19}$$

Despite the fact that the currents are of low velocities wind induced set-up is of importance as it causes a water level rise which determines the position of the surf zone and the location of wave breaking. Wind induced set-up is governed by the following equation (Bosboom & Stive, 2015, p. 220)

$$\rho g h \frac{\partial \zeta}{\partial x} = \tau_{wind,x} \tag{2.20}$$

Equation 2.20 implies that the water level gradient $\frac{\partial \zeta}{\partial x}$ is inversely proportional to the water level h. This means that in shallow water the set-up is larger than in deeper areas. As Scheveningen is located at the North Sea coast, which is a (shallow) shelf sea, wind induced set-up plays an important role (Emeis et al. (2015); Bosboom and Stive (2015, p. 223)). Consequently it is important for the profile of the surf zone as it may move shoreward during high energy wind conditions. This is important to take into account because the location of the surf zone determines governs the shoaling and breaking behavior of the incoming waves.

With the findings from literature it seems apparent that the longshore component of the wind has a significant impact on longshore current velocities. To the author's knowledge it is has thus far not been implicated as a direct influence on boundary rips.

2.3.4 Structure Characteristics

Behavior of boundary rips is strongly dependent on the characteristics of structures in the surf zone. Scott et al. (2015) found that the ratio of the groyne length L_g over the surf zone width X_b is a good indicator of the hydrodynamic response to incoming waves near groynes. Field observations showed that the strongest flow velocities would occur at the tip of the groyne. It was also found that the intensity of the rip flow velocity is mainly dependent on the significant wave height H_s and the wave angle of incidence θ. Interestingly enough there seemed to be a threshold of $H_s \approx$0.4 m and $\theta \approx 10$ degrees for which the rip flow velocity would remain below 0.3 m/s. This value was set to be the limit for swimmers to safely escape a rip.
For the ratio of the groyne length over the surf zone width Scott et al. found that for values of $L_g/X_b <$ 0.5 rip currents had flow velocities similar to the longshore flow velocity and almost no deflection. For 0.5 $< L_g/X_b <$ 1.25 there was an increase in both the deflection and rip flow velocity. Rip flow velocities were also maximized in this configuration. Lastly, for $L_g/X_b >$ 1.25 full deflection takes place.
Another important feature found in the study by Scott et al. is the groyne spacing L_s/L_g, which is the distance between groynes divided by the groyne length. Maximum rip velocities were found for $L_s/L_g >$ 4. This seems to be due to the fact that the longshore velocity due to obliquely incident waves has to build up. It was found that the maximum longshore velocity is found for values of $L_s/L_g \approx$ 4-6. Although in this study there is no groyne field present, it is of importance to estimate at which point on the shoreline the maximum longshore velocity is reached, and if there are features nearby that could play a role in the longshore flow.

Lastly it was noted that the bathymetry may be of importance on the breaking behavior of waves, even though a simplified bathymetry in the numerical model seemed to agree very well with field measurements.

Pattiaratchi et al. (2009) found that for increasing wave height there was also an increase in the offshore rip extent. Furthermore it was found that an increased wave height would lead to increased rip velocities. At the groyne tip the flow pattern deflects due to the obliquely incident waves. These findings seem to agree with those from Scott et al..

As for the situations in which either a shadow rip or a deflection rip occurs, Sous, Castelle, Mouragues, and Bonneton (2020) found that at headlands shadow rips mainly occurred when incoming waves were close to shore normal. Deflection rips were prevalent when the angle of incidence becomes larger. Oftentimes the shadowing effects were eclipsed by the flow velocities from the deflection rip. This means that the configurations may coexist, but that in such cases shadowing effects are almost negligible. They also found that between the shadow rips and deflection rips the latter had the highest exit rates and that the shadow configuration mainly led to a circulating flow pattern.
The difference between this study and the ones performed by Pattiaratchi et al. (2009) and Scott et al. (2015) is the size of the perturbation. This likely to be a result of a fully developed longshore current.

2.4 Basic Rip Current Model

2.4.1 Lagrangian and Eulerian Reference Frames

Flow fields can be described using two different frameworks: the Eulerian framework and the Lagrangian framework. The Eulerian reference frame describes the fluid motion from a fixed standpoint whereas the Lagrangian describes fluid motion by moving along with a particle. As the focus of this research is on following surfers and swimmers in a rip current, the Lagrangian approach is most suitable.

2.4.2 Transport Patterns

As hinted in the descriptions of Deflection and Shadow rips above transport patterns are essential in describing rip behavior. The difference between current patterns and transport patterns is that current patterns are a snapshot in time of the flow field, whereas a transport pattern is the description of the movement of a particle in time in this flow field. As the currents in a flow field may change direction and intensity in time it will influence the pattern of a particle inside the flow field.
The trajectory of a particle in the horizontal plane can mathematically be described as the integral of the particle position and velocity over time:

$$\begin{aligned} x_{end} &= x_0 + \int_{t=0}^{t=t_{end}} u\,(x,y,t)\,dt \\ y_{end} &= y_0 + \int_{t=0}^{t=t_{end}} v\,(x,y,t)\,dt \end{aligned} \tag{2.21}$$

In which u the velocity in x-direction and v the velocity in y-direction.

2.5 Prior Delft3D Modeling of Rip and Nearshore Currents

Before this study several modeling efforts in Delft3D on rip currents have been performed. The rip mechanism in these studies differed slightly, such as by Schlooz (2012) and Van der Baan (2013). The study mentioned in section 2.3.4, by Scott et al. (2015), on rip currents in a groyne field was performed in XBeach. Lastly, Pattiaratchi et al. (2009) used experiments with Eulerian measurements and drifters in the lee of a groyne and hindcasted the result using the computational program MIKE 21.
Schlooz (2012) looked at the formation of mega rips at the Sand Motor mega nourishment located on the

South Holland coast. A hindcast of field tests with drifter measurements led to the conclusion that the model was in adequate agreement with observations. The velocity, location, shape and size were consistent with the measurements, though the model seemed to underestimate velocities outside of the rip. Also the computed tidal range differed from observations.
Schlooz also mentioned that the model used a constant wave field which does not allow for wave grouping, which ultimately led to the underestimation of maximum offshore velocities. For the simulation of boundary controlled rip wave grouping has thus far not found to be of importance in relevant literature, but is still a relevant issue to take into account.

Research by Van der Baan focused on the flow pattern of a system with submerged transverse breakwaters on wave forcing and the subsequent shoreline response. The Delft3D model was validated and compared with analytical and empirical relations. It was found that the model gave accurate results for the wave set-up which showed a difference of approximately 1 percent. Differences between the analytical approach and model outcome became higher with increased difference in radiation stresses at the submerged breakwaters and the shore line without breakwaters to about 10 percent.
Although the focus of the research is not on current velocities it provides a glimpse on the capabilities of Delft3D in computing rip currents. Erosion and accretion are processes that can be heavily influenced by rip behaviour. The shoreline response to rips may therefore be seen as an indicator of rip behaviour in this model. As stated by Van der Baan the model was not yet capable of making a quantitative prediction on shoreline evolution, but could certainly be used to make a preliminary assessment on the response of the system.

Scott et al. (2015) modeled boundary rip currents in a groyne field with varying significant wave height H_s, wave angle of incidence θ and varying breakwater length with a simplified morphology using XBeach. Tide and Wind waves were applied at the boundaries. Wind forcing was employed in the direction of the waves. They were able to reproduce their field measurements, which allowed them to investigate further on the response of the system on the aforementioned parameters with confidence. The main difference with this research is the computational program used for calculating the hydrodynamics. Both XBeach and Delft3D are very similar in their computational abilities.

Measurements performed by Pattiaratchi et al. (2009) showed that an increase in wave height would in turn increase the rip velocity. This was also reflected in the numerical model. There is however a difference in the eddy generated by the model and the eddy obtained from field measurements. The model outcomes showed retention of the eddy in wake of the groyne, whereas field data showed a larger eddy. As mentioned in section 2.3.2 tidal currents are able to generate shedding vortices. But since the spring tidal range at the measurement location is only 0.8 m it may be very well possible that the tide does not induce vortex shedding. This makes it plausible that the vortex extends beyond the groyne but does not necessarily move away.

Comparing the outcomes from Scott et al. with the modeling efforts by Schlooz and Van der Baan, allows for confidence in the modeling efforts of boundary rips in Delft3D. The aforementioned modeling efforts in Delft3D show that the primary inputs (waves, tide and wind) are well behaved in Delft3D. Even though Scott et al. used XBeach and Pattiaratchi et al. used MIKE 21, due to the similarities between the programs it seems reasonable to believe that modeling of the Scheveningen harbour area in Delft3D and accurately predicting rip current behaviour is certainly achievable (Reniers et al., 2009).

2.6 Swimmer Safety

The maximum velocity an average person can handle is about 0.3 m/s (Scott et al., 2015). This is different per age, sex and physical condition. An indication of the swimming abilities for humans has been given in table 2.2.
From table 2.2 it is instantly clear that most people will be in trouble as boundary rips are often associated with velocities larger than 0.5 m/s. In addition people will in most of the cases have to deal with incoming

Table 2.2: Swimmer velocities in a pool per age, sex and physical condition. From Schlooz (2012)

Physical ability rating	*Gender*	*Age category* 13-19	20-29	30-39	40-49	50-59
Very poor	M	<0.70	< 0.60	< 0.49	< 0.40	< 0.35
	F	< 0.60	< 0.40	< 0.35	< 0.28	< 0.21
Poor	M	0.70 - 0.80	0.56 - 0.69	0.49 - 0.62	0.42 - 0.55	0.35 - 0.48
	F	0.56 - 0.69	0.42 - 0.55	0.35 - 0.48	0.28 - 0.42	0.21 - 0.35
Average	M	0.83 - 0.97	0.70 - 0.80	0.62 - 0.76	0.56 - 0.69	0.49 - 0.62
	F	0.70 - 0.80	0.56 - 0.69	0.49 - 0.62	0.42 - 0.55	0.35 - 0.48
High	M	0.97 - 1.11	0.83 - 0.97	0.76 - 0.90	0.70 - 0.83	0.62 - 0.76
	F	0.83 - 0.97	0.70 - 0.83	0.62 - 0.76	0.56 - 0.69	0.49 - 0.62
Excellent	M	> 1.11	> 0.97	> 0.90	> 0.83	> 0.76
	F	> 0.97	> 0.83	> 0.76	> 0.70	> 0.63

waves and panicking, which is very different from the conditions in the table. It is therefore very reasonable to assume 0.3 m/s as a threshold value for rip currents.

2.7 Knowledge Gap and Conclusion

The found knowledge gap is focused around the limited amount of research that has been performed on boundary rips and the prediction thereof. This research will therefore focus on trying to build a model which can find conditions which lead to boundary rips, specifically for the Scheveningen harbour area.

Answer to sub question I: known factors in boundary rip formation are primarily the tide and waves. Wind may be of importance in amplifying the current velocity and the bathymetry is of importance in the behavior of wave breaking. Additionally the ratio L_g/X_b is important for the generation of a rip current.

Answer to sub question II: The known conceptual models are by wave shadowing and by the deflection of the longshore current. These two types are however not necessarily independent of each other and may coincide as found by Scott et al. (2015) and Sous et al. (2020).

3. Description and Analysis of the Delft3D Numerical Model

This chapter provides a description of the harbour area model in Delft3D. In the first section the grid obtained from JARKUS measurements will be discussed. Thereafter follows a description of the Delft3D FLOW module. This chapter concludes with the Delft3D WAVE module.

3.1 Bathymetric Grid

Delft3D uses a bathymetric grid to compute the hydrodynamics of the system, such as the water level and flow velocities. A bathymetric grid consists of cells in which the depth at every location is defined. The bathymetric grid for the Scheveningen harbour area is obtained from the JARKUS program. This program consists of yearly measurements performed by the Dutch Ministry of Infrastructure and Water Management with the goal of mapping the current bathymetry and to keep track of long term changes in the coastal system. Measurements are taken in intervals of 250m in alongshore direction and intervals of 200m in cross-shore direction up to a depth of 20m below Nieuw Amsterdams Peil (NAP). The result is a bathymetric grid with cells of 250m by 200m.
For the use of a bathymetric grid the spacing of the JARKUS measurements is too coarse: the harbour moles would fit in just six grid cells whereas the aim is to find detailed hydrodynamic behaviour in this area. Therefore the depths from the JARKUS measurements are linearly interpolated in the cross-shore and longshore directions in intervals of 20m and 25m respectively. The result is a much finer bathymetric grid which allows for computations on the required scale.
The grid is rotated 50 degrees to account for the orientation of the coast at the Scheveningen area.

For the FLOW and WAVE modules Delft3D uses two grids. The FLOW module grid is the exact area that is modeled with the interpolated JARKUS grid cells and depths. Normally the WAVE module uses an extension of the FLOW grid on the lateral and offshore boundaries such that the incoming waves can move freely into the domain. At the Wave boundaries wave forcing is induced in a uniform manner. This means that at the offshore boundary and the lateral boundaries the incoming wave heights are the same. Consequently, some waves may be too high with respect to depth at the lateral ends, especially close to the shore line. This leads to points of instant wave breaking at the edge of the domain and introduces errors at the model boundaries. Therefore the lateral boundaries are extrapolated further for the WAVE grid such that wave breaking takes place outside the model boundaries, but is still resolved within the WAVE module. This reduces wave induced perturbations at the boundaries and the distance these perturbations may travel into the model domain.

3.2 FLOW Module

In this research the Delft3D FLOW module is used to resolve the system's hydrodynamic response to forcing by tide, waves wind. It is also able to calculate flows for other forcings, such as by stratified flows, and apply this to morphodynamic calculations. This is however outside the scope of this research.

The FLOW Module has four boundaries: one boundary and the landward side, including the harbour area,

two lateral boundaries and one offshore boundary. Of these boundaries the landward boundary has no boundary conditions. It is however impermeable due to the bathymetry being impermeable. The offshore boundary is defined as a water level boundary. This type of boundary is a so called open boundary and allows flows pass through. Water level boundaries can either be fixed, a time-series, harmonic or astronomic. For wind and wave forcing this is a fixed water level, whereas if the run includes tide the water level boundary is astronomic. Delft3D computes the astronomic water level boundaries as follows (Deltares, 2020):

$$\zeta(x,t) = \sum_{i=1}^{N} \hat{\zeta}_i \cos(\omega_i t - k_i x) = \sum_{i=1}^{N} \hat{\zeta}_i \cos(\omega_i t - \varphi_i) \tag{3.1}$$

In which N the amount of tidal components, and per tidal component i there are a water level amplitude $\hat{\zeta}_i$, angular frequency ω_i, wave number k_i and tidal phase φ_i.
The lateral boundaries are also open boundaries, but have a water level gradient $\frac{\partial \zeta}{\partial x}$ imposed: the slope of the water level at the boundaries is the same as in the adjacent grid cells. Boundaries with a water level gradient are also called Neumann boundaries. Here again the difference has to be made between scenarios including and excluding tidal forcing. Without tidal forcing the water level gradient is assumed to be zero. Delft3D resolves the water level gradient for runs including flow using eq. 3.2 (Deltares, 2020):

$$\frac{\partial \zeta}{\partial x}(x,t) = \sum_{i=1}^{N} k_i \hat{\zeta}_i \sin(\omega_i t - k_i x) = \sum_{i=1}^{N} k_i \hat{\zeta}_i \cos\left(\omega_i t - \left(\varphi_i + \frac{\pi}{2}\right)\right) \tag{3.2}$$

It would also be possible to apply water levels at both the offshore and lateral boundaries, but Roelvink and Walstra (2005) have shown that this configuration induces larger disturbances at the lateral sides. They argued that it is difficult to predict what the water level and flow velocities at the boundaries. Therefore it would be easier to let the model determine these parameters by using a Neumann boundary.
Comparing eq. 3.1 and eq. 3.2 shows a phase difference between the water level and its gradient resulting from derivating the cosine. From the periodicity of the sine and cosine functions it is known that $sin(\varphi) = cos\left(\phi \pm \frac{\pi}{2}\right)$. The sign in the cosine depends on the direction of the wave: if the wave progresses in positive x-direction (i.e. to the North) it will be $\phi + \frac{\pi}{2}$. Movement in the negative direction (i.e. to the South) results in $\varphi - \frac{\pi}{2}$. As discussed in section 2.1 the tidal wave moves from South to North along the Dutch coast, and therefore the phase difference must be $\varphi + \frac{\pi}{2}$

Delft3D requires only the water level amplitude, water level phase, Neumann amplitude and Neumann phase as inputs. As for setting the Neumann boundary parameters: the amplitude of the boundary is simply the wave number k multiplied with the tidal wave amplitude $\hat{\zeta}$. The relation between phase and wave number is given by:

$$\varphi_i = k_i x \tag{3.3}$$

This means that the phase of each tidal component is different for each point on both the lateral and offshore boundaries. Each boundary is therefore discretized: the offshore boundary consists of seven parts and both lateral boundaries are divided into four parts. This is shown in section 3.2. To comply with continuity the ends of adjacent parts must have the same amplitudes and phases section 3.2. When it comes to the continuity between the offshore and lateral boundaries, the offshore ends of the lateral boundaries have a phase of $\varphi_{offshore} + \frac{\pi}{2}$. This is also shown in section 3.2

The amplitude and phase for every tidal component are obtained from Delft Dashboard, which is a program with the ability to compute these properties. It does however not readily compute the wave number of every tidal component, which must consequently be calculated by hand. There are two methods to do so: the first one is by using the wave celerity c and angular frequency ω of the tidal component, the second one is by using:

$$\Delta\varphi_i = \frac{2\pi}{L_i}\Delta x = k_i \Delta x \tag{3.4}$$

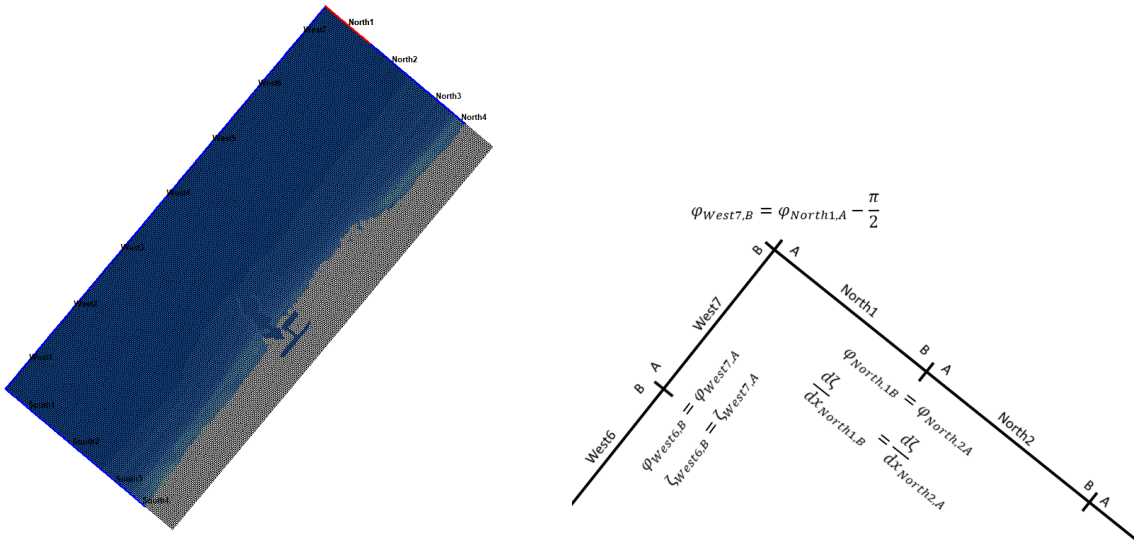

Figure 3.1: a) All model boundaries in the FLOW module. b) Boundary discretization and continuity of the tidal phase between two boundary parts and between sub-boundaries. The boundary "West" is the water level boundary and the boundary "North" is the Neumann boundary. The figure also shows the relation between the phases of the water level and Neumann boundaries and the phase continuity between adjacent boundary sections.

The latter method is proposed by both Roelvink and Walstra (2005) and Deltares (2020). Deltares (2020) states that the method using the angular frequency ω and wave celerity c, with $c = \sqrt{gh}$ is also applicable, but this method does not sufficiently take into account the deformation of the wave in shallow water. The method using eq. 3.4 is preferred because wave deformation is already implicated in the data obtained from Delft Dashboard.
Lastly, it is important to note that reflection may occur at the offshore boundary when using this method. Therefore it is important to prevent this by using the keyword `Cstbnd=#YES#`.

Wind forcing in Delft3D is taken constant over the entire domain: the wind speed and wind direction are the same for every grid cell. To reduce spin-up time and errors due to wind the wind forcing is linearly increased over a period of 5 hours from the beginning of the model.
Wave forcing is applied with the Delft3D-WAVE function, which is a direct coupling with the Delft3D WAVE module. This function performs a WAVE simulation after each time Delft3D FLOW writes information to a communication file. A requirement to use the Online function is that a WAVE input file is set up with the hydrodynamic coupling (Deltares, 2020).
Obtaining a Lagrangian flow field from Delft3D is done with the keyword `SMVelo=#glm#`. Delft3D calculates the Lagrangian flow velocities as follows:

$$u_{glm} = u_E + u_S \tag{3.5}$$

In which u_{glm} the Generalised Lagrangian Mean velocity, u_E the Eulerian flow velocity and u_S the flow velocity due to the Stokes' drift (Deltares, 2020). By adding the Stokes' drift to the Eulerian flow the orbital wave motion affecting suspended particles can be accounted for.

The model is situated at a latitude of 53 degrees. As said above the bathymetry is obtained from the JARKUS measurements. The harbour interior is however modeled with a constant depth of 5m. The model runs for five days and has time step of 0.5 min. This time step seems to yield more stable results than a one minute time step. A simulation length of 5 days seems to be the optimum between simulation length and damping of the initial model perturbations.

Depending on the model runs Wind and Wave are included as physical processes. Wave runs are, as mentioned above, combined with the Online Delft3D-WAVE functionality.
As for the physical parameters a uniform Manning roughness of 0.028 $s/m^{\frac{1}{3}}$ is applied. The wave stresses are resolved using the Fredsøe formulation. The slip condition is set to free and the Horizontal eddy viscosity is set to a value of 1 m^2/s.
The used advection scheme for Momentum is Cyclic, which is the standard Delft3D scheme. Drying and flooding check is set at the grid cell centres and faces. Lastly, the depth at the grid cell faces is set to mean, the threshold depth is set to 0.1m, marginal depth to -999m and the smoothing time is 360 minutes.

3.3 WAVE Module

Wind waves are generated in the Delft3D WAVE module. As mentioned above the WAVE module uses a larger grid than the FLOW module, with extended lateral boundaries by additional grid cells. In the extended area wave breaking and refraction are the most important processes in this part of the grid, and are both depth driven. Since the changes in bathymetry only take place in the cross shore direction the resolution of the grid in only the cross shore direction is of importance. Therefore it is possible to increase the grid cell size in alongshore direction, which in turn will result in only a limited extra amount of computational time. To allow for a gradual transition from the outer WAVE grid to the FLOW grid the longshore sides of the cells are gradually increased. An illustration can be found in fig. 3.2.

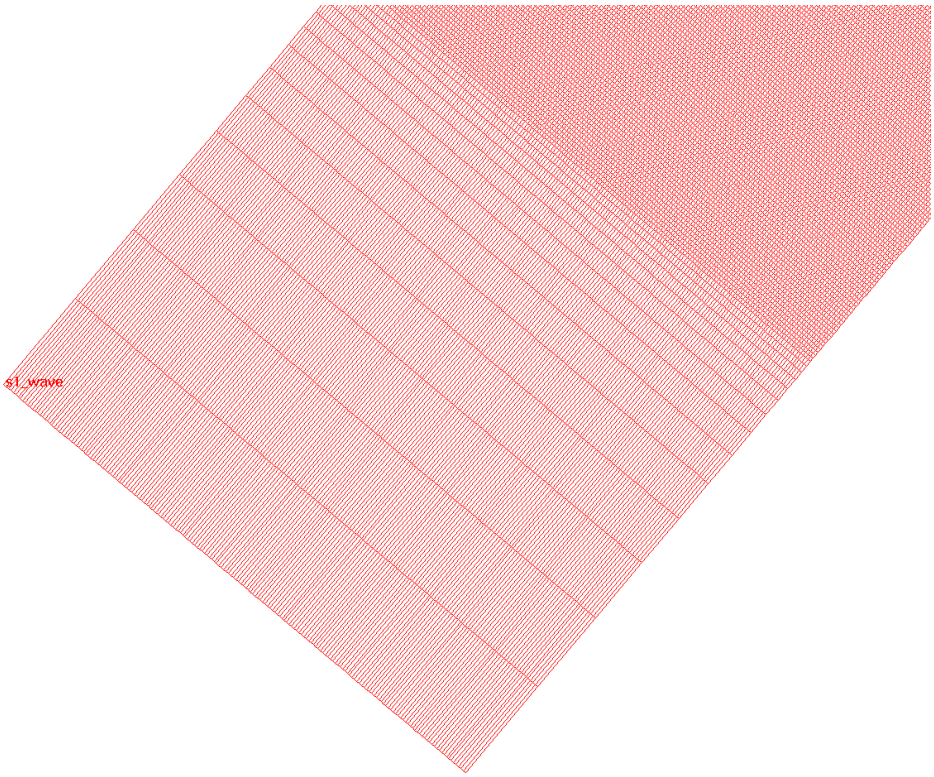

Figure 3.2: Extended area of WAVE grid

Incident waves are generated at the boundaries of the WAVE module. These boundaries are located at the three edges of the wave grid: both lateral ends and the offshore end. Unlike for the flow grid these boundaries do not have to be discretized because waves with the same significant wave height H_s and peak period T_p will occur over the size the modeled domain in real world conditions as well. The boundaries are defined by their respective orientations, which are "West" for the offshore boundary, "Northeast" for the northern lateral boundary and "Southwest" for the southern lateral boundary.

As said above the main problem lies with the offshore waves applied at the nearshore ends at the lateral boundaries. This is problem is remedied with the extended wave grid as discussed above.
Modeling is focused on wind waves, which means that the directional spreading is relatively high. The model uses the cosine power function to compute the wave spreading. This is set to 4. The periods of wind waves a peak period of 5-6 seconds is applied (de Schipper et al., 2016). To the spectral space the JONSWAP spectrum is applied with a peak enhancement factor of 3.3. The period is set to peak.
Refraction, diffraction and breaking of waves are solved by SWAN, which is a built-in program used for computing random, short-crested wind waves, and the development of these waves inside the domain.
The computational grid in the WAVE module is obtained by coupling the FLOW file to the WAVE file and is therefore the same. The Directional space is set to a circle with 36 directions. As for the frequency space the lowest frequency is 0.05 Hz and the highest frequency is 1 Hz. The whole spectrum is made up of 24 bins in total. The WAVE module uses and extends both the water level and the current obtained from the FLOW results, but not the bathymetry and wind.
The directional space and Frequency space values are both set to 0.5. In the accuracy criteria the Relative change is set to 0.02, the percentage of wet grid points to 98%, the relative change of H_s and T_{m01} to 0.02 and the maximum number of iterations is 2.
Lastly, the output for the computational grid is set to intervals of 60 minutes.

4. Theoretical Model Assessment

In this chapter the validation of the Delft3D model will be discussed. As no field data is available results are compared to expectations obtained from literature. The theoretical model assessment will be conducted by initially picking one forcing mechanism and applying it to the model with the goal of assessing the model performance. The used forcing mechanisms are: tide, waves and wind. After evaluation of these individual mechanisms combinations of forcings will be made. The goal of assessing the individual components and combinations of those is to test the model behaviour and map the boundary conditions for which the model is applicable. Model validation is performed at four cross sections, with two cross sections at each side of the harbour (fig. 4.1).

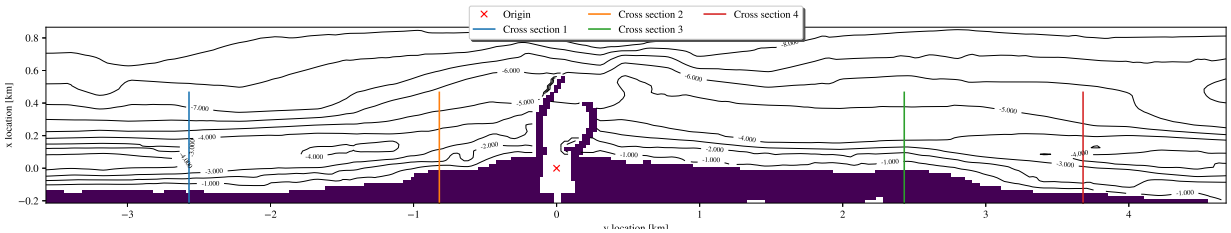

Figure 4.1: Locations of cross sections and origin

In the wind and wave validations only one side of the wave and wind directions, i.e. the southern directions are investigated. It is assumed that both boundaries act very similar for incoming and outgoing flow/waves/wind and therefore this is considered sufficient.
Figure 4.2 shows a schematization of the coastline and the used directions. From here on directions relative to shore normal will be denoted with RSN.

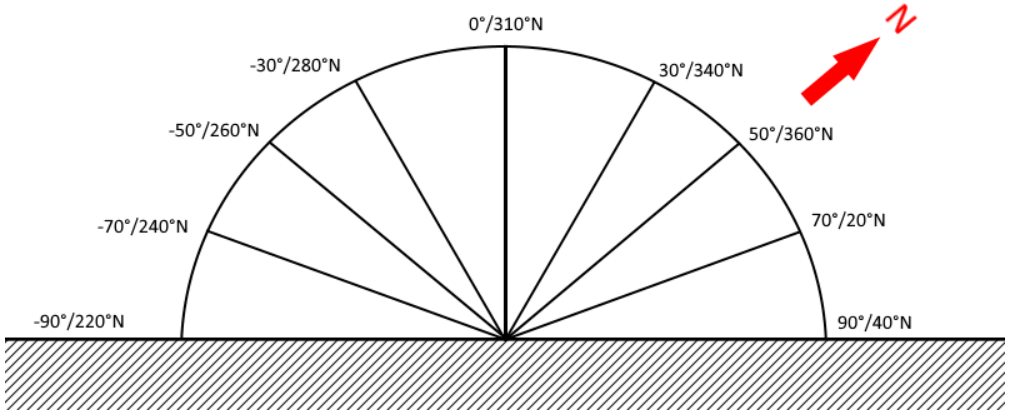

Figure 4.2: Schematized overview of incoming wind and wave directions in degrees to shore normal and degrees North respectively.

4.1 Tide

In order to determine the model behaviour on tidal forcing a first look will be taken at the performance of the tidal signal. The model is run for four days. In this chapter only the model results will be shown for a tidal phase between neap and spring tide, as the results in model behaviour are very similar. The tidal water level and flow velocities in water with a depth of approximately 10m can be found in fig. 4.3.

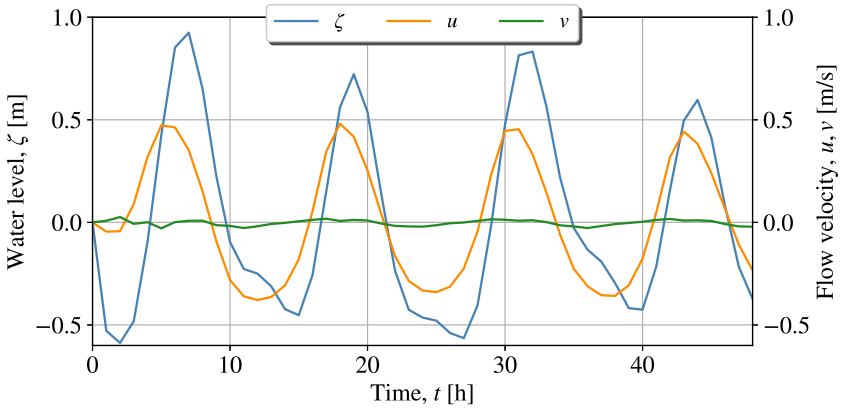

Figure 4.3: Tidal water level ζ, longshore flow velocity u and cross shore flow velocity v in approximately six tidal cycles.

A first look at fig. 4.3 reveals that the longshore flood flow velocities are higher than the ebb flow velocities. This was also described in section 2.3.2 as the result of the water level differences between the two tidal phases as the wave celerity is described by $c = \sqrt{gh}$. Furthermore the water level shows differences between two subsequent high water peaks and low water troughs. This is caused by the daily inequality.

The model boundaries behave without showing any perturbations during ebb and flood (Figure 4.4). Similarly the nearshore area located between x= -0.1 km and x= 0.7 km shows a gradual increase in flow velocity in seaward direction. This is due to the decreased effect of the bottom friction on the longshore flow as depth increases. During flood flow a vortex forms behind the harbour area as seen in fig. 4.4a. As discussed in section 2.3.2 this vortex was expected to form. Its behaviour will be discussed later in this section. Similarly during ebb flow there is also a turbulent area behind the harbour mole due to streamline expansion which will also be discussed below.

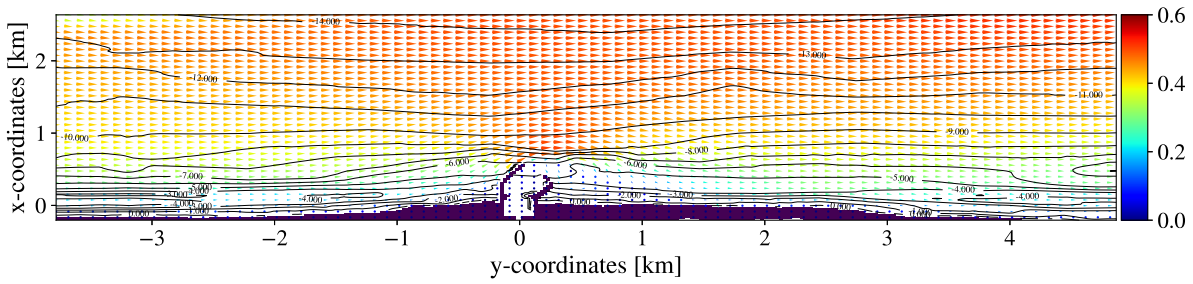

(a) Flood flow

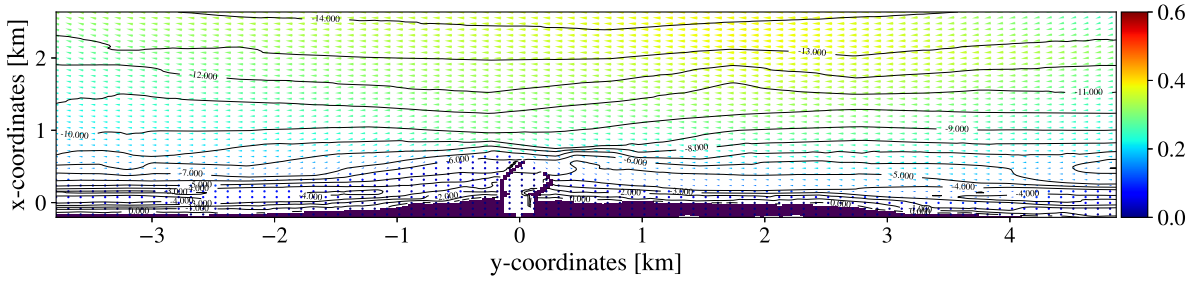

(b) Ebb flow

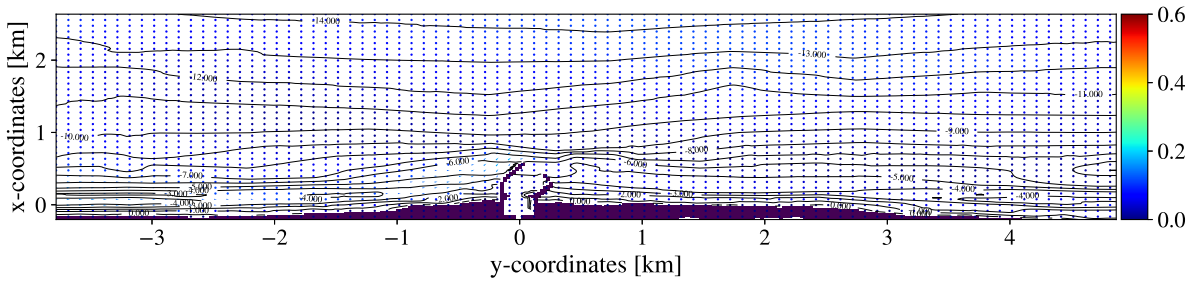

(c) Ebb to flood flow

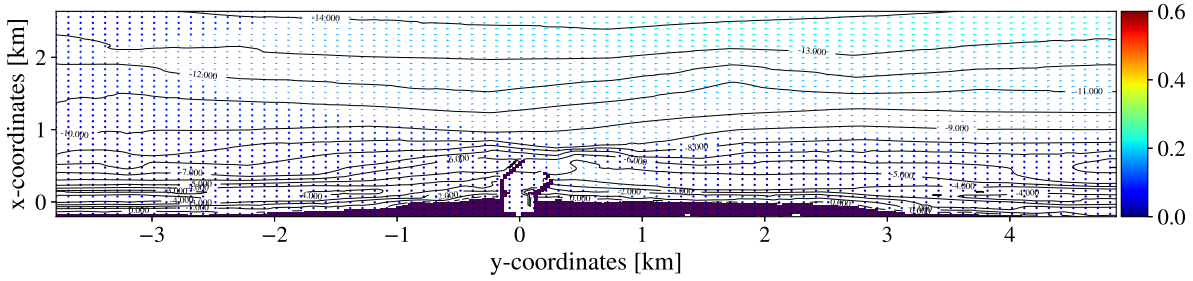

(d) Flood to ebb flow

Figure 4.4: Flow fields of the whole domain during flood flow (a), ebb flow (b), flow shifting from ebb to flood (c) and flow shifting from flood to ebb (d) at T=50, T=56, T=53 and T=58 hr respectively. The arrows show the direction of the flow field and the colors of the arrows show the velocities as related by each color bar. Shoreline and harbour moles are depicted in black.

When the tide turns from from either from ebb to flood or the other way around it can be seen that the flow in the deeper areas lags behind with respect to the shallower areas. This is because of the difference in water masses that have to be accelerated. The mass in the deeper areas is larger than in the shallow area, and by Newton's second law this means that for an equal force the acceleration in the shallow area is faster. Overall the flow fields for the tide turning cases seem to behave properly. Around the harbour moles the flow accelerates due to streamline contraction and decelerates again once past the moles. In the area between the mole tip and the shoreline, which lies approximately between x= -0.1km and x= 0.7 km, the flow is well behaved. There are no sudden instabilities in alongshore flow velocities and flow directions.

In both flow turning cases the longshore flow in the area between the harbour end and the shoreline looks stable the boundaries show a flow direction and magnitude that deviates from the rest of the flow in the flow field. When the tidal flow turns around the model produces a stable current between the shoreline and offshore end of the harbour. The currents at the offshore boundary during flood to ebb flow are directed opposite to the nearshore flow. For the case in which the tide turns from ebb to flood mainly the nearshore current is noticeable. The magnitude of the flow velocities in this case are lower than 0.2 m/s.
At the left border in during ebb to flood flow there is some flow divergence around the 1.0 km in cross shore direction with flows of 0.05 m/s (fig. 4.4c).
These deviations are however very limited in magnitude and reach as they are located far from the northern harbour mole and the area adjacent to it.

To compare the behaviour of the flow behaviour near the harbour moles five points will be checked. These are located at the harbour entrance and at both the upper and lower ends of each mole. A depiction of the locations can be found in fig. 4.5.

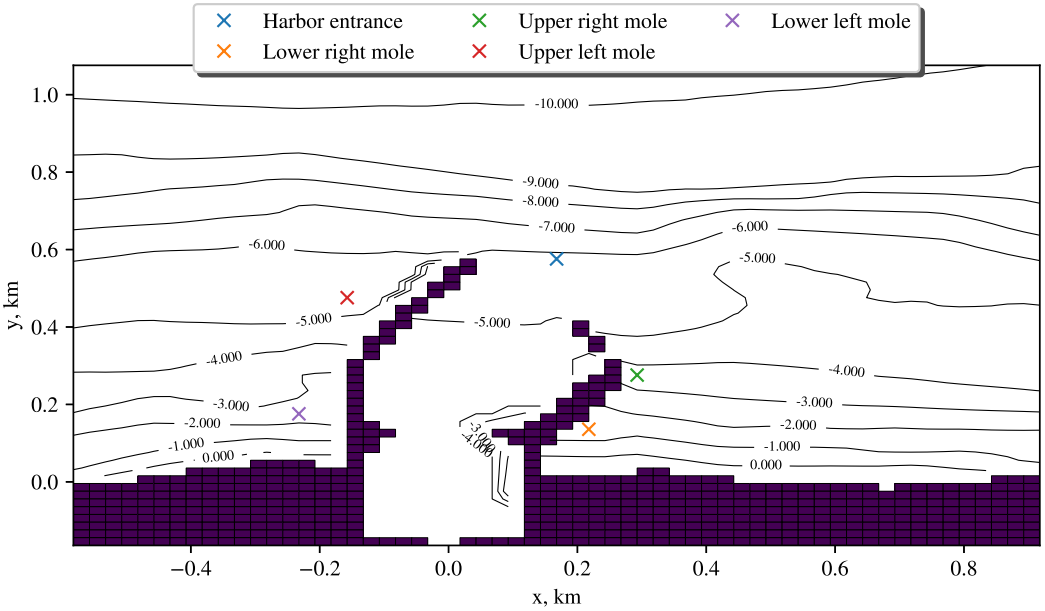

Figure 4.5: Locations of tidal measurements in model

The locations shown in fig. 4.5 are compared to the results of water level elevation and flow velocity with the deep water outcomes. First the water levels are analyzed. The nearshore water levels are very similar to the water level in deep water. This is only reasonable; though the tidal wave has phase differences over both the cross-shore and longshore directions these are very small due to the wave length, which is of $\mathcal{O}(500km)$. Looking at the flow velocities reveals some differences both the magnitudes and flow directions. The velocities at the left mole are out of phase with the flow in deep water during ebb. As said above there are vortical

structures in the wake of the harbour moles during both ebb and flood. With the flow velocity out of phase during ebb flow at the southern side of the harbour this indicates that there must be a rotating flow. Similarly, during flood flow the flow velocities at the upper right mole are out of phase with deep water. The tidal flow signal of the longshore flow at the lower right mole is very weak, which is a result of its sheltered location compared to the other measurement points. All out of phase flows have very low flow velocities, but this is expected behaviour when a turbulent structure forms due to flow line expansion.
By dividing the flow velocity at each measurement location by the deep water velocity the exact moments at which the flow is out of phase are identified (fig. 4.6). When the relative flow velocity is smaller than 0 it means that there is out of phase flow. This allows for a more quantitative analysis of the flow velocities. For example, the points which have the strongest out of phase velocities are the harbour entrance, the measurement location at the upper left mole and the location at the upper right mole (fig. 4.6d).

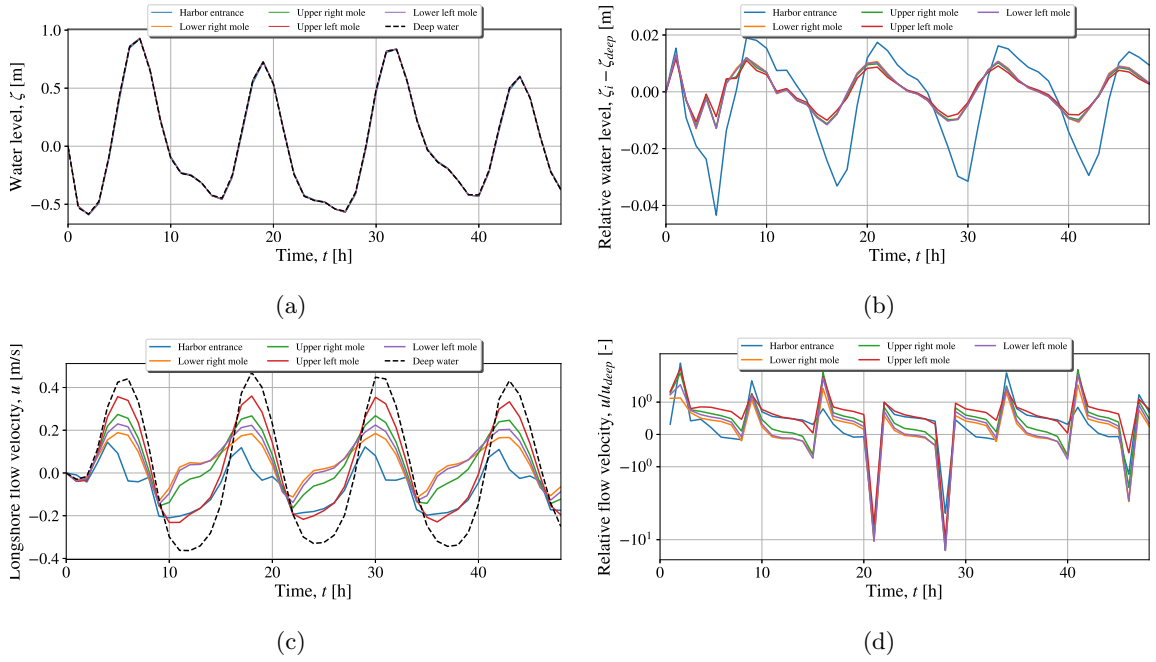

Figure 4.6: Comparison of deep water velocity and water level over time with locations near the harbour moles. a) Water levels for deep water and locations near the harbour. b) Water level of every point minus the water level in deep water. c) Longshore flow velocities for all points including deep water. d) Longshore flow velocity per location divided by the longshore flow velocity in deep water.

Lastly for the tide the behaviour of the vortex will be analysed. Signell and Geyer (1991) described that for values of K_C >66 there should vortex shedding (section 2.3.2). From the geometric properties of the harbour it was deduced that for Scheveningen harbour there would vortex shedding for $U_p \leq$0.13 m/s. Model results gave peak flow velocities of approximately 0.45 m/s and 0.39 m/s for flood and ebb flow respectively, leading to the conclusion that vortex shedding should occur in the model.
From fig. 4.7 it is clear that during both the ebb and flood phases there is vortex formation and shedding. The shedding of the vortex is accelerated by the change of the longshore flow and drives the eddy seaward, where it eventually vanishes. The ebb vortex is slightly smaller in size than the flood vortex. This may be due to the geometry of the harbour moles. Additionally, the entrance seems to facilitate the formation of the flood vortex as the vortex outgrows this area in a maximum of 2 hours. Both vortices are still large as they both have a diameter in the order of the length scale of the harbour area. Furthermore velocities in the flood vortex are between 0.1 and 0.2 m/s, whereas velocities in the ebb vortex reach a maximum of 0.1 m/s.

To conclude, the model is applicable for tidal forcing. As said above the results of the neap and spring tidal runs are shown in the appendix and underwrite the conclusion.

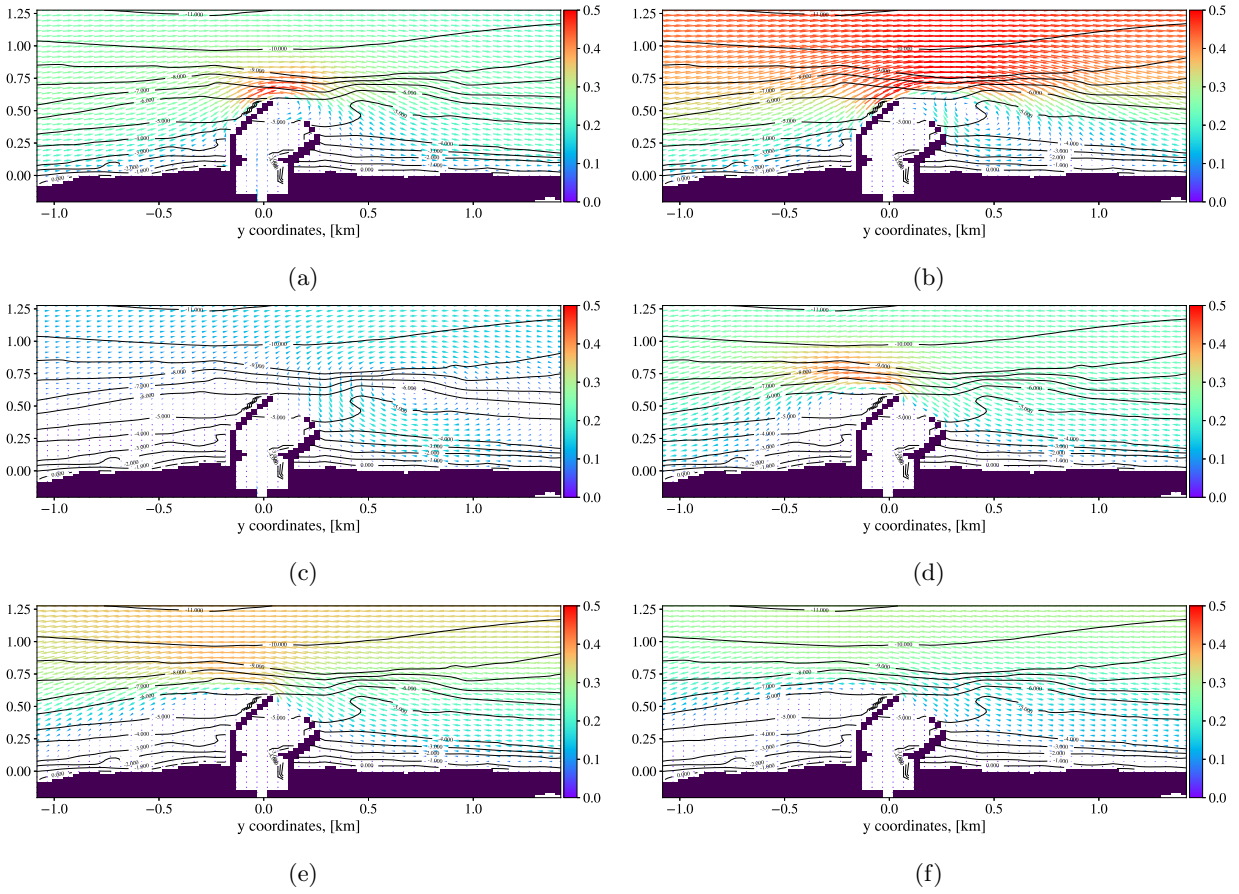

Figure 4.7: Vortex formation during ebb and flood phases. Plot a) flood flow at time T=29hr, a subtle ebb vortex starts to form at the northern mole. b) T=31hr, the ebb vortex has increased in size and starts to move northward. c) T=33hr, the flood vortex is released by the incoming ebb and has been shed. d) T=35hr, the ebb vortex develops near the southern mole. e) T=37 hr, the vortex has grown significantly in size as it is has a diameter of approximately the length scale of the harbour, which is $\mathcal{O}(700m)$. f) T=39hr, the vortex has now reached its full size and starts to shed from the harbour.

4.2 Waves

In this section the model behaviour on wave forcing is discussed. The location of the cross sections used are shown in fig. 4.1.
To determine which wave runs are applicable the offshore wave directions θ_0 from fig. 2.2 in section 2.1 have to be translated to nearshore wave angles θ at the boundary of the model. These waves typically have a period of 5-6 seconds. Therefore a value of T 5.5 seconds will be used as this is a common value for wind waves at the dutch coast (de Schipper et al., 2016).

Translating the offshore to the nearshore wave angles is done by using the dispersion relation and Snel's law. Snel's law states that for an alongshore uniform beach, following a wave ray:

$$\frac{sin\,(\theta)}{c} = constant \tag{4.1}$$

This means that the offshore wave angle and nearshore wave angles are simply related as follows:

$$\frac{sin\,(\theta_0)}{c_0} = \frac{sin\,(\theta)}{c} \longrightarrow sin\,(\theta) = \frac{c}{c_0} sin\,(\theta_0) \tag{4.2}$$

The wave period T does not change as waves approach the coast, but the wave length does change and consequently the wave number do. As the wave celerity c is dependent on the wave number and waver period the change in wave length must be accounted for. This can be done using the dispersion relation eq. 4.3, which relates the wave length L to the wave period T and depth d:

$$L = \frac{gT^2}{2\pi} tanh\left(\frac{2\pi d}{L}\right) \tag{4.3}$$

Using a mean period of $T = 5.5$ s, the measurement depth of d_0 30m and the depth d= 13.5 m at the model boundaries it is possible to calculate the nearshore wave angles. The result of the wave angle transformation is found in table 4.1, including the resulting refraction parameter.

Table 4.1: Refraction of wave angles for waves with a period of T=5.5 s from 30m depth to 13.5m depth

Offshore wave angle θ_0, deg RSN	Nearshore wave angle θ, deg RSN	Refraction parameter K_r
90	73	0.042
80	70	0.42
70	64	0.58
60	56	0.70
40	38	0.88
20	19	0.97
0	0	1.00

From the results in table 4.1 it is clear that the largest wave angle with respect to shore normal is 310-237 = 73 degrees. The maximum offshore wave height is $H_0 = 5$m. To transform this value to a nearshore wave height the shoaling and refraction parameters, K_s and K_r must be multiplied with the offshore wave height:

$$H = H_0 K_s K_r = H_0 \cdot \sqrt{\frac{c_{g,0}}{c_g}} \cdot \sqrt{\frac{cos\,(\theta_0)}{cos\,(\theta)}} \tag{4.4}$$

The shoaling parameter is only dependent on the two wave group celerities and has a value of $K_s = 0.95$. Using the shoaling and refraction parameters to calculate the maximum nearshore wave height from the offshore direction of 220 degN results in $H = 5 \cdot 0.95 \cdot 0.042$=0.2 m. With the breaker parameter γ of 0.73 these waves will break at a depth of $d = 0.3$ m. This wave height is too low to take as it will produce a very limited longshore current, and more importantly, it will dissipate over only one coastal cell in the model. Dissipation in only one cross shore cell is not enough to account for fluctuations in the longshore current in cross shore direction.

To properly account for the longshore current driven by wave breaking it is important that the model has a high enough cross shore resolution in which it captures the dissipation of wave energy. If the resolution is too low and wave breaking only occurs over a short cross shore distance the approximation of the shape and flow velocities of the longshore current are unlikely to be reliable. Therefore wave breaking has to occur over several coastal cells in cross shore direction. To ensure that wave breaking is well accounted for a minimum wave height must be determined. Therefore the the model is set up with wave forcing only. The waves have a wave height H_s = 0.5-4 m, angle of incidence $\theta = 260$ degN and period $T = 5.5$ s. In order to determine whether the model is able to accurately account for the longshore current due to wave breaking the cross shore extent of energy dissipation must be examined. A plot of a cross section of wave breaking in the cross shore direction is found in fig. 4.8. The exact location of the cross sections can be found on the map in fig. 4.1.

Figure 4.8 shows that for waves with a significant wave height of 0.5 m wave dissipation takes place over 60 to 80 m in cross shore distance. This is only three to four coastal cells. Comparing these results with energy dissipation of waves with a significant wave height of 1.0 m and larger shows already an improved cross shore resolution of five cells or more (see fig. 4.9).

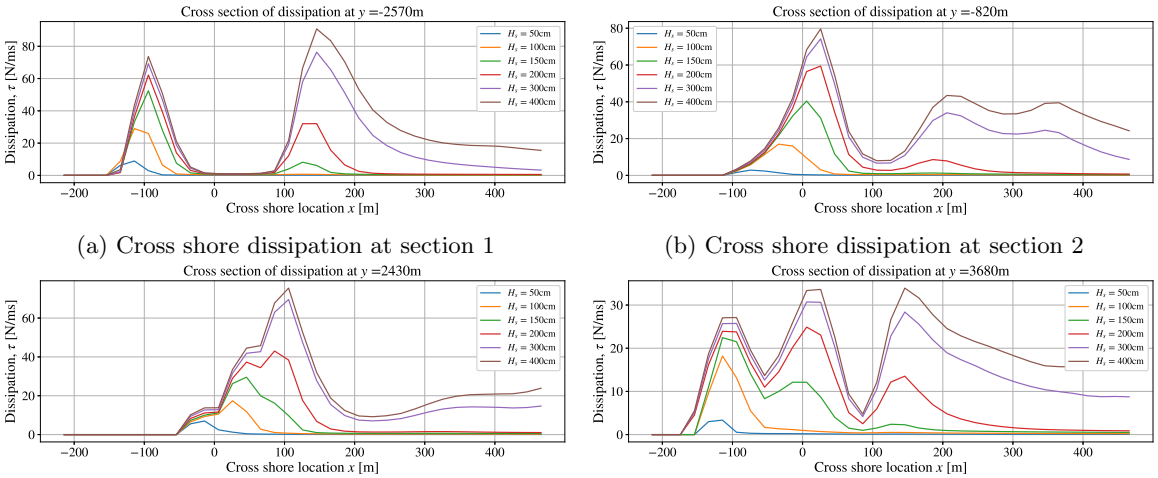

(a) Cross shore dissipation at section 1

(b) Cross shore dissipation at section 2

(c) Cross shore dissipation at section 3

(d) Cross shore dissipation at section 4

Figure 4.8: Cross sections in cross shore direction of wave dissipation τ_b due to wave breaking

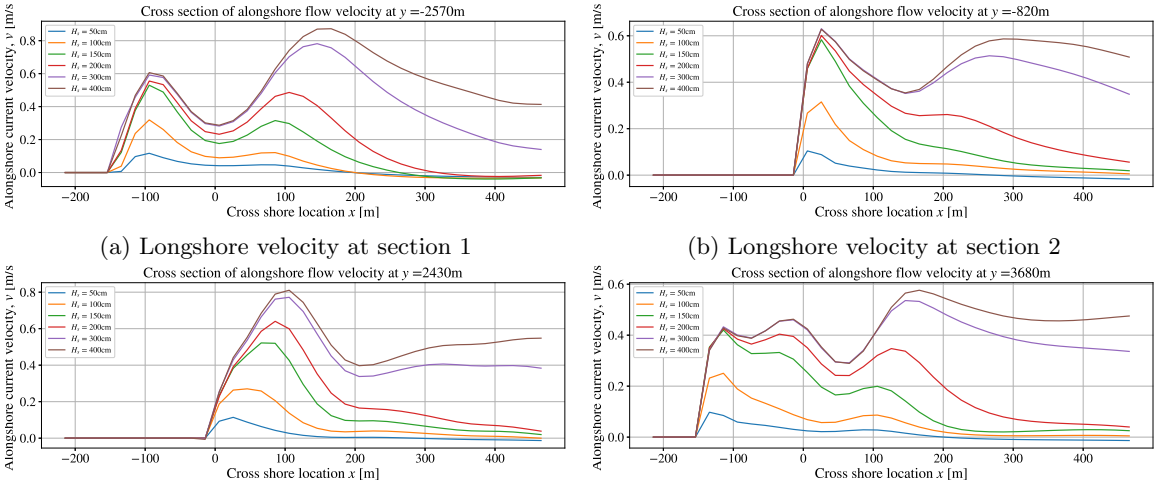

(a) Longshore velocity at section 1

(b) Longshore velocity at section 2

(c) Longshore velocity at section 3

(d) Longshore velocity at section 4

Figure 4.9: Cross sections in cross shore direction of the longshore current v

Comparing the cross sections of the flow velocities with the cross sections of the energy dissipation shows that the strongest flow velocities occur just after the waves start to break. Additionally, looking further seaward to both the velocity and wave dissipation shows that only a small amount of wave breaking already generates a current. This does out of proportion with the strong increase in dissipation and the much smaller increase in velocity, but the strong rise in bed shear stress in shallow water makes up for this imbalance. For example, comparing the longshore velocity, dissipation and bed shear stress at cross section 2 as shown in fig. 4.9c, fig. 4.8c and fig. 4.10c respectively shows that for $H_s = 4$ m that there is a very low dissipation rate at x=200 m. The flow velocity however is moderately high and the bed shear stress is at a local minimum. Moving shoreward to x= 100m the dissipation has increased seven fold, whereas the alongshore current increased only two fold. This must then be due to the increased bed shear stress, which is four times higher at this location. The same holds for the other locations.
The shape of the longshore current also shows the presence of horizontal mixing as the maximum velocity is located more shoreward than the point at which the waves start to break.

These findings are congruent with those from Longuet-Higgins (1970a), who showed that the maximum

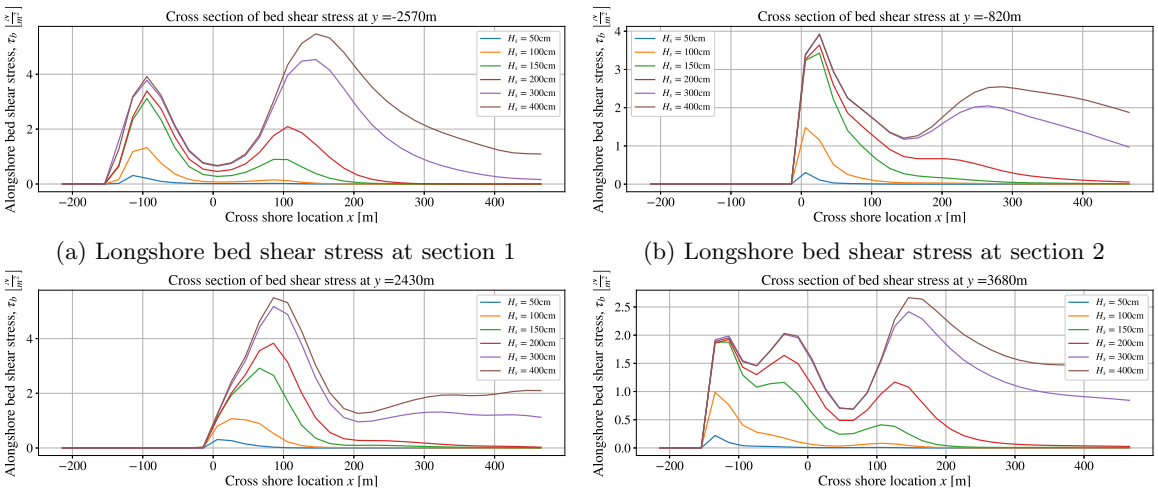

(a) Longshore bed shear stress at section 1

(b) Longshore bed shear stress at section 2

(c) Longshore bed shear stress at section 3

(d) Longshore bed shear stress at section 4

Figure 4.10: Cross sections in cross shore direction of the bed shear stress τ_b

velocity will take place between the breaker line and the shore face, and that due to continuity there must be a flow velocity outside the breaker line. From the comparison of these observations with the literature review leads to the conclusion that the restrictions for the applicable wave conditions are a minimal wave height of 1.0 m and a maximum angle relative to shore normal of 70 degrees.

Lastly the overall behaviour on wave forcing has to be checked. This can simply be done by examining the performance of the total flow field and the model boundaries. The total flow fields are found in fig. 4.11.

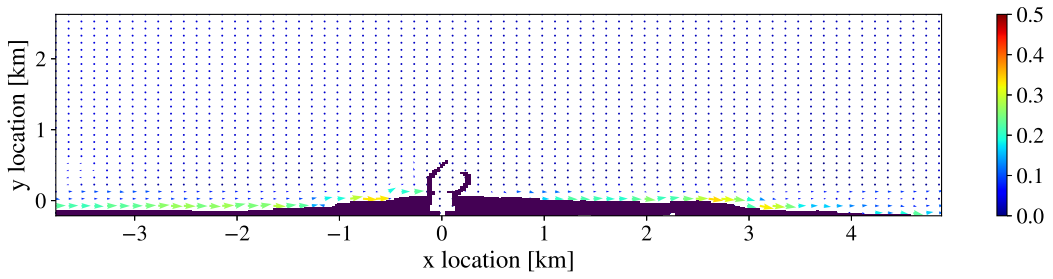

(a) Flow field for $H_s = 1.0$ m

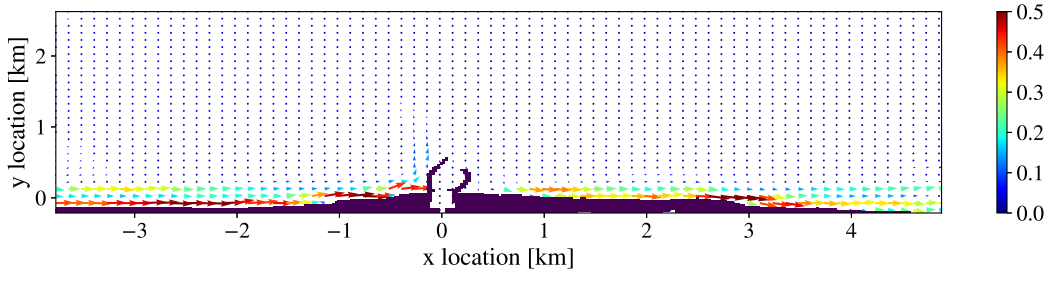

(b) Flow field for $H_s = 1.5$ m

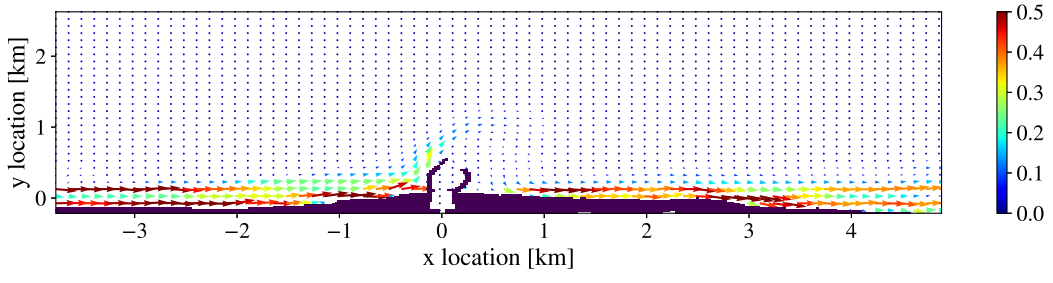

(c) Flow field for $H_s = 2.0$ m

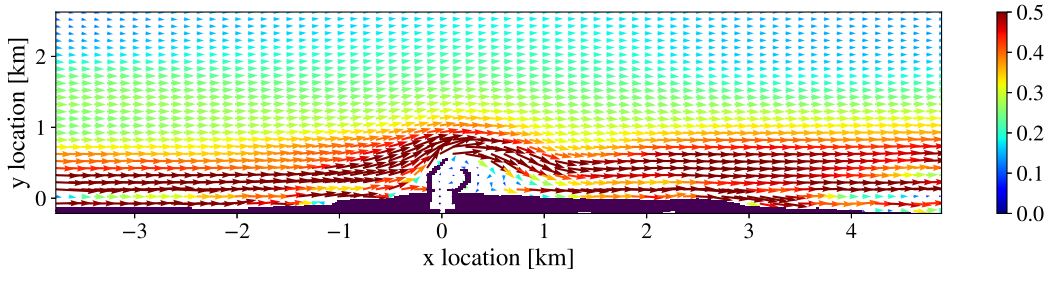

(d) Flow field for $H_s = 4.0$ m

Figure 4.11: Flow field in entire model domain for waves entering the domain from 50 degrees relative to shore normal with a period $T = 5.5$ s. Arrows show the direction and the colors the flow velocity.

For wave fields with $H_s < 2.0$ m the longshore velocity in deeper areas is opposite to the direction of the incoming waves (fig. 4.11c). This residual flow is most likely to be caused by the applied Neumann boundaries. Upon closer inspection it becomes clear that the the flow in deeper water is very limited when it is against the wave direction, as it is in the order of cm/s. This is verified in fig. 4.9. Comparing the residual flow to the flow in the surf zone, which is of $\mathcal{O}(0.2)$ m/s and higher. Therefore, the residual flow in the deeper section is negligible

Looking at the boundaries of the flow fields also no large inconsistencies are found (fig. 4.11). The locations that seems to show some error is in the shear band between the longshore flows in opposite directions at the edge of the surf zone. At this point the there is some recirculation of the flow where none is expected. In order to find out how far this error travels into the domain and how large it is, the total longshore flow in the surf zone will be calculated at several cross sections. When the total longshore flow no longer fluctuates the error is assumed to be negligible.

The total longshore flow is ideally calculated as:

$$Q = \int_{x_0}^{x_b} \int_{h=0}^{h=h} v \, dh \, dx \tag{4.5}$$

In which x_0 the shore line, x_b the breaker line, $h = 0$ the bottom of the water column, $h = h$ the top of the water column and v the depth averaged velocity. As indicated by Longuet-Higgins (1970a) and shown in the results above waves generate a current before the breaking point. Therefore the point at which a current starts to develop has been set to dissipation values of $\tau/\tau_{max} \geq 0.05$. The difference in total longshore flow ΔQ is then simply calculated as the difference in total flow between two adjacent cross shore cross sections as follows:

$$\Delta Q = Q_n - Q_{n+1}$$

The relative importance of ΔQ with respect to Q is then simply shown as $\frac{\Delta Q}{Q}$. This has been done for the cases of $H_s = 1.0$ m, 2.0 m and 4.0 m and can be found in fig. 4.12.

In fig. 4.12 the locations at which $\Delta Q \geq Q$ have been marked with dashed lines. Blue indicates total flow deviation between 10 and 100% and red indicates a difference of 100% or more. Differences at the model boundary are only of $\mathcal{O}\left(10^{-1}\right)$ and lower for all cases, meaning that boundary errors are very limited.

Incoming waves with a significant wave height of 1.0 m show the most deviations in longshore flow as can seen in fig. 4.12. The reason for this behaviour is most likely two-fold. First, the cross shore resolution of the wave dissipation is, as discussed above, lower than for higher wave heights. Second, as the wave heights are very small there is relatively small longshore current. This means that when changes in breaking in longshore direction occur it has a relatively high impact on the total longshore current.

Nonetheless, main differences in total longshore current occur in the harbour area. This was expected as the current is interrupted by the moles. The larger the wave height, the lower the changes in longshore current. This is most likely due both due to the previously discussed width of the resolution of the surf zone as well as its width. Waves with H_s=2.0 m have a surf zone which ends at a depth of approximately 4m, meaning the moles are not fully contained by the surf zone. Waves with H_s=4.0m the surf zone ends at roughly 8m depth. This is well beyond the moles, such that the longshore current is only partially obstructed by the harbour.

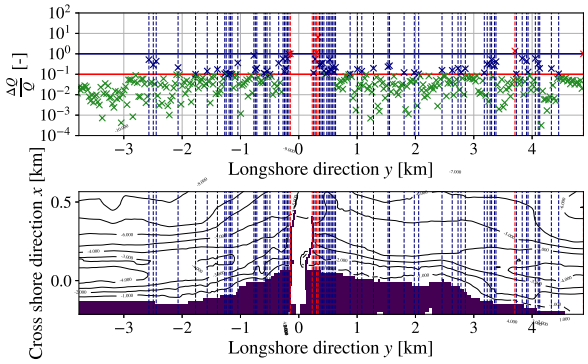

(a) Fluctuations in total longshore flow for $H_s = 1.0$ m

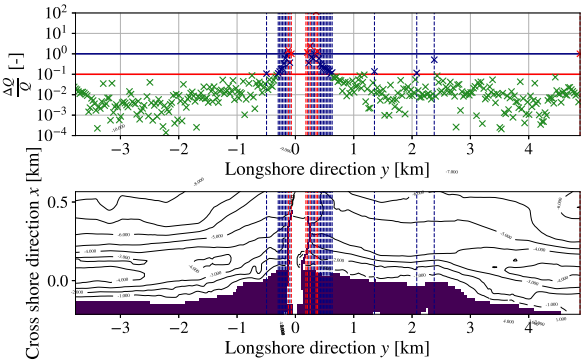

(b) Fluctuations in total longshore flow for $H_s = 2.0$ m

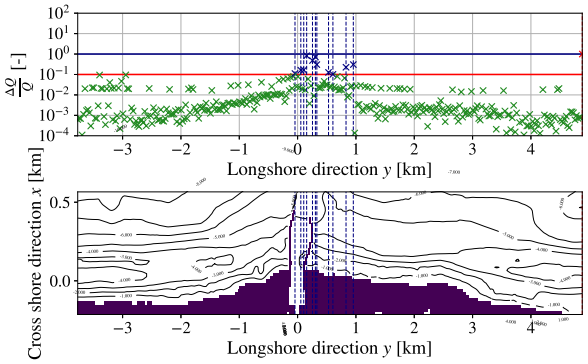

(c) Fluctuations in total longshore flow for $H_s = 4.0$ m

Figure 4.12: Differences in total longshore flow. Locations where $\frac{\Delta Q}{Q} \geq 0.1$ are marked with red dashed lines and the locations at which $\frac{\Delta Q}{Q} \geq 1$ are marked with navy blue.

4.3 Wind

Wind forcing is the last component that will be analyzed in this chapter. For this purpose wind speeds of 1.5, 3.0, 4.5, 6.0 and 9.0 m/s will be examined with angles of 50 and 90 degrees relative to shore normal. First, the entire flow field and boundaries will be examined during conditions with wind speeds of 3.0, and 9.0 m/s, with angles of 50 and 90 degrees to shore normal (fig. 4.17).

The plots in fig. 4.17 show the velocities and the directions of the flow due to the wind speed. Overall the behaviour of the flow fields look similar to the findings in section 2.3.3 where the flow velocities mainly developed in the longshore direction. Similarly, the flow velocities in the field per wind speed are of the same order for different wind angles. For 50 degrees relative to shore normal the alongshore flow near the shoreline is $\mathcal{O}(0.03m/s)$ whereas for 90 degrees relative to shore normal this is $\mathcal{O}(0.05m/s)$. For both directions and wind speeds the development of the flow field in the harbour area seems to perform well.
The boundaries however reveal that for low wind speeds there is an area with some irregular behaviour. This starts at the top left corners of fig. 4.17b and fig. 4.17a. These show a slight deviation in the flow velocity and direction with respect to the rest of the flow field. In this area the flow direction has a shoreward component. Additionally, for both wind directions with a wind velocity of 3.0 m/s there are at the left boundary just below $y = 1.0$km high flow velocities compared to the rest of the flow field. This seems to be only a local error as the flow decelerates further into the domain.

To further investigate how far this boundary error travels into the domain the impact on the total longshore flow will be analysed. This is done by calculating the longshore flow as was done for wave validation, with

the single difference that in this case the current will be calculated from a set depth to the shoreline instead of the breaker depth. This depth is chosen at 10.5m as it will include the above discussed error. The result is shown in fig. 4.13.

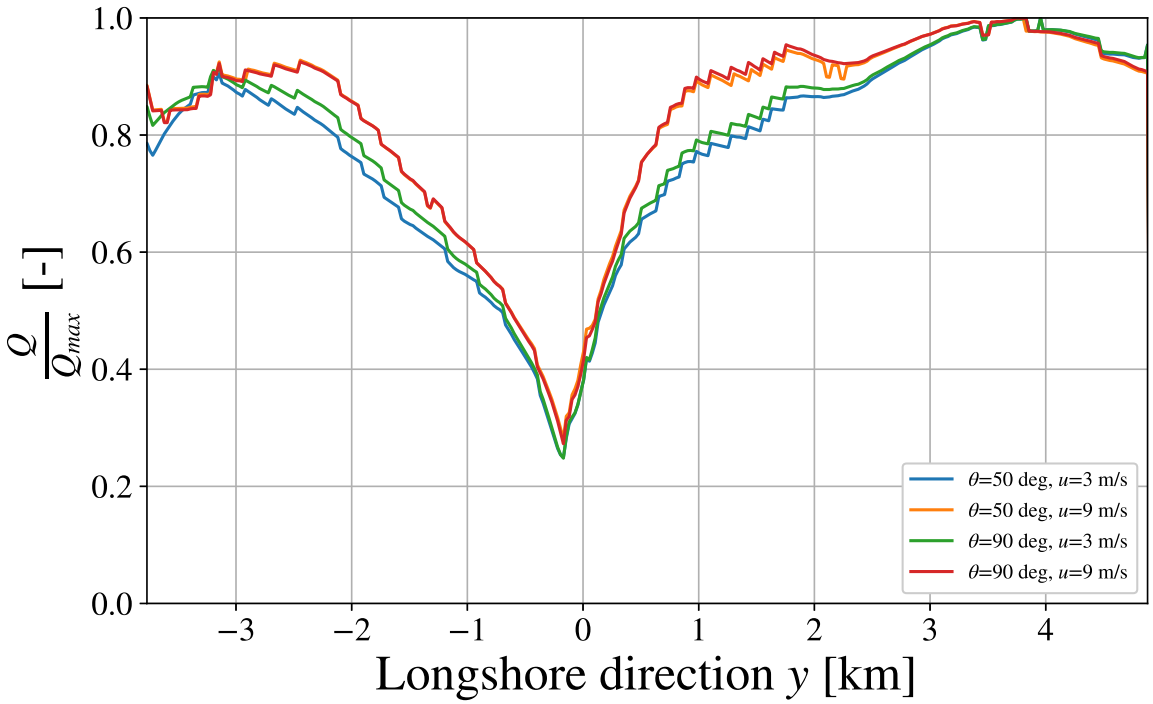

Figure 4.13: Longshore current divided by maximum longshore current $\frac{Q}{Q_{max}}$ for different wind velocities and directions.

From fig. 4.13 it is clear that the impact of the strong flow velocities around x=0.9km is very limited. A small decrease in the longshore current does occur as the flow decelerates further into the domain, but the extent is very limited. After a few hundred meters the effect is no longer noticeable.
The figure shows a decline starting around x=2.5 km towards the harbour area. This is the effect of the flow obstruction by the harbour moles. The impact is equally large on both combinations of flow velocity and wind direction, suggesting that they have a very similar longshore flow pattern in cross shore direction (Figure 4.12). Another interesting feature is that just behind the harbour area, starting at x=0.15km, initially the larger wind velocities reach the near maximum velocities faster than the lower wind velocities. This is likely to be the effect of the non-linear interaction between wind drag and the flow velocity.

Looking at the longshore current cross sections in fig. 4.14 and fig. 4.15 reveals that the depth averaged longshore have a steep rise for 20 to 40 meters from the shoreline, which is about 2 cells in cross shore direction. For lower wind velocities the maximum is almost reached at this point whereas higher intensity winds may still produce higher flow velocities further offshore. As found in section 2.3.3 the findings from Murray (1974) suggest that when the wind direction is completely parallel to shore the flow influence on the flow velocity is somewhat lower than 5% of the wind speed at 2m deep in a 6 to 12m deep water column. For example, when taking a wind direction of 50 degrees to shore normal at location x=-2570m and dividing the most offshore flow velocities by the wind velocity values around 1.3 for wind speeds of 1.5, 3.0 and 4.0 m/s and values around 2.1% for 6.0 and 9.0 m/s. This is comparable to the values found by Murray (1974) considering the fact that flow velocities decrease lower in the water column. Estimating the mean flow velocity as percentage of the wind velocity for water columns of 6 and 12 m with 3% velocity values at 2m deep would then yield:

$$u(h=6m)_{flow,mean} = \frac{1}{2} \cdot 3 \cdot \frac{6}{4} = 2.25\% \quad u(h=12m)_{flow,mean} = \frac{1}{2} \cdot 3 \cdot \frac{12}{10} = 1.8\%$$

This shows that when assuming a triangular velocity profile over the depth flow velocities would be very similar. In reality the profile is highly non-linear and has at the top a flow velocity close to the wind velocity. With increasing depth the flow velocity decreases rapidly. This is however still likely to yield similar results in terms of the depth averaged flow velocity.

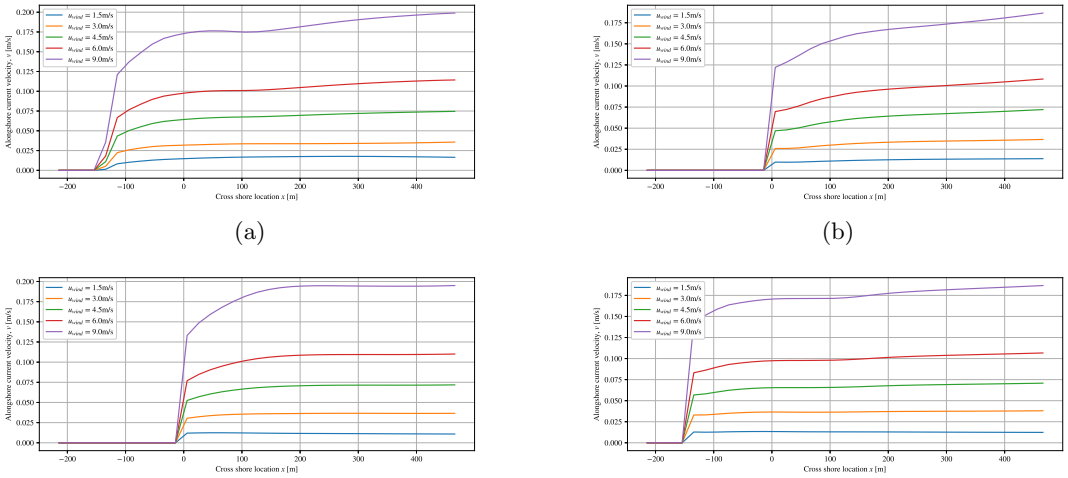

(a) (b)

(c) (d)

Figure 4.14: Cross sections in cross shore direction of the longshore flow velocity due to wind for a wind direction of 50 degrees to shore normal

Lastly, the spin-up time for the wind driven currents will be discussed. As found in the literature review wind driven currents take approximately a day to fully develop. Model findings are shown in fig. 4.16.

Figure 4.16 shows that globally speaking the longshore flow development takes longer in deep water than in shallow water. This finding is similar to the finding in section 4.1 where the deeper areas took longer to adjust to the flow regime due to the larger water mass which has to be set into motion. The time it takes for the model to adjust seems to be mainly dependent on the wind velocity. Higher wind speeds lead to a faster spin-up time. Additionally the wind direction also seems to have a minor influence on the flow adjustment, with winds more parallel to shore leading to a lower adjustment period.
The spin-up time as found in (Bosboom & Stive, 2015) seems to be a good first estimate for the time it will take for the flow to adapt, with only slight increases in the the longshore flow velocity if the maximum is not yet reached.

4.4 Conclusion

With the found results for tide, wind and wave the model seems applicable to all proposed conditions, with a minimal required significant wave height of 1.0m. This minimal wave height is due to the cross shore resolution of wave breaking and the longshore current.
Errors found at the boundaries were found to be restricted to the edges of the domain without having a noticeable impact on the longshore flow.

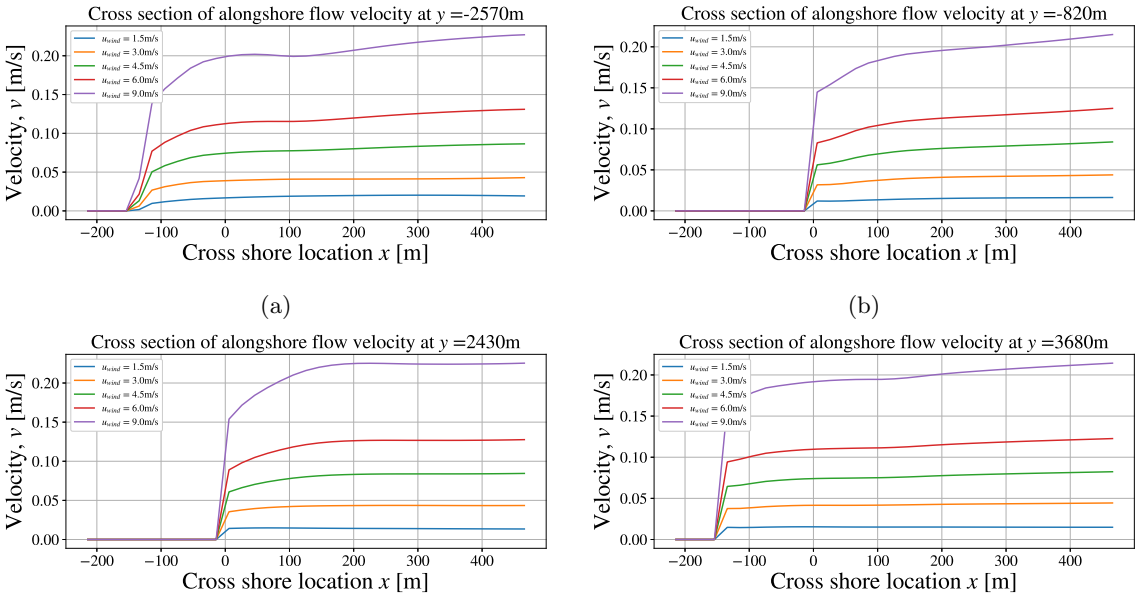

Figure 4.15: Cross sections in cross shore direction of the longshore flow velocity due to wind for a wind direction of 90 degrees to shore normal

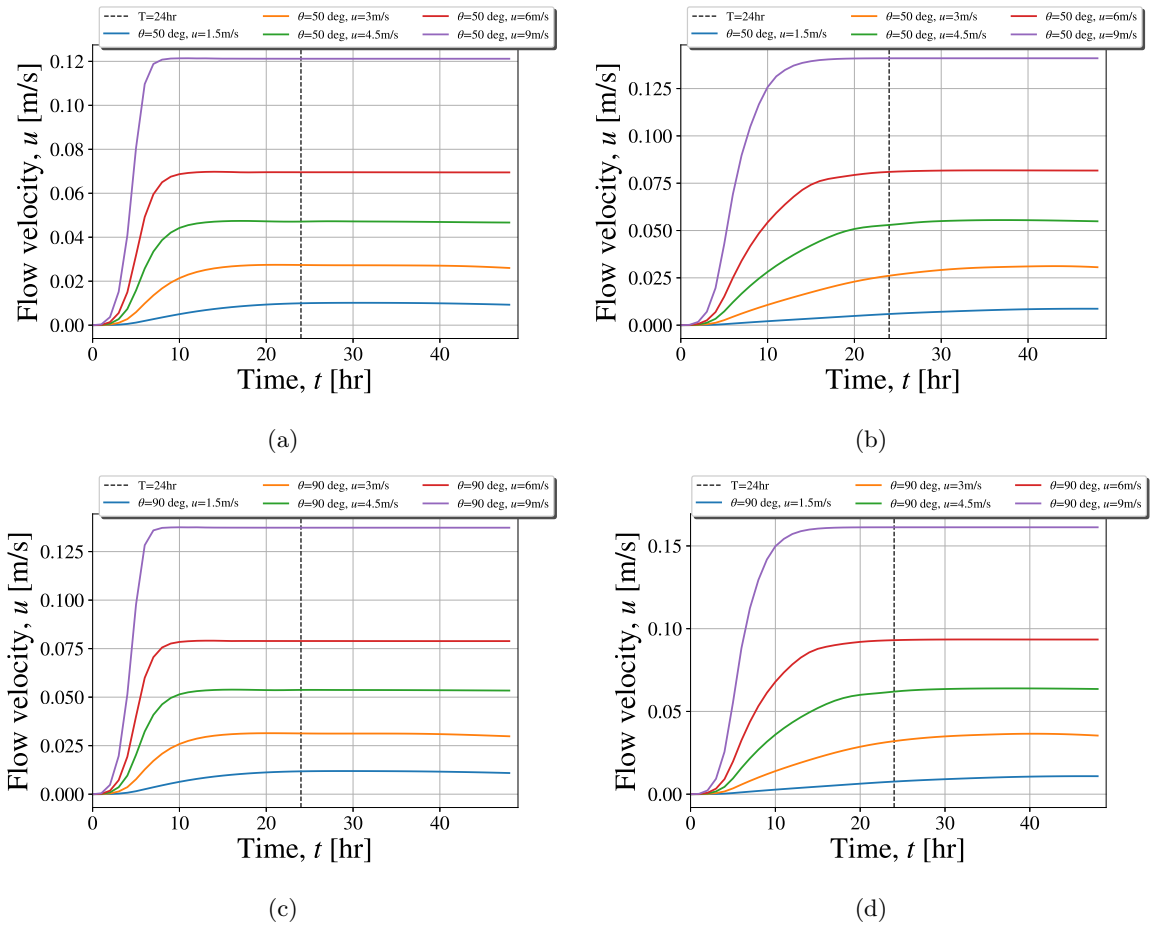

Figure 4.16: Development over time of longshore wind driven current. a) 50 degrees to shore normal, shallow water. b) 50 degrees to shore normal, deep water. c) 90 degrees to shore normal, shallow water. d) 90 degrees to shore normal, deep water.

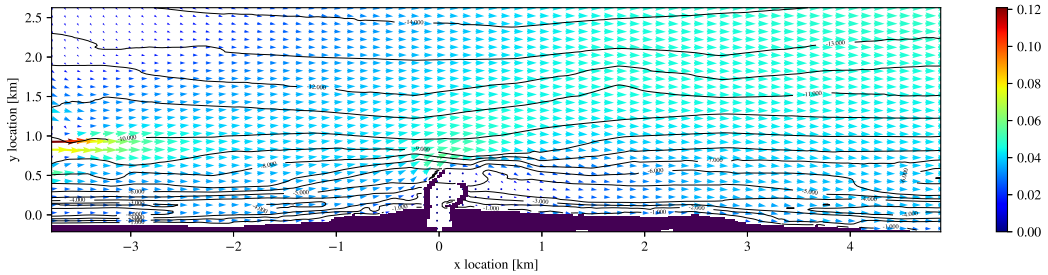

(a)

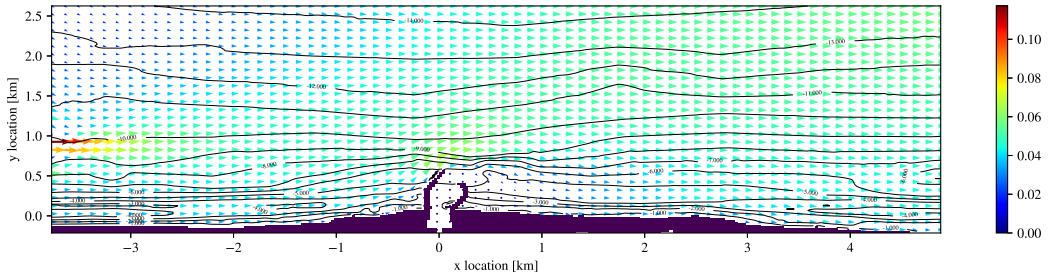

(b)

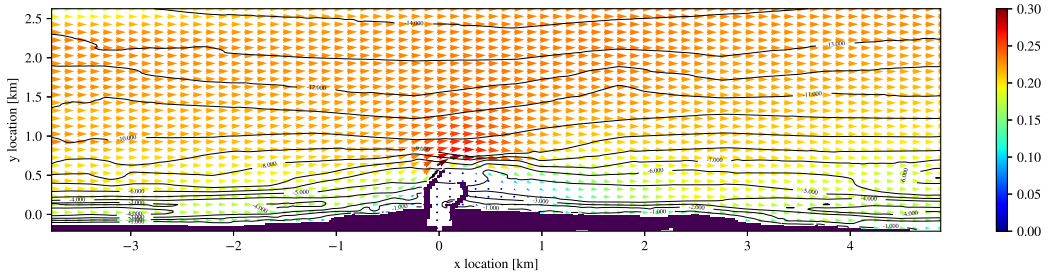

(c)

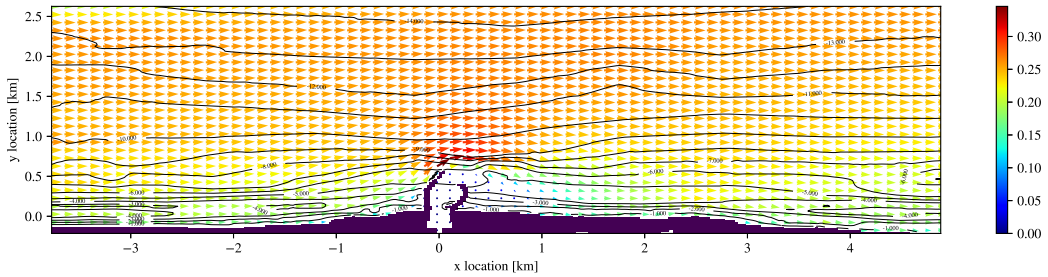

(d)

Figure 4.17: Flow field in entire model domain for wind entering the domain from 0 degrees relative to shore normal. Arrows show the direction and the colors the flow velocity. a) Flow field of wind from 50 degrees relative to shore normal and u_{wind}=3.0m/s. b) Flow field of wind from 90 degrees relative to shore normal and u_{wind}=3.0m/s. c) Flow field of wind from 50 degrees relative to shore normal and u_{wind}=9.0m/s. d) Flow field of wind from 50 degrees relative to shore normal and u_{wind}=9.0m/s.

5. Rip Current Analysis

In this chapter rip currents in the validated model are investigated by means of virtual drifters. The analysis performed on the formed boundary rips will focus on rip characteristics such as exit rates, rip velocities and rip head locations.
This chapter starts with a general outline of the approach including a table with the parameters and definitions. Then the virtual drifters will be described. Thereafter wind, wave and tide are analyzed individually. Lastly combinations of wind, waves and tide are made which are then compared to the individual forcing mechanisms.

5.1 Approach

Both single and multiple forcing conditions will be analyzed for rip currents. In nature there is oftentimes not a single condition such as tide, wind or waves at a time but most likely all or at least two occurring simultaneously. Dissecting the system has as benefit that it gives insight in the impact of a single forcing on the system. Making combinations of the separate parts it will help in identifying the causes of the behaviour of a rip. Single conditions are thus used as handles for the more complicated combinations. Still, as the interactions are non-linear not all cases can be compared as a sum of the parts.

To obtain a full data set combinations of wind, wave and tide are made. As limit for the wave height a significant wave height of 4 m is used. Although maximum wave heights at Scheveningen are 5m, these only occur only during storm conditions. It is unlikely that people will enter the water with waves this height during a storm and is therefore not considered. Therefor wave heights are taken up to 4m to account for extremes, and combined with a wind speed of 9 m/s.
Also the directions of wind and waves is important. As discussed in section 3.3 incoming waves refract when approaching the coast. This means that the point at which waves are generated by the wind has a different wave angle than at the nearshore. Additionally, it is assumed that the wind direction is similar to the nearshore location as the Europlatform, the location from which the wave statistics are obtained, lies only 30km from the coast. Combined with the fact that wind waves have a relatively high directional spreading it seems only natural to have several runs with one wave height and wave angle of incidence and a different wind direction.
For tidal runs and combinations including tidal motion three tides are analyzed. These are neap, spring and regular tide, with the latter being in between neap and spring tide. These three are considered since spring tide comes with higher flow velocities and more extreme water levels, whereas neap tide has lower flow velocities and a reduced water level amplitude. The regular tide will be analyzed because it occurs most frequently.

All three forcing mechanisms will have discretized inputs in order to make the results workable and comparable. For wave runs all waves have a period of 5.5 seconds as this is the mean value found for waves along the coast of The Netherlands. This is a simplification as in reality wave periods are related to the wave height. The used wave heights are as follows: 1.0, 1.5, 2.0, 3.0 and 4.0m. The directions are -70, -50, -30, 0, 30, 50 and 70 degrees RSN.
The discretized wind cases are as follows: wind velocities: 1.5, 3.0, 4.5, 6.0 and 9.0 m/s with wind directions of -70, -50, -30, 0, 30, 50 and 70 degrees RSN. The combinations for waves are tabulated in table 5.2 and for

Parameter	Definition
Total amount of drifters	100
Drifter run time	60 minutes
Rip	v_{median} ≥0.1 m/s
Hazardous rip	v_{median} ≥0.3 m/s
Exit	$x_{drifter}$ >0.41 km
Overshoot	$y_{drifter}$ <0.15 km
Retentions	100 - n_{exits}

Table 5.1: Parameters and their definitions

wind in table 5.3.
For the tide it is not possible to discretize in the same manner, but it will be done on the basis of the tidal period. Considered cases are: 2hr before high water, high water, 2hr after high water, mean water level , 2hr before low water, low water and 2hr after low water.

In the model rips will be identified by measuring flow velocities in the model area, which is depicted in fig. 5.1b by the white dots. Measurement of the flow velocities for wind and wave cases takes place at a single point in time near the end of the run. This is because the flow will become stationary over time. For tidal runs seven points in time are chosen as the water level and flow velocities fluctuate over time. These are the same points in time as discussed above.
From the measured velocity points the median value of the flow velocity will be calculated, as well as the minimum and maximum velocities. The median velocity gives a better overall view of the velocity in the area as it shows the value of the center of the velocity distribution. A rip is defined as having a median velocity of 0.1 m/s. Consequently a rip is considered potentially hazardous when the median value of the velocities is greater or equal than 0.3 m/s. In turn this metric allows for the identification of the conditions during which a rip is formed and if this rip is potentially dangerous based on the rip velocity.

Virtual drifters will be deployed to find the velocities in a drifter trajectory and to identify the transport pattern. The velocities of the drifters are used to analyze the potential hazard of each condition regardless of rip occurrence. Transport patterns will be obtained from the drifter end locations after one hour of virtual drifter run time. Drifter release locations are shown in fig. 5.1b as white crosses.

Drifter exits are simply calculated as the drifters that leave the surf zone in one hour. The surf zone is however dependent on the wave height and it differs per case how far a particle is transported offshore. Therefore it seems more suitable to choose a location as offshore limit. As the location under investigation is around the northern harbour mole the offshore extent of this mole will mark the border between exit and retention. This border is located at cross shore location x=0.41 km (marked in fig. 5.1a by the red dotted line).
Another question of interest is whether or not drifters may stay north from the harbour mole or travel southwards from it. This is defined as an overshoot and occurs when a drifter passes the line located at longshore location y=0.15 km (marked in fig. 5.1a by the black dotted line).
Transport patterns are defined on the basis of the location of the drifter end location. This is then translated to the aforementioned exit, retention and overshoot regions. From literature it is found that boundary rips are very narrow compared to the longshore flow. The location in the vicinity of the northern mole where the rip flow velocity will be obtained is depicted with white dots in fig. 5.1b. If the flow velocity in this area is 0.3 m/s or higher it is defined as a hazardous rip, otherwise it is not regarded as such (see also table 2.2).
An overview of all the aforementioned parameters and their definitions is shown in table 5.1.

5.2 Virtual Drifters

The virtual drifters used to assess the rip transport patterns use the advection scheme as described in section 2.4.1. The inputs used are the x and y coordinates at the drifter release and the Delft3D outputs

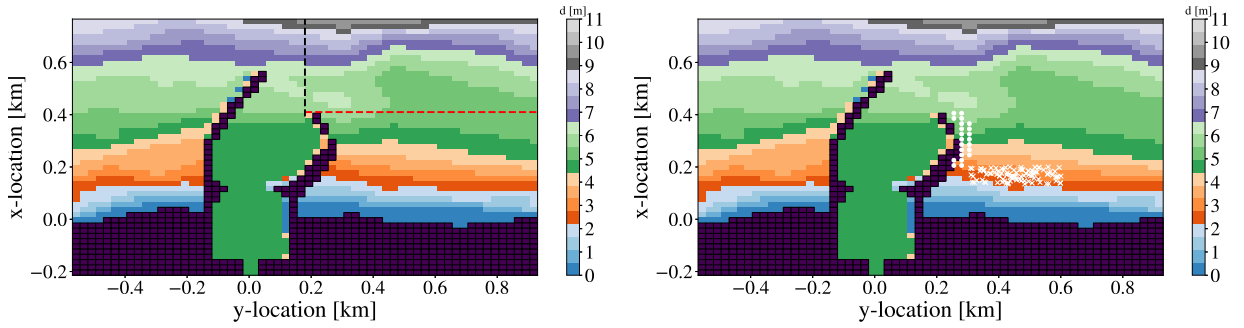

(a) (b)

Figure 5.1: a) Figure with retention, exit and overshoot domains. Below the red dotted line is the retention area. The exit area contains the area above the red line and also left of the black line. The overshoot area is left of the black line. b) Map showing the area in which the rip current is measured in white dots. White x's are the locations at which drifters are released.

containing the flow velocities of a run. Once released the drifters use the velocity at the current point in both time and space to calculate the next position using the advection scheme.
Delft3D outputs are discretized in grid points containing velocity data and the time series having a time step of one hour, whereas the drifters run for one hour. This means that the velocities of the flow field have to be interpolated over time and space. This is done by means of linear Lagrange interpolation. Time interpolation takes place between two subsequent time stamps of the velocity field. The amount of time steps to be obtained from the interpolation depend on the maximum allowed time step for the numerical integration scheme used to calculate the transport pattern.
For numerical integration the Runge-Kutta 4 scheme is used, which is an explicit integration method. In order for an explicit method to be stable and yield reliable results it needs to fulfill the CFL condition, which states that the following conditions must hold:

$$\frac{u\Delta t}{\Delta x} + \frac{v\Delta t}{\Delta y} \leq 1 \tag{5.1}$$

For all cases a time step of $\Delta t = 10$ seconds is chosen. This means that the amount of discretized time steps resulting from the interpolation must be 360, including the start and end points. The velocity is then interpolated between the start end end points for each newly discretized point in time.
At each of these discretized time points a space interpolation will be performed. To this end the values of the velocities found at the corners of a grid cell in which the drifter resides are used. The velocities at the grid cell corners are then interpolated to estimate the velocity at the drifter location. A schematization of interpolation in space and time is shown in fig. 5.2. Each rectangle is a grid cell obtained from time discretization and shows with the drifter location marked by the circle. The corners of the rectangle have the x, y, u and v values, which are all interpolated in space to find the coordinates and velocities at the drifter location. The drifter then uses the RK4 integration method to take one step in time to obtain the following drifter location, with the drifter path depicted by the dotted line with arrow.

The functions used for numerical interpolation and numerical integration can be found in appendix A. appendix A.1 shows the interpolation function, appendix A.2 shows the integration function and **??** shows two functions for finding the corner points of the grid cell in which a drifter resides, one for the x coordinates and the other for the y coordinates.

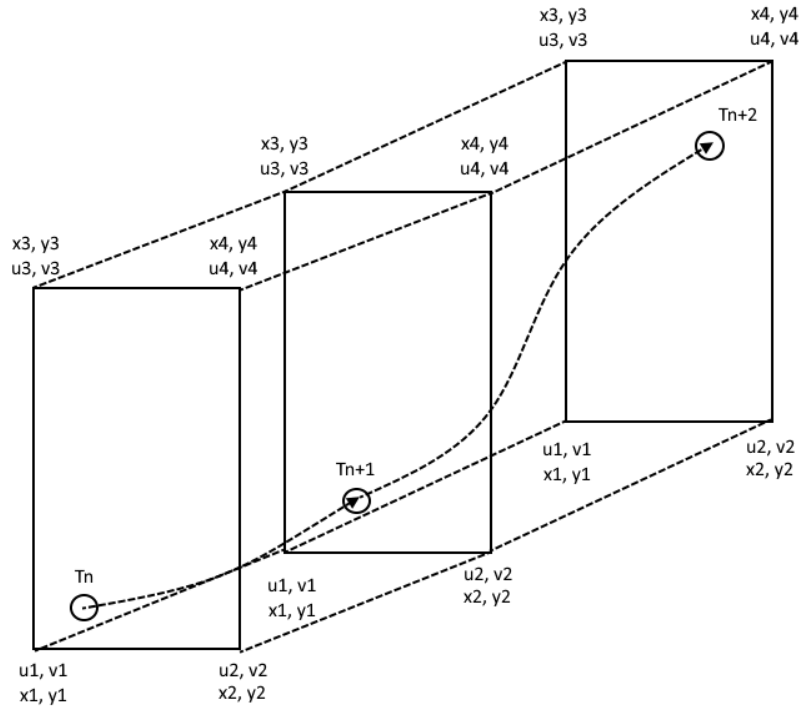

Figure 5.2: Schematization of interpolation in time and space.

5.3 Single Forcing Mechanism

In this section the results of the single forcing mechanisms are analyzed.

5.3.1 Tide

Virtual drifter measurements for the tide are performed for a spring tide, neap tide and a tide in between these two. Drifters are released in the model during the moments in time as described in section 5.1. Figure 5.3 shows the tidal signal for a spring tide. The moments of drifter release are marked by black markers. Virtual drifters are also released during neap and regular tides on similar moments of the tidal water level signal.
The spring tidal cycle has the largest water level differences and the highest flow velocities, both in ebb and flood direction. Water level differences are approximately 2.1 m between flood and ebb. Ebb flow velocities are 0.5 m/s whereas flood velocities are 0.6 m/s.
Both flow velocities and water level differences are significantly lower for the regular tide and the neap tide. Between these two the neap tide has the lowest flow velocities and water levels. Values are 0.4 m/s for flood flow and 0.35 m/s for ebb flow. The regular tide produces flow velocities of 0.4 m/s for ebb and 0.45 m/s for flood flows.

Flow velocities along the northern harbour are shown in the lower plot of fig. 5.4. Spring tide is depicted with blue markers, normal tide with red markers and neap tide green markers. The figure depicts the total range of velocities found at each tidal phase, with the extrema depicted by - markers and the medians by dots. A negative velocity in this figure means that the flow is directed towards the shore. Examination of the results show that rips occur as median velocities reach values of 0.1 m/s and higher for spring tide during mean water level to high water level. All median flow velocities are below 0.3 m/s, meaning that on the basis of the velocity criterion no hazardous rips occur.
Most exits take place during medium to high water, which coincides with the larger flow velocities. This is similar for the overshoots, except that no overshoots occur during the high water peak. As found in

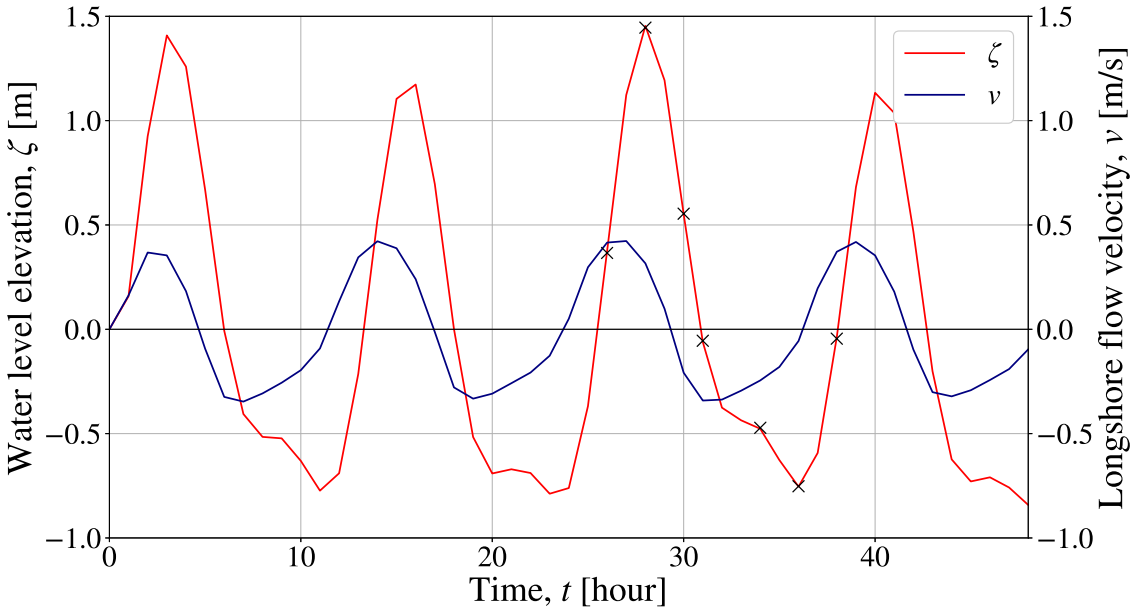

Figure 5.3: Tidal signal during spring tide, with the flow velocity taken in shallow water. Water level is plotted in blue and longshore flow velocity in red. The marks are chronologically: $T_{high} - 2hr$, T_{high}, $T_{high} + 2hr$, T_{mean}, $T_{low} - 2hr$, T_{low} and $T_{low} + 2hr$.

section 4.1 a vortex forms at the northern harbour mole during high water. Initially this vortex is small and restricted to the entrance of the harbour area for neap and regular tides. During spring tide the vortex is already quite developed with flows strong enough to force drifters to exit and even overshoot the northern mole.
When the tide reaches high water the vortex at the northern mole is fully developed. Most drifters exit the area but none overshoot.
From high water to low water the flow velocities are negative. In this range of the tide exits mainly occur when the water level is above mean water level. When the water level has dropped below mean water level exit rates are only found to occur sporadically during the neap, spring and regular tides. An overview of the overshoots and exits during several tidal phases can be found in fig. 5.4 in the top and middle panels respectively. Examples of drifter trajectories during high water and two hours thereafter are shown in fig. 5.5a and fig. 5.5b respectively.

Mean drifter velocities seem to be in correspondence with the water level. From mean water to high water drifters show an increase in mean velocity. From high to low water velocities generally decrease, with at low water most mean drifter velocities less than 0.05 m/s.
It is likely that the low flow velocities during low water are linked to the water level. When the water becomes very shallow the tidal flow becomes dominated by the bed shear. This likely to be the cause of the reduced flow velocities.

To conclude, tidal motion in itself does not lead to a potentially hazardous rip current based on the flow velocities. Exits and overshoots occur for drifter velocities below the velocity threshold value. These are linked to the higher velocities which occur during high water.

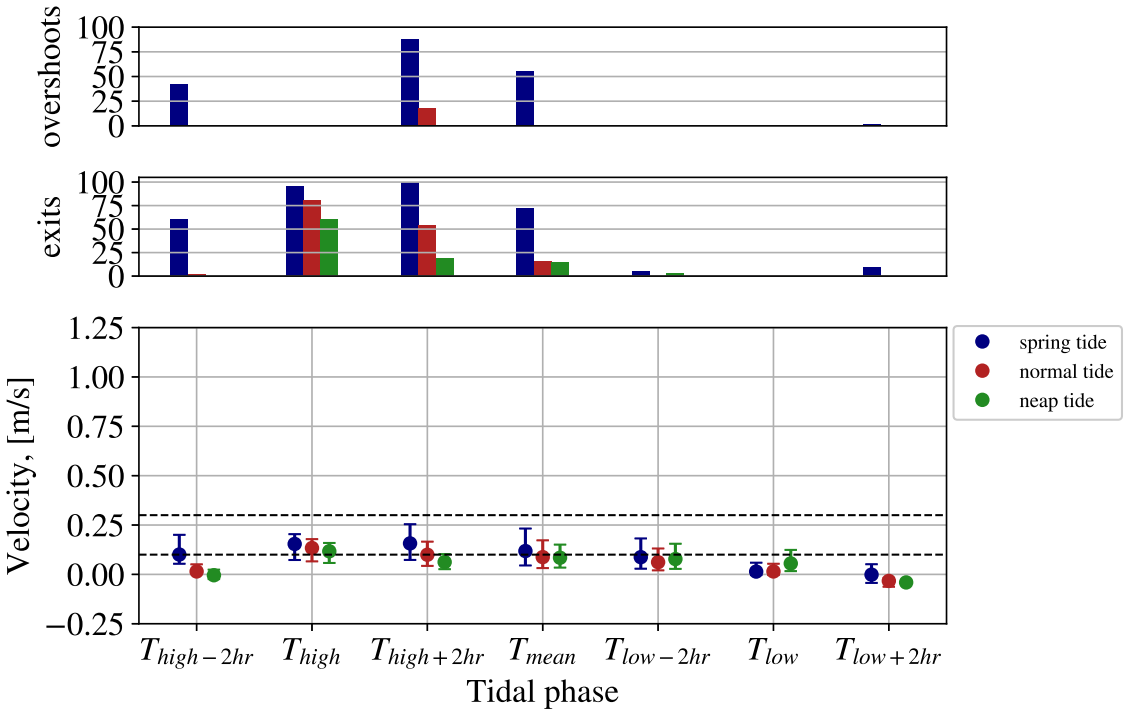

Figure 5.4: Velocities along the northern harbour mole for spring, neap and normal tides during various tidal phases, combined with overshoots and exits. Top panel: overshoots. Middle panel: exits. Lower panel: flow velocities along the mole; including the median value (dots) and minimum and maximum values.

5.3.2 Waves

Wave forcing is applied to the model with significant wave heights ranging from 1.0 to 4.0 meters and angles of incidence ranging from -70 to 70 degrees relative to shore normal. The combinations of wave angle and wave height can be found in table 5.2.

Angle of incidence, θ [deg RSN]	Significant wave height, H_s [m]
70	1.0, 1.5, 2.0, 3.0, 4.0
50	1.0, 1.5, 2.0, 3.0, 4.0
30	1.0, 1.5, 2.0, 3.0, 4.0
0	1.0, 1.5, 2.0, 3.0, 4.0
-30	1.0, 1.5, 2.0, 3.0, 4.0
-50	1.0, 1.5, 2.0, 3.0, 4.0
-70	1.0, 1.5, 2.0, 3.0, 4.0

Table 5.2: Modeled runs with only waves. Each angle of incidence is modeled separately with each wave height.

Velocities forced by waves coming from -70 to 0 degrees RSN do not lead to drifter velocities above 0.3 m/s for any significant wave height, meaning that these waves alone do not produce a potentially hazardous boundary rip current. Some exits and overshoots occur for drifters which start closest to the harbour mole. These seem to be occurring due to shadow rip formation. Similar to Pattiaratchi et al. (2009) the drifters at the mole side of the flow divide move towards the harbour mole and are caught in a shadow rip. The other drifters float to the North, away from the harbour mole. The offshore extent of the shadow rip seems to be positively correlated with the wave height, meaning that increasing the wave height also increases the

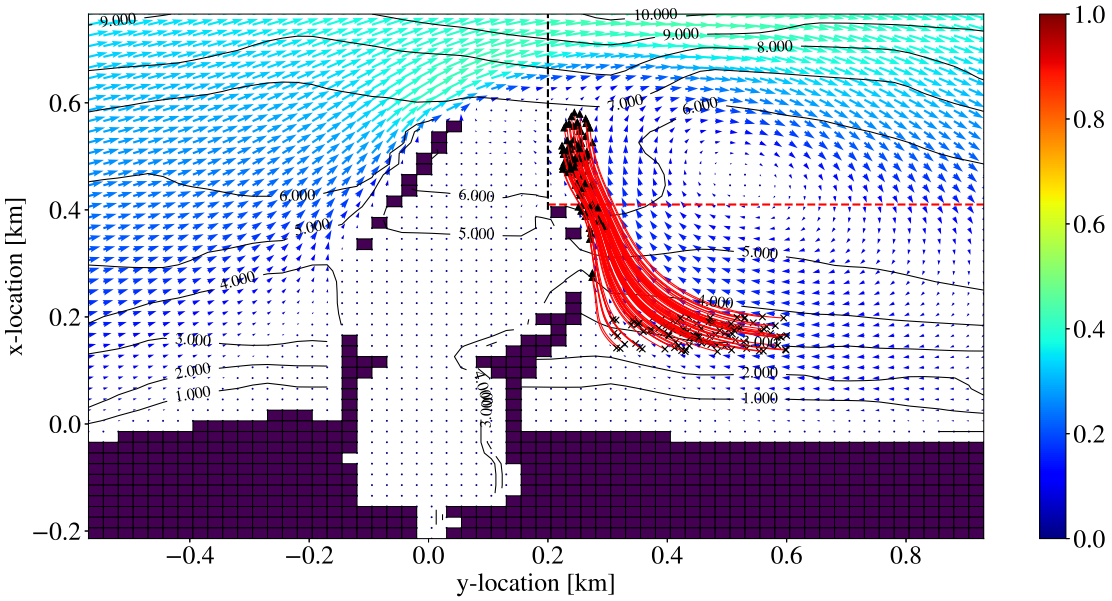

(a)

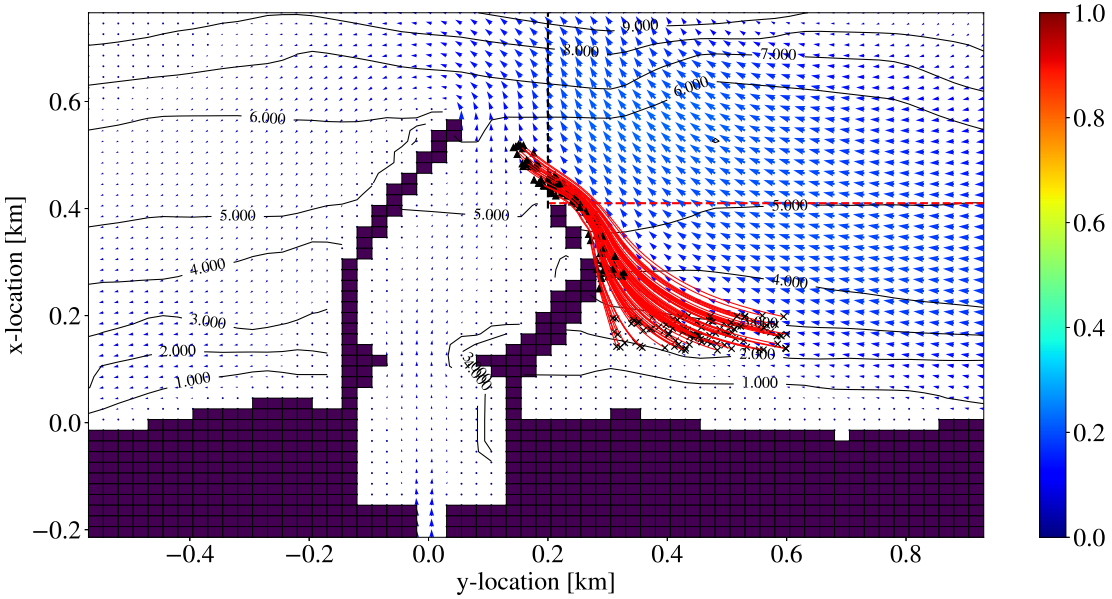

(b)

Figure 5.5: Drifter trajectories for a normal tide during high water (top panel) and two hours after high water (bottom panel). Drifter trajectories are shown with the red lines, drifter start positions are marked by black crosses and end positions with black triangles. The arrow color indicates the flow velocity in m/s. Flow fields are the instantaneous flow fields of the respective tidal phases.

offshore extent of the shadow rip. The velocity data however do not seem to agree with the drifter patterns as most of the found velocities are below 0.1 m/s and for wave heights smaller than 2m these are even negative. The discrepancy is most likely caused by the location of the measured points. This is because they lie next to the harbour mole starting at approximately half its length up to the mole tip, and the rip does not extend to the measurement points. Therefore no rip is observed during low waves. An example is shown in fig. 5.6.

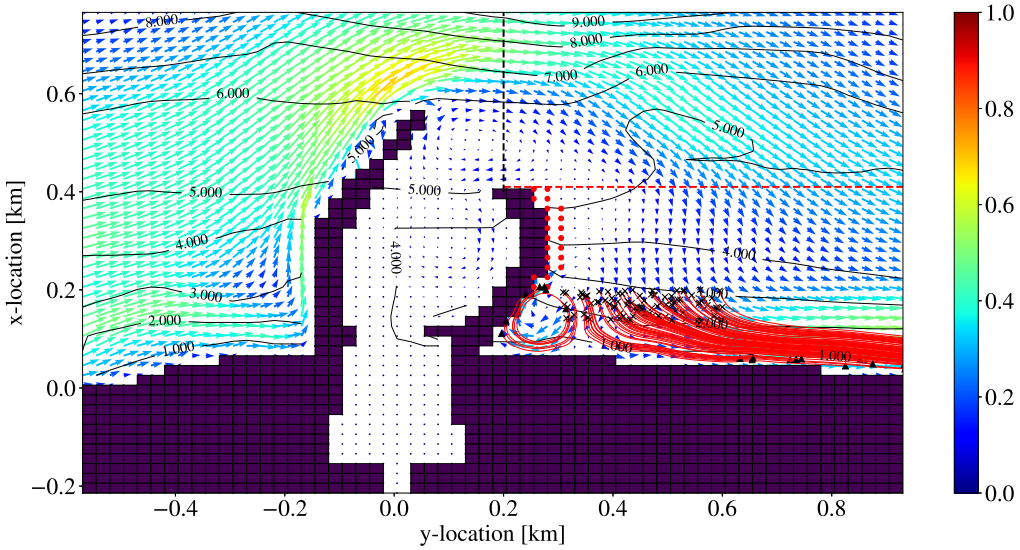

Figure 5.6: Extent of a shadow rip. Drifter trajectories shown in red, drifter begin locations with black crosses and end locations with black triangles. The flow field depicted flow field is a snapshot from the moment of drifter release, with the colors indicating drifter velocities.

Influence of the wave height on the rip velocity are clearest for the waves coming in from northern directions. Waves from these directions show increasing rip velocities for per increased wave height (fig. 5.7, bottom panel). For larger wave heights (H_s =3, 4m) the differences in flow velocities are relatively small. This is likely due to the extent of the surf zone, which already envelopes the northern mole during conditions with H_s =3m. The additional flow generated by H_s=4m is stronger due to the increased wave height, but since this additional flow at least partially bypasses the northern mole the impact on the rip velocity is limited. Northern waves also generally show larger rip velocities. This however also has to do with the limited offshore extent of the shadow rips.
Waves coming in from shore normal show rip velocities which are less dependent on the significant wave height H_s. This is likely due to main driver of the longshore current being longshore differences in wave breaking.
Overall, flow velocities from the directions southern and shore normal directions show rip velocities below 0.2 m/s for all wave heights, meaning that waves from these directions alone produce boundary rips although they are not produce a boundary rip.

Mean drifter velocities for waves coming in from the south show velocities increasing with wave height, with waves from 2m and higher showing velocities of 0.3 m/s and higher. Compared to the maximum velocities found near the harbour mole for the larger wave heights it seems that the extreme drifter velocities do not correspond to drifters inside a shadow rip. Most likely the higher flow velocities are due to the waves being caught in the alongshore current. The longshore current is is able to build up speed from the harbour area to the north without hindrance.

Waves coming in from the northern directions show fairly consistently increasing flow velocities with wave height. Flow velocities near the harbour mole seem to show a strong correlation with the wave height, with larger wave heights resulting in stronger currents.
Differences in flow velocities between these angles of incidence are relatively small, but for the larger wave heights, i.e. $H_s \geq$ 3.0m it is clear that the larger the angle with respect to shore normal, the larger the drifter velocities (fig. 5.7, bottom panel).
Figure 5.7 shows significant differences in flow velocities depending on the wave direction. It is clear that rip currents from waves occur only in the model for wave directions of 30 degrees relative to shore normal and higher for $H_s \geq$ 2.0m.

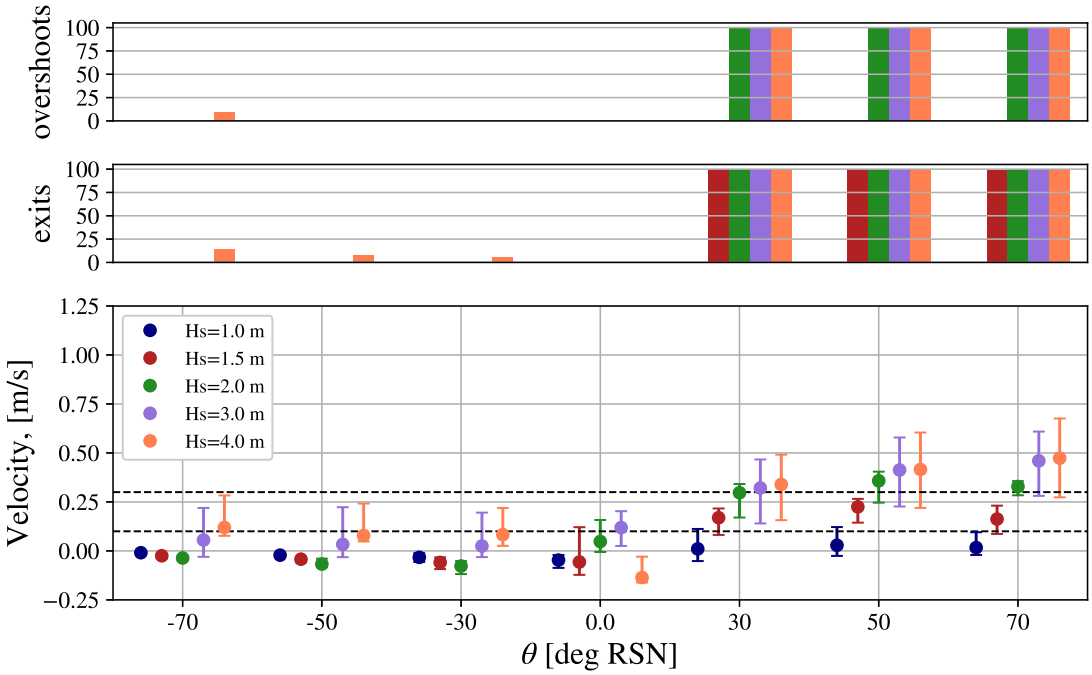

Figure 5.7: Velocities along the northern harbour mole for waves from -70 to 70 degrees RSN and significant wave heights of 1-4 m, combined with overshoots and exits. Top panel: overshoots. Middle panel: exits. Lower panel: flow velocities along the mole; including the median value (dots) and minimum and maximum values.

Waves from the northern direction also cause the most exits and overshoots. Exits occur for wave heights of 1.5m and larger, whereas overshoots occur for wave heights of 2.0m and larger. The waves force the longshore current against the harbour mole, which then deflects the current offshore in the form of a deflection rip. If exits or overshoots take place it was found that all drifters follow this behaviour. For waves larger than 1.5m exits all turn into overshoots. An example is shown in fig. 5.8, which shows drifter trajectories for waves of 2m and a direction of 70 deg RSN.
Looking at the drifter trajectories for waves of 1.5m wave height from the same direction show only exit rates. The flow field however suggests that this is only due to the flow velocity not being high enough to force the drifters south of the northern mole. This is shown in fig. 5.9
Mean drifter velocities for waves from the northern directions increase with increasing wave height and increasing angle relative to shore normal. Mean drifter velocities are only found for wave heights of 3.0m and higher.

During forcing from only waves the angle of incidence regulates which form of boundary rip occurs. As found in literature waves from the southern side of the mole result in shadow rips, whereas waves coming in from the northern side result in deflection rips. The higher wave heights (3 and 4m) indicate that rip velocities are highest for the deflection type. For lower wave heights this can not be said with certainty due to the measured locations adjacent to the mole not being in the range of the shadow rips. Still, literature and higher wave heights suggest that rip velocities are less intense than during deflection rips.

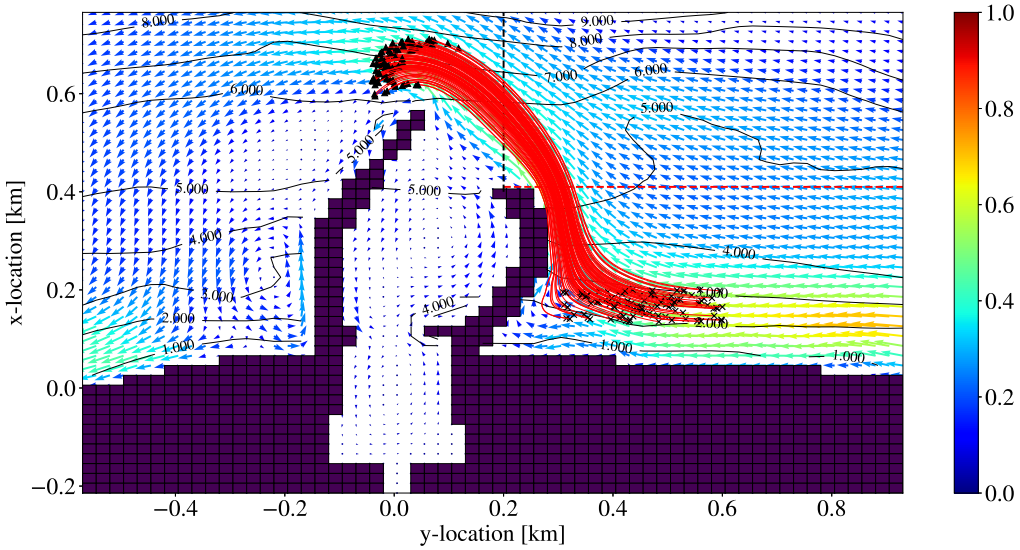

Figure 5.8: Drifter trajectories for waves coming from 70 deg RSN and 2m significant wave height. Trajectories are shown with red lines, drifter start positions are shown with black crosses and end positions with black triangles. Flow field obtained from the moment drifters are released.

5.3.3 Wind

Virtual drifters during wind conditions have been applied to wind forcing of 1.5, 3.0, 4.5, 6.0 and 9.0 m/s for wind directions of -70, -50, -30, 0, 30, 50 and 70 degrees with respect to normal. The combinations are tabulated in table 5.3

Angle of incidence, θ [deg RSN]	Wind speed, W [m/s]
70	1.5, 3.0, 4.5, 6.0, 9.0
50	1.5, 3.0, 4.5, 6.0, 9.0
30	1.5, 3.0, 4.5, 6.0, 9.0
0	1.5, 3.0, 4.5, 6.0, 9.0
-30	1.5, 3.0, 4.5, 6.0, 9.0
-50	1.5, 3.0, 4.5, 6.0, 9.0
-70	1.5, 3.0, 4.5, 6.0, 9.0

Table 5.3: Modeled runs with only wind. Each angle of incidence is modeled separately with each wind speed.

From these forcing only drifters from the latter three directions with wind speeds of $u_{wind} \geq 3.0$ m/s reach the vicinity of the mole as can be deduced from fig. 5.10, which shows the average drifter velocities in the measurement area adjacent to the mole.
As found in literature the more shore parallel the wind direction, the stronger the flow velocities. This also translates in more exits and overshoots.

Winds originating from the southern directions almost have no impact on the flow velocity at the harbour mole. They do however result in longshore flows forcing the drifters northward. Northern winds have a developed longshore flow, which results in overall higher drifter velocities.

Although the modelled winds do not result in any rip currents with velocities of 0.3 m/s or higher, some lead to weaker rips with exits and overshoots. Exits mainly occur during winds of 9.0 m/s, with results showing that exit rates intensify for during more shore parallel winds. The only wind case with exit rates for flow

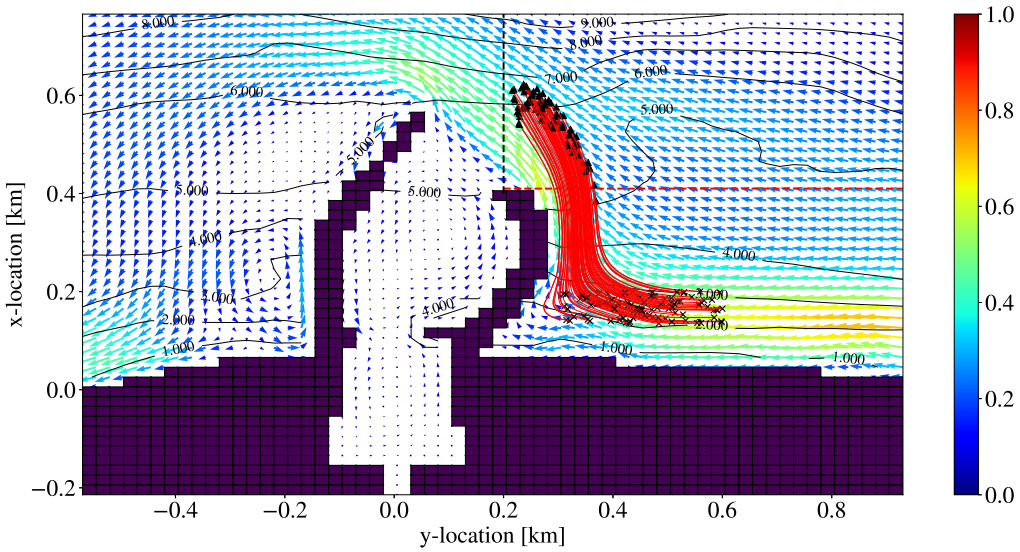

Figure 5.9: Drifter trajectories for waves coming from 70 deg RSN and 1.5m significant wave height. Trajectories are shown with red lines, drifter start positions are shown with black crosses and end positions with black triangles. Flow field obtained from the moment drifters are released.

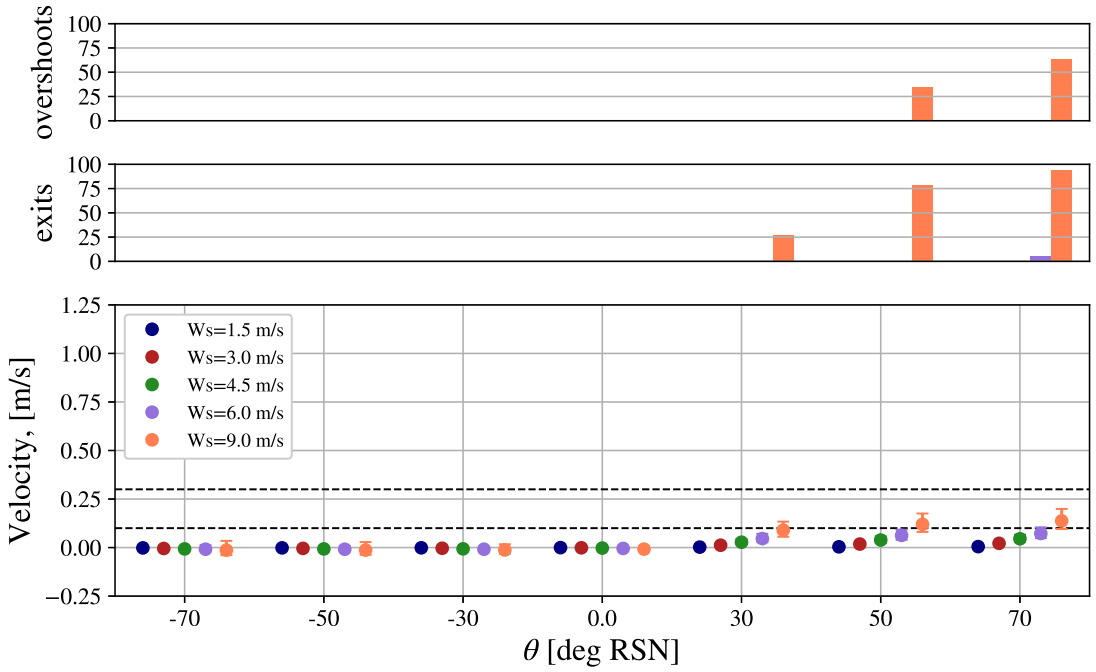

Figure 5.10: Velocities along the northern harbour mole for waves from -70 to 70 degrees RSN and significant wave heights of 1-4 m, combined with overshoots and exits. Top panel: overshoots. Middle panel: exits. Lower panel: flow velocities along the mole; including the median value (dots) and minimum and maximum values.

velocities lower than 6 m/s occurs when the wind direction is 70 degrees to shore normal. Still, for this case exit rates are only 5 out of 100 drifters.

5.4 Multiple Forcing Mechanisms

In this section combinations of tide, wave and wind are analysed. Wind and wave directions are chosen to be the same and fixed combinations of wind speed and wave height will be used. These cases are shown in table 5.4, and will be applied per tide and tidal phase.

Combination	Wind speed, u_{wind} [m/s]	Significant wave height, H_s [m]	Angles, θ [deg RSN]
1	1.5	1.0	-70, -50, -30, 0, 30, 50, 70
2	3.0	1.5	-70, -50, -30, 0, 30, 50, 70
3	4.5	2.0	-70, -50, -30, 0, 30, 50, 70
4	6.0	3.0	-70, -50, -30, 0, 30, 50, 70
5	9.0	4.0	-70, -50, -30, 0, 30, 50, 70

Table 5.4: Combinations of wind and waves for multiple forcing mechanisms

All figures with exit histograms, overshoot histograms, drifter velocities and retention rates can be found in the appendices per tide.

5.4.1 Regular Tide

Outcomes for runs with a tide in between neap and spring show that in all cases rip exits with $u_{drifter} \geq$0.3 m/s occur during wind and wave directions of 50 and 70 deg RSN during forcing combinations 4 and 5 as described in table 5.4. Comparing the outcomes of the individual run of the regular tide with the outcome of the combined forcing indicates that tidal forcing is not dominant in forcing the drifters. Exits mainly occur from high water level to mean water level when the system is forced by only a regular tide (fig. 5.4). Results in combination with wind and waves show however that exits occur for every assessed moment in the tide.
One tidal phase that stands out is during high water. This is the moment in the tide that the least amount of exits become overshoots. The drifter trajectories of this case are shown in fig. 5.11, which also includes the flow field at the moment of drifter departure. From this moment on the tide is moving towards mean water level, which means that the tidal current is weakening. This is reflected by the movement of the drifters, which is mainly directed offshore.
Something similar to fig. 5.11 occurs during two hours before high water level and two hours after low water. At this point in time the tidal current is stronger and the vortex close to the northern mole is still developing, forcing a lot of drifters offshore. The trajectories show a large deflection in the northern alongshore direction once they reach the tip of the harbour mole. This is caused by the considerable longshore tidal current. Still some drifters are driven into the overshoot area. These drifters are the ones floating closest to the mole. That these drifters become overshoots may either be due to their distance from the tidal eddy, due to the large scale turbulent structures in the harbour entrance or a combination thereof. Drifter trajectories during two hours before high water are shown in fig. 5.12. An overview of rip velocities, exits and overshoots during this period is given in fig. 5.13.

During the other tidal phases the longshore current drives the drifters past the northern mole for wave heights larger than 1.0m. The vortex is in these cases too weak or already shed too far from the mole, therefore unable to significantly change the course of the drifters. Alternatively the current generated by wind and waves are equally strong as the tide generated current, thereby forcing the drifters offshore at the location where these currents meet.
Another important thing to note is that during low levels the surf zone has moved seaward with respect to mean water level, as well as the tidal current moving in southward direction. During such times the flow hits the upper part of the mole, which due to its convex shape allows the flow to pass with relative ease. Therefore it seems that overshoots should occur more often during low water levels. This effect is strongest during two hours before low water. At this point in the tide the water has already dropped below mean water level and the ebb tidal current is strongest. An overview of rip velocities, overshoots and exits during two hours before low water is found in fig. 5.14. During mean water level and to two hours after high water the

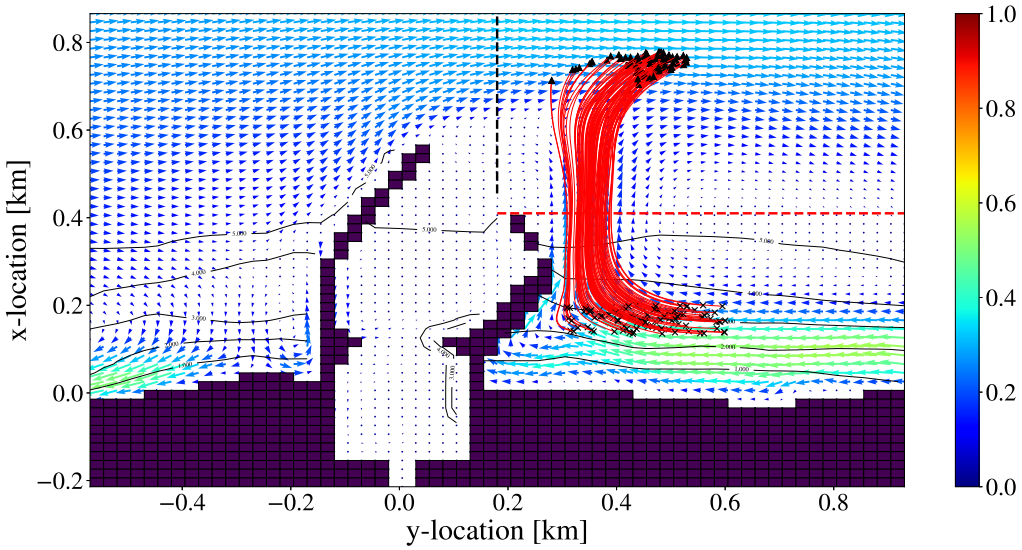

Figure 5.11: Drifter trajectories for wind and waves coming from 50 deg RSN, with 2m significant wave height and wind speed of 4.5 m/s during regular tide and high water. Trajectories are shown with red lines, drifter start positions are shown with black crosses and end positions with black triangles. Flow field obtained from the moment drifters are released.

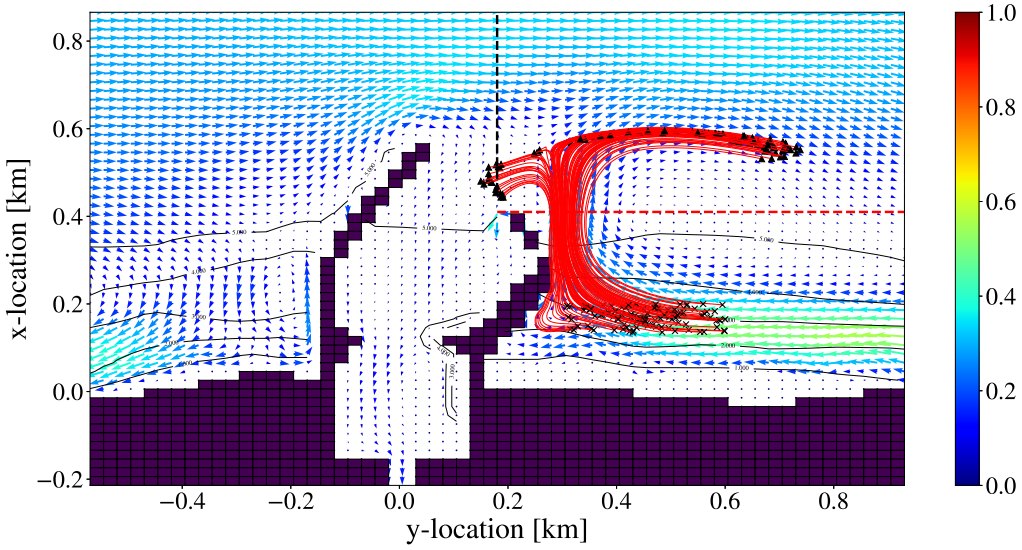

Figure 5.12: Drifter trajectories for wind and waves coming from 50 deg RSN, with 2m significant wave height and wind speed of 4.5 m/s during regular tide and two hours before high water. Trajectories are shown with red lines, drifter start positions are shown with black crosses and end positions with black triangles. Flow field obtained from the moment drifters are released.

tidal current is already directed southward, resulting in high exits and overshoots. This therefore indicates that the effect of the tidal current is stronger than the shape of the mole.
Important to note on the overshoots is that not all overshoots pass both harbour moles. In some cases drifters end up inside the harbour. Such an example is during low water for forcing combinations 4 and 5 with angles of 50 and 70 deg RSN. During such conditions the harbour interior contains a large vortex, which pulls in several drifters.
Mean drifter velocities show similar patterns to single wind and wave runs, with increasing drifter velocities per increased wind speed and wave height. Also the northward directed wind and waves generate higher drifter velocities, similar to the behaviour found during runs forced by waves only.

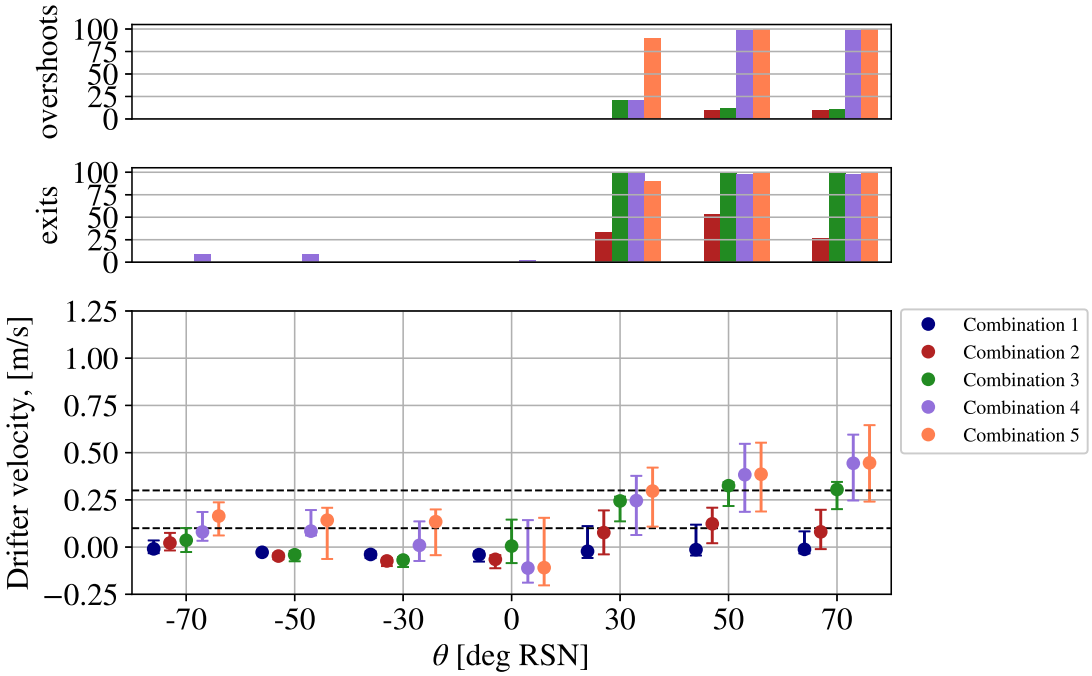

Figure 5.13: Rip velocities along the northern harbour mole combined with overshoots and exits at two hours before high water during a regular tide. Wind and waves combined as shown in table 5.4. Top panel: overshoots. Middle panel: exits. Lower panel: flow velocities along the mole; including the median value (dots) and minimum and maximum values.

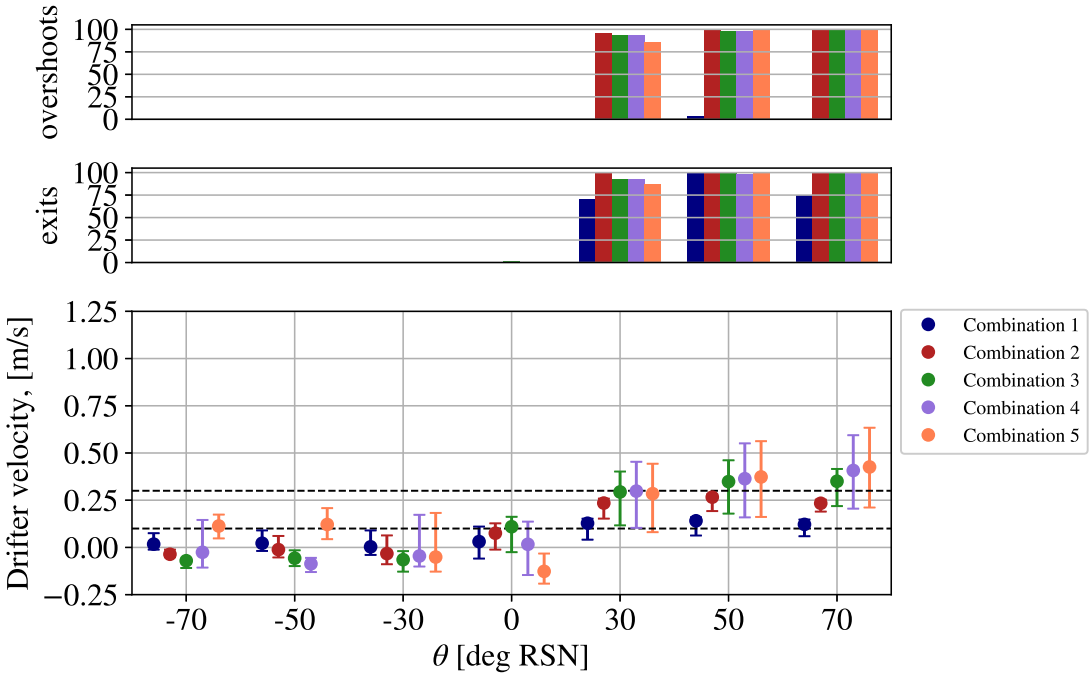

Figure 5.14: Rip velocities along the northern harbour mole combined with overshoots and exits at two hours before low water during a regular tide. Wind and waves combined as shown in table 5.4. Top panel: overshoots. Middle panel: exits. Lower panel: flow velocities along the mole; including the median value (dots) and minimum and maximum values.

5.4.2 Spring Tide

Similar to the regular tide spring tide shows exits rates for all moments in time during forcing combinations 4 and 5 coming from 50 and 70 deg RSN. The main difference between these two tides however is that in general exit rates are lower, with some exceptions. During the exceptions the tidal flow velocity is negative, which amplifies the longshore current and consequently enhances drifter exits and overshoots.
The effect of the surf zone location on the deflection of longshore flow is increased by the larger extremes of the spring tide. As tidal flow velocities are also larger during spring tide there are several phases at which the combined longshore flow creates a large eddy in the harbour interior. This vortex then deflects drifters that travel past the harbour entrance into the interior. In addition to flow reinforcement the location at which the longshore flow collides with the harbour mole also plays a role. As seen during regular tides this location is an important factor in steering the flow. During low water in a neap tide the surf zone is moved even further offshore, allowing for the flow to bypass the harbour area easier. Figure 5.15 shows an example of such a bypass flow occurring during low water.

Mean drifter velocities show a clear relation with the increased wind and wave forcing when from 50 and 70 deg RSN. More intense forcing conditions from these directions lead to higher drifter velocities. Forcing conditions from 30 deg RSN show comparable behaviour to that during regular tide, with drifter velocities sometimes decreasing during forcing conditions 4 and 5.
Mean drifter velocities also tend to be higher during higher water levels for forcing from the north. In the period from two hours before high water to mean water level drifter velocities are higher than drifter velocities during two hours before low water to two hours after low water. For forcing from the south it is the other way around, with drifter velocities often being higher during low water.
This is likely to be due to the whether the tidal flow enhances the longshore flow velocity or not.

Exits occur during spring tides during every tidal phase. It is striking however that during water levels

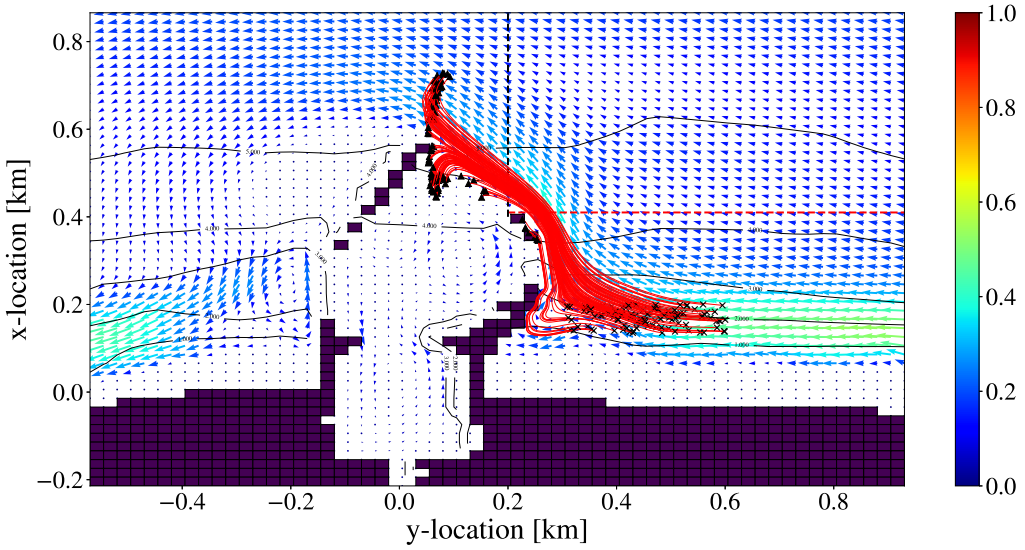

Figure 5.15: Drifter trajectories for wind and waves coming from 50 deg RSN, with 2m significant wave height and wind speed of 4.5 m/s during spring tide and low water. Trajectories are shown with red lines, drifter start positions are shown with black crosses and end positions with black triangles. Flow field obtained from the moment drifters are released.

higher than mean water level exits occur for forcing from -70 to 0 deg RSN. This is strongest seen during high water and high water plus 2 hours and forcing combinations 2 and 3, which are intermediate conditions. Such behaviour is similar to that of the shadow rip, which originates from the shadowing effect of a structure inside the surf zone. Figure 5.16 and fig. 5.17 suggest that for forcing from the southern directions the exit rates increase with increasing obliqueness of wind and waves.
Overshoots also occur during these forcing situations, but less frequently. Also the relation with obliqueness as seen for the exits seems less strong and only is clear during two hours after high water (fig. 5.17).
The relation with the rip velocity found adjacent to the mole forcing intensity is most clear for forcing from 30 to 70 deg RSN, whereas the range of -70 to 0 deg RSN indicates a very weak or no relation. This is most likely due to locations at which the rip velocities are observed, as the shadow rip types occurring during 0 to 70 deg RSN forcing have a very limited extent, meaning that the measurement area oftentimes do not coincide with parts of these rips.

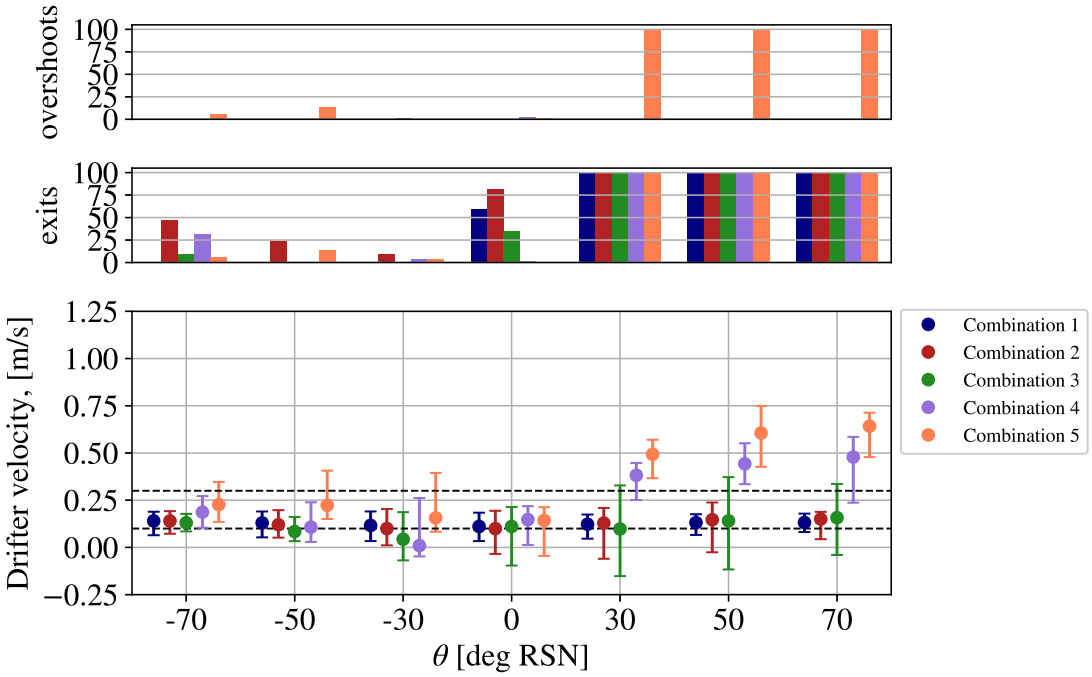

Figure 5.16: Rip velocities along the northern harbour mole combined with overshoots and exits at high water during a spring tide. Wind and waves combined as shown in table 5.4. Top panel: overshoots. Middle panel: exits. Lower panel: flow velocities along the mole; including the median value (dots) and minimum and maximum values.

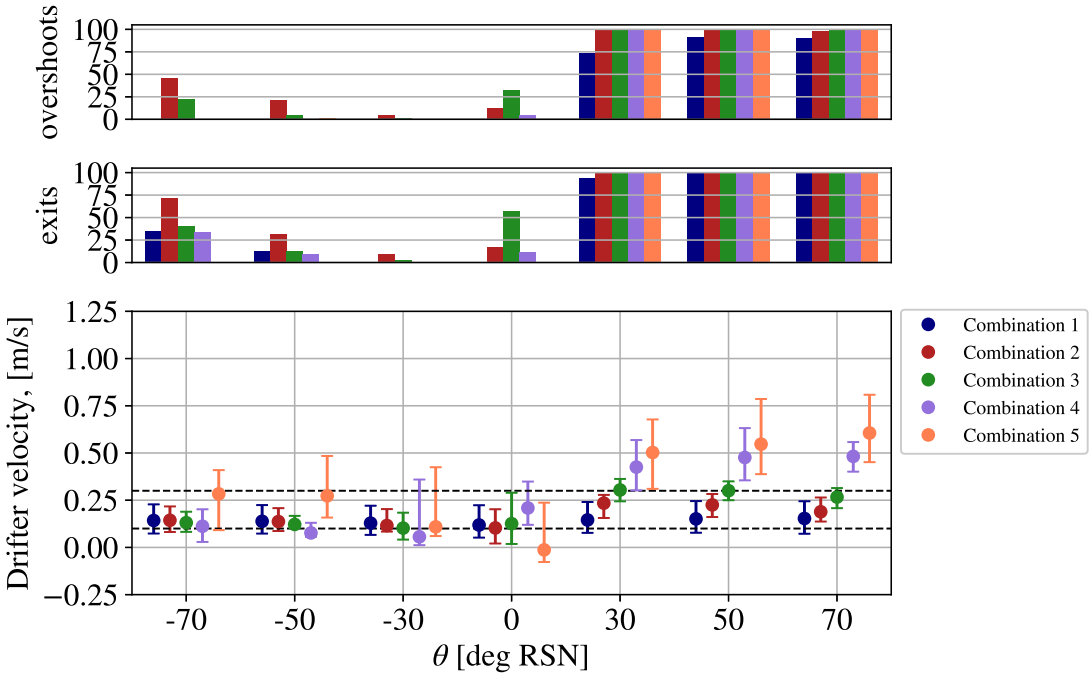

Figure 5.17: Rip velocities along the northern harbour mole combined with overshoots and exits at two hours after high water during a spring tide. Wind and waves combined as shown in table 5.4. Top panel: overshoots. Middle panel: exits. Lower panel: flow velocities along the mole; including the median value (dots) and minimum and maximum values.

5.4.3 Neap tide

Similar to the other tides, exit rates during neap tide occur during all tidal phases for cases 4 and 5 with angles of incidence of 50 and 70 deg RSN. Forcing from this direction results in more exits and overshoots during a regular tide, except during two hours before high water. This is due tidal current which is directed northward and can be seen in fig. 5.18

During high water however also exits occur for forcing from -70 to 0 deg RSN, mainly during forcing combination 5 (fig. 5.19). This is different from the findings during spring tide, which showed more exits during intermediate conditions.

Drifter trajectories during neap tide are fairly similar to the trajectories found during a regular tide. This also goes for the exits and overshoots that were found.

Drifter velocities show the same patterns as during regular and spring tides, with increased drifter velocities for forcing from 50 and 70 deg RSN as the forcing increases. Also drifter velocities are generally higher during higher water levels for forcing from the north. When the forcing originates from the south drifter velocities are generally lower.

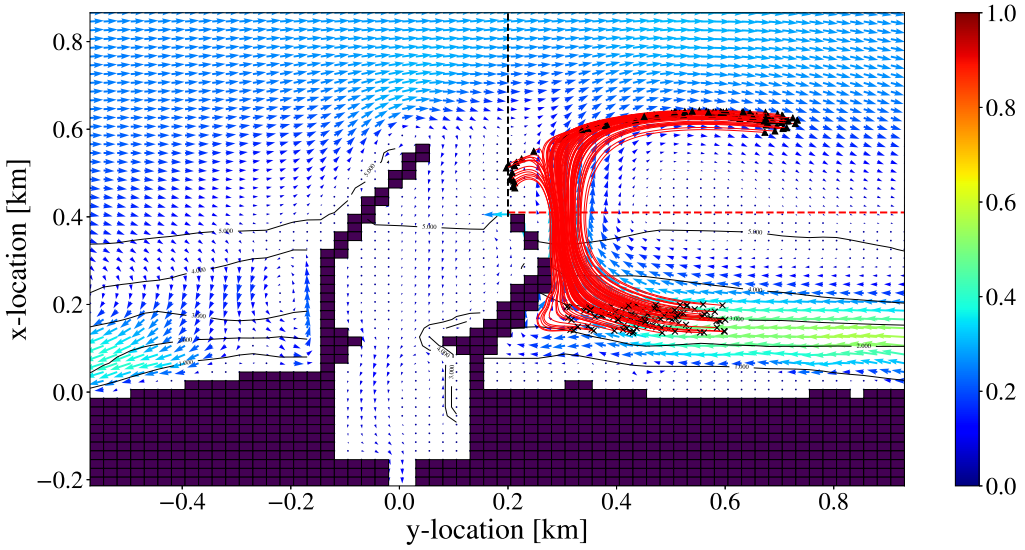

Figure 5.18: Drifter trajectories for wind and waves coming from 50 deg RSN, with 2m significant wave height and wind speed of 4.5 m/s during neap tide and two hours before high water. Trajectories are shown with red lines, drifter start positions are shown with black crosses and end positions with black triangles. Flow field obtained from the moment drifters are released.

5.4.4 Comparison of Superimposed Individual Runs with Combined Runs

Comparison of the individual forcing mechanisms and the combined forcing mechanisms is performed by comparing the rip velocities adjacent to the northern harbour mole. To this the regular tide was chosen, wind from 50 deg RSN and a velocity of 4.5 m/s, and waves from 50 deg RSN with a significant wave height of 2.0 m. In short this comes down to a regular tide with forcing combination 3 from table 5.4 with an angle of 50 deg RSN.

Due to forcing by only waves the range of velocities at the mole lies between 0.25 and 0.4 m/s and for wind only between 0.03 and 0.07 m/s. Rip velocities for only tidal forcing differ per tidal phase, with the highest overall velocities found during high water and the overall lowest velocities during two hours after low water. Comparing the superimposed rip velocities immediately show that, when compared to the full model, the variant with tide + wind shows the least resemblance to the combined model. The best fit seems to be the superposition of tide + waves from two hours before low water until two hours after low water. From two hours before high water level until mean water level the differences are relatively large, where the superimposed tide and waves show approximately two times higher velocities than the combined model. Overall the superposition of tide and waves gives an overestimate of the full model. Figure 5.20 shows the velocities of each single forcing mechanism, the full model and the following combinations: tide + waves, tide + wind and tide + waves + wind.

The superposition of tide, wind and waves gives a larger overestimate of the full model when compared to the superposition of waves and tide. Differences between the superimposed combinations and the full model during high water level are likely to be due to the aforementioned fact that wind, waves and tide are not linear processes, meaning that the interaction between component is not a simple subtraction or addition. Also, the tidal water level together with the wave height determine the extent of the surf zone. In the superimposed combinations the rip induced by the wind and waves is directed at the some stretch of the mole, with only the superimposed tide inducing a variable current in time. In the full model the stretch which is hit by the current differs due to the relocation of the surf zone by the tidal water level. Results from the regular tide with a wind of 4.5 m/s and waves of 2.0m from 50 deg RSN show higher overall rip velocities during lower water levels. Figure 5.13 and fig. 5.14 indicate this relation. For the results of all moments in the regular tide the reader is referred to appendix B.

Additionally, the boundary rip is mainly a product of the longshore current generated by wind, waves and

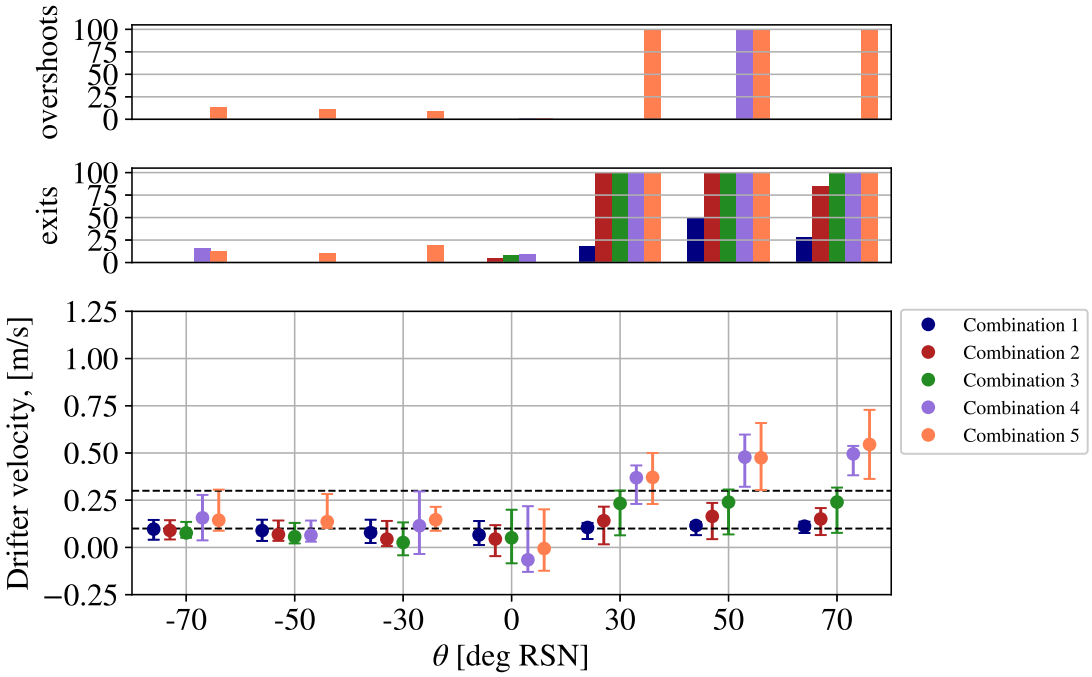

Figure 5.19: Rip velocities along the northern harbour mole combined with overshoots and exits at high water during a neap tide. Wind and waves combined as shown in table 5.4. Top panel: overshoots. Middle panel: exits. Lower panel: flow velocities along the mole; including the median value (dots) and minimum and maximum values.

tide. During the higher water levels the tidal current is directed against the current induced by waves and wind. As a result, the longshore current is lower and therefore the rip velocities observed in the full model are also lower. This reduced longshore flow is not accounted for when single components are added together, as this only adds the rip velocities adjacent to the harbour mole.

It was found that the individual wind forcing lies between $\frac{1}{10}$ and $\frac{1}{5}$ of the wave forcing (fig. 5.20). The differences in rip velocity between tide and tide + wind, and tide + waves and tide + wind + waves shows that the impact of wind is only minor. Looking at the differences between tide only and tide + waves, the waves have a severe impact on the flow regime. That this occurs in the model as well is supported by the minor differences in flow velocities between the full model and the combination of tide + waves.

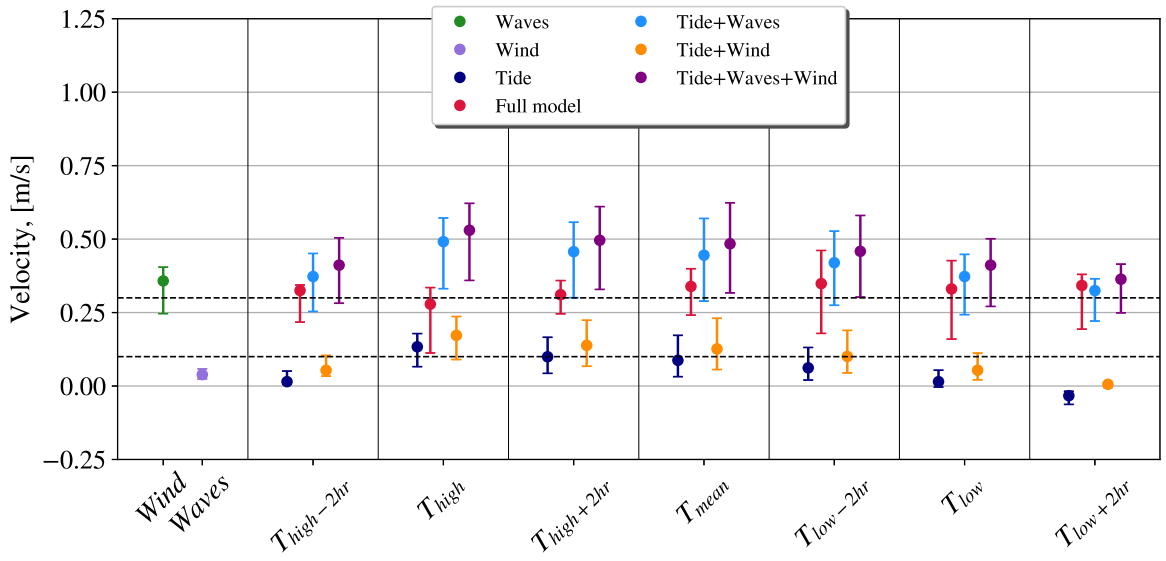

Figure 5.20: Comparison between the individual forcing components, three superimposed variants, and the combined model. The chosen tide is regular, waves from 50 deg RSN with H_s=2.0 m and wind from 50 deg RSN with 4.5 m/s. The black dotted lines represent the 0.1 m/s and 0.3 m/s thresholds.

5.4.5 May 11th 2020

The Delft3D model and virtual drifters have been applied to conditions similar to the accident which occurred May 11th 2020. A significant wave height of H_s=3.0 m has been applied with a peak period of T=8.0 seconds from 335 degN, which is the same as 25 deg RSN. A directional spreading of 8 has been applied to these waves. Wind is modeled as uniform over the whole area with a wind speed of 11 m/s and a direction of 10 degN, or 60 deg RSN.
Virtual drifters have been deployed every hour from 15:00 to 20:00, with a deployment time of 60 minutes. Results show very large amounts of exits and overshoots during all times (fig. 5.21a).

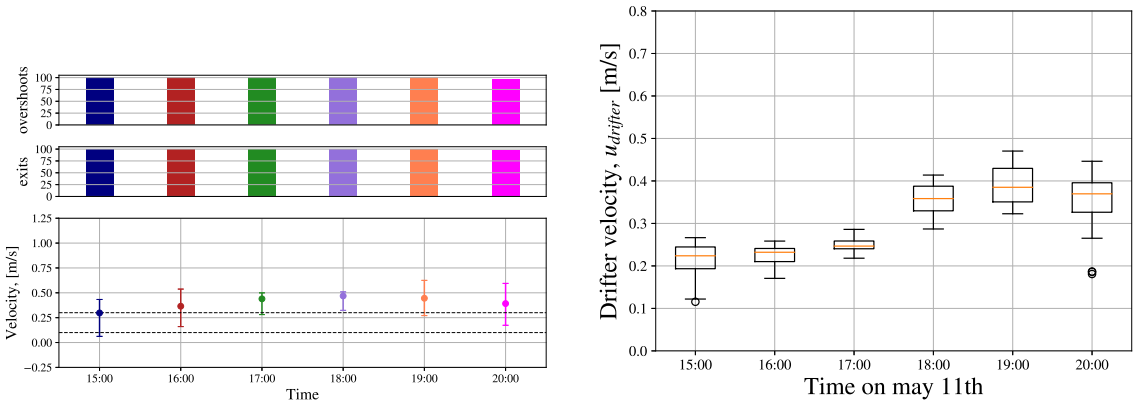

(a) (b)

Figure 5.21: a) Plot showing overshoots (top panel), exits (middle pannel) and velocities adjacent to the northern mole (bottom panel). b) Box plots with mean drifter velocities.

Drifter velocities during this case are relatively high (fig. 5.21b). The wave height used is the same as for

forcing combination 4, but the wind speed is almost double. Forcing conditions are still less severe than a forcing combination 5. Therefore the 11 May case will be considered as in between these two.
The drifter trajectories as shown in fig. 5.22 show the paths traveled per drifter. The locations at which the surfers were found during the accident was in the retention area. Although some drifters are retained the end positions of the drifters after being outside the rip do not coincide with the accident.

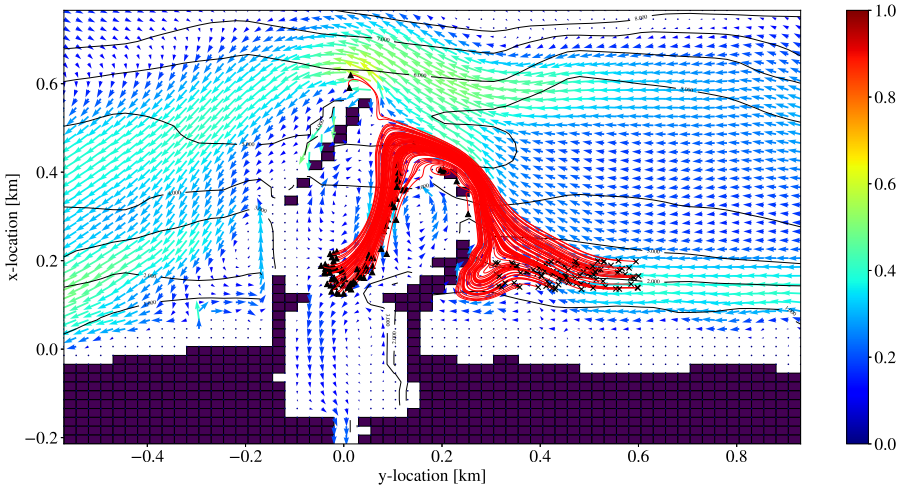

(a)

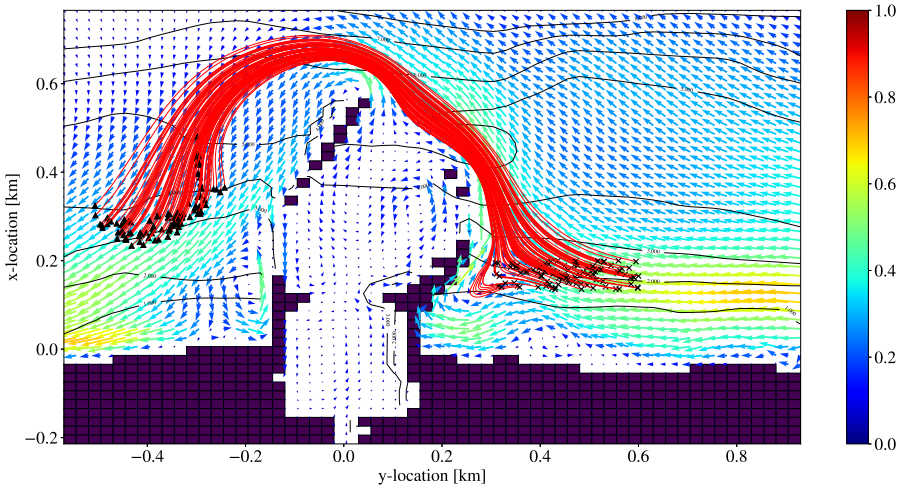

(b)

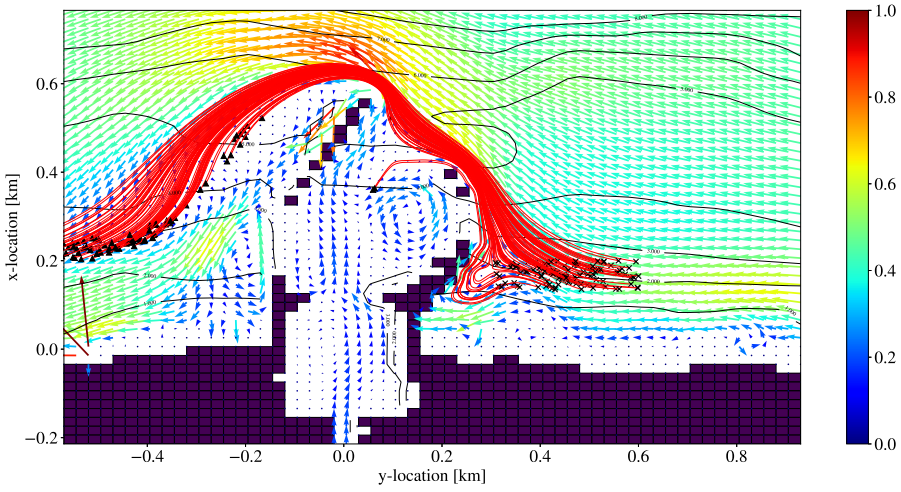

(c)

Figure 5.22: Drifter trajectories in flow field during numerical run May 11$^{\text{th}}$ 2020. Crosses: drifter start, triangles: drifter end. a) T=15:00. b) T=18:00. c) T=20:00.

6. Discussion

The goal of this research is to investigate the behaviour of boundary rips and the involved forcing mechanisms by means of a numerical model in Delft3D. The main findings will be discussed in this chapter including interpretation of the results.

6.1 Forcing by Single Factors

6.1.1 Tide

During runs with only the tide as a forcing mechanism no rip currents with $u \geq 0.3$ m/s were found. If a rip current should occur with $u \geq$0.3 m/s during a tide, it is likely to happen during flood flow this shows the highest drifter velocities and the highest velocities adjacent to the harbour mole.
Ebb flow is generally speaking slower due to the decreased water level, which in turn makes the wave more susceptible to bottom friction and slows it down. Spring flood flows however have a longshore ebb flow of order 0.5 m/s and could therefore be a good candidate for a rip. Also, results in the previous chapter show that when the water level is lower the deflection of the longshore current is less severe, resulting in drifters which pass at least the northern breakwater. Even though flow velocities generally increase in this area due to flow line contraction, bottom friction is likely a dominant process as the area is very shallow. Therefore the tide is unlikely to form a rip by itself, even during a spring tide.

6.1.2 Waves

The applied waves in the model are wind waves. Results show that exit rates with $u_{drifter} \geq$0.3 m/s occur during waves coming in from 50 and 70 deg RSN have exit rates for significant wave heights of $H_s \geq$2.0m, and also some for a significant wave height of 4.0 m during 30 deg RSN. Overshoots occur for the same conditions except for wave heights of 2.0m. The directions of 50 and 70 deg RSN are likely to be dominant because they produce the strongest longshore directed flow in southward direction. Waves from 30 deg RSN also create a longshore current, but due to the angle of incidence this is less effective. The boundaries may here also play a role as waves are applied uniformly over them. However, boundaries have been extended outside of the Delft3D FLOW domain to normalize such errors.
Waves coming in from the southern directions cause a longshore flow which collides with the southern breakwater. As it is longer than the northern breakwater it takes higher waves to effectively get past the harbour area and effectively influence the surf zone in the direct vicinity of the northern mole. Waves with 4m wave height are large enough and even create a longshore current stretching beyond both moles. By passing the harbour area flow lines expand and a turbulent structure follows. This is likely to affect the drifters such that they exit beyond the moles, albeit with a drifter velocity lower than 0.3m/s.
Overshoot rates do not seem to occur for wave heights lower than 3.0 m, whereas exits do occur for waves of 2.0 m. A possible explanation for this is that flow velocities during such waves are too low. This seems an acceptable conclusion as the difference in mean drifter velocities between waves of 2m and waves of 3m height showed differences of 0.1 m/s for 70, 30 and 50 deg RSN.

6.1.3 Wind

Wind forcing as applied in the model does not lead to boundary rip velocities larger than 0.3 m/s. Highest velocities were found during winds of 9.0 m/s from 70 deg RSN. For the directions of 30-70 deg RSN only wind speeds of 9.0 m/s led to exits. One exception is the wind from 70 deg RSN with a wind speed with about 10 exits. Wind generated currents for these winds speeds are simply not strong enough to create a boundary rip. This is likely due to the limited extent that the wind speed influences flow velocities over the whole water column. Only at the surface near wind speeds are obtained, whereas in deeper areas flow velocities rapidly decline. The result is a low depth averaged flow.
The effect of wind on the drifters however is likely to be different from field tests using drifters. Drifters in the model are not affected by windage, whereas real life drifters may stick out of the water or float close to the surface, meaning that the effect on such measurement devices is larger than in the numerical model.

6.2 Forcing by Multiple Factors

6.2.1 Regular, spring and neap tides

All runs with multiple forcing factors show a general decrease in exits and overshoots during two hours before high water and high water. This coincides with the formation and growth of the tidal eddy and strong northward flood flows. Interesting enough this is also the moment at which the tidal flow reinforces the longshore flow velocities from wind and waves from the directions of -70 - -30 deg RSN. Mean drifter velocities in the measurement area during the low water period and waves from 30-70 deg RSN are generally also lower than during high water. This may be due to the increased bed shear and the fact. When the water level is low, the surf zone lies further seaward than during high water. The location at which the current then hits the breakwater is also at the more seaward end, which in the model has a convex shape. This convex shape allows the longshore flow to pass relatively easily. In case of high water the surf zone and longshore current move more landward. This means that the longshore current will also hit the mole at the more landward end. At this end the breakwater shape forces the incoming current such that it is directed partially against itself. This leads to both a more net offshore directed flow and an increase in flow lines, which accelerates the flow. Therefore the result is a stronger rip current.
Additionally, the amount of overshoots that will occur are dependent on the width of the surf zone, which steers the rip current into southward direction if it is wide enough. The surf zone only extends beyond the harbour area for waves with $H_s \geq 3$m, which coincides with forcing case 4. This forcing case is the lowest forcing case for which overshoots take place during T_{high}-2, T_{high} and T_{high}+2.
There are some differences in exits and overshoots between the different tides. During spring tide it was found that during low water exit and overshoot rates are higher than during a regular tide. This is likely to be due to the increased flow velocities resulting from the larger tidal flow velocities. Additionally, because the water level has larger extremes, the surf zone is located much further offshore, making it easier for drifters to escape past the moles as they have to deflect less far.
Neap tide seems to have the least favorable for exit and overshoot rates due to the combination of its low extremes. Here flow velocities due to the tide are low and during low water the surf zone lies more landward compared to the other two tides. This should make it harder for drifters to exit the retention area.

6.2.2 Superposition of Single Factors versus Multiple Factors

Results showed that the full model is best estimated by the superposition of the wave and tidal components during the period from two hours before low water until two hours after low water. It is likely that the effect of wind, waves and tide on each other account at least partially for the differences between the combinations and the full model. Especially during high water the tidal longshore current is directed against the wind and waves coming from 50 deg RSN. This means that the longshore current directed towards the harbour mole by wind and waves is weakened by the opposite directed tidal current. This effect cannot be accounted for by superimposing all individual components.
Additionally the location of the surf zone and its effect on the rip velocity are not reflected by summing up the single factors. It is likely that this at least has some effect on the current, especially since the shape of

the mole is convex. This means that during high water the longshore current is partially deflected back in longshore direction, whereas during low water it is guided easier along the harbour.

The impact of the wind on the rip velocity was found to be low in comparison with the other factors, although in the superimposed combination of wind + waves + tide it showed quite an overestimate when compared with the full model. Similar to the combination with waves + tide the difference with the full model during higher water levels can be explained by the opposite directions of the tide and the combined flow of wind and waves. During low water it is less clear what may cause the large difference, but may simply be an effect of the aforementioned non linear interactions between the three components that form the current.

Combinations of wind speed and wave height were made on the basis of individual occurrence instead of the co-occurrence of wind speed and wave height. This is likely to have caused the wind-wave combinations to have somewhat low wind speeds in comparison with the co-occurring wave height. Still, the highest attained overall rip velocities occurred during winds of 9.0 m/s from an angle of 70 deg RSN, with current velocities between 0.1 and 0.2 m/s. If these were to occur with waves lower than 4.0m, and instead with for example a significant wave height of 2.5-3.0m, the wave forcing would still likely to be dominant on the basis of velocities found in fig. 5.7.

6.2.3 May 11th

The results from the run for May 11th are quite different from what happened during the accident. Surfers were found in the area adjacent to the northern mole, whereas the virtual drifters exited the area. A possible cause is the simplification of the conditions in the model. For example, an astronomic tide has been applied at the boundaries instead of a time series of the water level. Additionally the wind turned on that day, which has not been incorporated in the model. The model has instead been run with the wind direction which occurred during the accident.
An additional difference between the model and reality is the duration of a virtual drifter run and the time that the victims were suspended in the water. Virtual drifters were only deployed for one hour, whereas the victims were found hours after the accident occurred. If the virtual drifters had been deployed for longer than one hour several drifters are likely to have re-entered the surf zone due to the turning of the tide.
Another cause for the differences is that the virtual drifters do not get stuck inside the harbour moles due to the space interpolation used.
Lastly, the surfers were also hindered by sea foam which collected near the harbour mole. This impeded their view and orientation, and made it harder to get away from the dangerous situation. Especially combined with the strong windage they may not have been able to get past the mole. The effect of the foam and windage were also not taken accounted for in the model. It would have been hard to account for the effect of sea foam in the model, but adding windage to the drifter behaviour might have significantly altered the drifters behaviour, making it more surfer like in its reaction to wind forcing.

6.2.4 Swimmer Safety

From literature it was found that rips with velocities of 0.3 m/s and higher are found to be potentially dangerous for swimmers. This however strongly depends on several things, such as the swimming ability, health, age, gender, but also the conditions such as amount and height of incoming waves, wind speed and many more parameters.
The velocity threshold is therefore limited in its use, because it does not account for the rest of the circumstances.

Results also showed that mean drifter velocities for waves from the south could well exceed 0.3 m/s from only being in a longshore current. This shows that swimmer safety is not only relevant near structures where boundary rips can occur, but also at locations where it would be less expected.

6.3 Measurement Methodology

Rip currents have measured using virtual drifters during post processing of the Delft3D velocity field outputs. Some problems with post processing lie in the domain in which to measure the rip currents. For this case the measurement area was chosen to be between 0.23km$< y <$0.38km and 0.255km$< x <$0.305km. This is seems like a narrow strip but in reality rip currents are much narrower than 50m, more in the order of 10m or less. Increasing the width of the measurement area resulted in lower rip velocities, whereas narrowing it down resulted in higher rip current velocities, as these are calculated as the mean drifter velocity inside the measurement area. It is possible that rip velocities are actually higher than found in this study, as the width of a cell in longshore direction is 25m. This is about three to four times the width of a rip current.

Another sensitivity found during post processing was the sensitivity of the drifter behaviour to the velocity criterion, i.e. when a person stops and starts being inside a dangerous rip. A difference of 0.05 m/s can mean a difference of 10 or more drifters. It is therefore important to define the criteria which form a rip very well.

7. Conclusion

In this research the influence of wind, wind waves and tide have been investigated on the formation of rip currents in the Scheveningen harbour area. The research question posed for this problem is:

What combinations of wind-waves, tide and wind lead to offshore boundary rip transport and what combinations lead to retentive boundary rip transport at the Scheveningen harbour moles?

Analyzing of the system has been done by means of numerical modeling in the Delft3D program. First wind, wind waves and tide have been analyzed separately, after which the full system has been analyzed.
The obtained flow fields were then used for virtual drifters. These drifters provided trajectories and velocities of particles caught in the stream. The end positions of the drifters were then categorized as retention, exit or overshoot. This would then also be the transport pattern linked to the forcing conditions.

Results from the individual forcing mechanisms show that only waves with a significant wave height of 2m and higher for the directions of 50 and 70 deg relative to shore normal result in rip currents with a velocity of at least 0.3 m/s. Although spring tide has velocities of order 0.5 m/s it does result in the development of a rip. Wind speeds of 9 m/s are also not enough to create a rip with velocities of 0.3 m/s. They do however drive rip currents, but these are weaker than the ones assumed to be potentially hazardous.

Combining wind, wave and tide did lead to rip current of $\geq$0.3 m/s. These occur with forcing from 30-70 deg relative to shore normal and with wind speeds of 4.5 m/s and higher and wave heights of 2.0m and larger. Most exit rates are generated by forcing from 50 and 70 deg relative to shore normal.
When combining the wind, waves and tide separately, with wind speeds of 4.5 m/s from 50 degrees relative to shore normal, a significant wave height of 2m from 50 degrees relative to shore normal and a regular tide and comparing those to a full model run of these conditions it was found that waves and tide have the strongest impact on rip current intensity. Although wind forcing is not negligible, it has a minor impact on the rip intensity as it is estimated to amount to approximately $1/10^{\text{th}}$ of the rip velocity.
It was found that the tidal flow and water level has a an impact on rip behaviour, as well as the convex shape of the breakwater. During high tide the longshore flow collides with the landward end of the breakwater, which directs the flow partially back due to its convex shape. When the flow then passes the harbour mole during high water both the tidal current and the vortex in the lee of the mole force the drifters offshore in northern direction. In case of approximately equal but opposite tidal current and wind-wave induced current, the drifters are forced offshore in a line parallel to the mole. During low tide the longshore flow is only partially deflected offshore. With the observed higher drifter velocities during high tide than during low tide, this indicates the importance of the water level on rip intensity.

A case study was also performed on the accident that occurred on May 11^{th} 2020 near the Scheveningen harbour. The model was not able to reproduce the situation as drifters exited the area, whereas during the accident surfers were found inside the retention area. Although wind forcing was larger than in the other modeled cases, from comparison wind driven currents were only found to be a about ten percent of the wind speed. Additionally, due to the angle of the wind with respect to the coast line the contribution of the wind to the flow velocity also is decreased. Tide and waves were found to be dominant. The tidal motion induces flow which enhances the longshore flow, but also affects the behaviour of the flow with due to the changing

water levels.
As waves have shown to be the only mechanism which can produce potentially hazardous rip currents on its own, this is the most important forcing factor. Although the effect of waves on the rip intensity can also strongly be affected by the tide.
Even though the model did not yield an accurate representation of the accident, it does show the relative importance of wind, wave and tidally generated longshore currents in the formation of boundary rips and its effect on suspended particles, as well as showing the effects of tidal water level and mole shape on steering the suspended particles.
From the model outcomes it follows that wind and waves from the directions of 30-70 deg RSN are most likely to lead to a boundary rip. During such conditions offshore directed rips mainly occur during high water, whereas overshoots are more likely to occur during low water at the Scheveningen harbour area. Comparison with a case study does not confirm these findings, but more validation is necessary as well as incorporation of windage for the virtual drifters, possibly longer virtual drifter run times and an evaluation of when the drifters should stick in the harbour mole.
Retentive behaviour for rips was found to occur mainly during wind-wave forcing from -70 to 0 degrees relative to shore normal.

8. Recommendations

This chapter will present recommendations for further research. These consist of measurements for validation and varying several model features.

- In this study no measurements were performed to validate the model results. Instead the model has been tested on its behaviour and compared with literature. Drifter and ADCP measurements for example would provide useful data to check model outputs against and also calibrate it. Useful scenarios would be a full tide, wind-wave scenarios with selected on basis of which wind speed co-occurs with which significant wave height. The former would ideally be during very calm conditions, meaning as little wind and waves as possible, using a drifter type which is not much affected by windage. The latter should be performed for several wind-wave directions, with the conditions lasting as long as possible. This way a database with field gathered data can be built against which the model results can easily be checked.
  As for drifter run times several options would be possible. One is to release the drifters during preselected moments in the tide for a short amount of time (e.g. an hour), the other option would be to release the drifters for a whole tidal cycle. This depends on the time scale of interest of course, although it will be interesting to be able to compare the long term behaviour of suspended drifters with the short term behaviour.

- Rip currents are often very narrow structures with respect to the surf zone, sometimes with widths of less than 10m. In this study the width of cells is 25m, which is more than 2.5 times the width of a rip current. In order to better capture rips it might be beneficial to decrease the grid cells. Additionally it might be valuable to do some more testing on the numerical model behaviour of the rip current, i.e. how wide it is in the model. This would allow for a more accurate definition and outputs of the velocities within the modelled rip. In this model the rip was chosen to be adjacent to the harbour mole, but some drifter trajectories suggested that it may sometimes be located somewhat further away from the mole or wider than expected.

- The harbour moles were found to be important features in adjusting the tidal flow. For a future model it is useful to check results against straight moles to obtain a better understanding on the total extent of their effect on deflecting longshore flow.

- Tidal behaviour has only been described using one run for each tide. In order to add variability to the results several tides on different dates can be used to check drifter behaviour. This should give a more generalized result of the model behaviour. The same thing can be done during wave and wind runs by releasing the drifters at different times.

- During model validation it became clear that boundary errors are very limited in this model. Therefore it is possible to shorten the longshore extent of the FLOW grid. This should save computational time and would make it more feasible to implement improvements such as the aforementioned grid refinement.

- This study focused on rip velocity as a measure for swimmer hazard, but as discussed in chapter 6 the velocity threshold is not a foolproof measure on rip safety. It would be beneficial to formulate a criterion which incorporates more variables to determine swimmer safety for rips. This criterion could for example include wave height and wave period, as well as the wind velocity and wind direction.

Although according to this study the wind is not of high consequence in the rip flow velocity, swimmers are prone to windage.

References

Black, K. P., & Gay, S. L. (1987). Eddy formation in unsteady flows. *Journal of Geophysical Research*, *92*, 9514-9522.

Bosboom, J., & Stive, M. (2015). *Coastal dynamics i.* Delft, The Netherlands: Delft Academic Press.

Castelle, B., Scott, T., Brander, R., & McCarroll, R. (2016). Rip current types, circulation and hazard. *Earth-Science Reviews*, *163*, 1–21.

Dalrymple, D. (1992). *Facies models response to sea level changes, tidal depositional systems.* Saint John's, Newfoundland en Labrador, Canada: Geological Association of Canada.

Dalrymple, R. A., MacMahan, J. H., Reniers, A. J., & Nelko, V. (2010). Rip currents. *Annual Review of Fluid Mechanics*, *43*, 551–581.

Deltares. (2020). *Delft3d-flow, user manual.* Delft, The Netherlands: Author.

de Schipper, M. A., de Vries, S., Ruessink, G., de Zeeuw, R. C., Rutten, J., van Gelder-Maas, C., & Stive, M. J. (2016). Initial spreading of a mega feeder nourishment: Observations of the sand engine pilot project. *Coastal Engineering*, *111*, 23-38.

Emeis, K.-C., van Beusekom, J., Callies, U., Ebinghaus, R., Kannen, A., Kraus, G., ... Zorita, E. (2015). The north sea — a shelf sea in the anthropocene. *Journal of Marine Systems*, *141*, 18-33.

Holthuijsen, L. H. (2009). *Waves in oceanic and coastal waters.* Cambridge, UK: Cambridge University Press.

https://waterinfo.rws.nl/. (n.d.). *Scheveningen: Waterhoogte astronomisch tij t.o.v. nap.* Retrieved 31-03-2021, from `https://waterinfo.rws.nl/#!/details/publiek/astronomische-getij/Scheveningen(SCHEVNGN)/Waterhoogte___20berekend___20Oppervlaktewater___20t.o.v.___20Normaal___20Amsterdams___20Peil___20in___20cm`

Jackson, D., & Short, A. (2015). *Sandy beach morphodynamics.* Radarweg 29, 1000 AE Amsterdam, The Netherlands: Elsevier.

KNMI. (n.d.). *Windrozen van de nederlandse hoofdstations.* Retrieved 30-03-2021, from `https://www.knmi.nl/nederland-nu/klimatologie/grafieken/maand/windrozen`

Kvale, E. (2009). Tidalites. *AccessScience, [online].* Retrieved 2021-03-29, from `https://www.accessscience.com/content/tidalites/696800`

Longuet-Higgins, M. (1970a). Longshore currents generated by obliquely incident sea waves, 1. *Journal of Geophysical Research*, *33*, 6778–6789.

Longuet-Higgins, M. (1970b). Longshore currents generated by obliquely incident sea waves, 2. *Journal of Geophysical Research*, *33*, 6790–6801.

Longuet-Higgins, M., & Stewart, R. (1964). Radiation stresses in water waves; a physical discussion, with applications. *Deep-Sea Research*, *11*, 529–562.

Meteoblue. (n.d.). *Klimaat scheveningen.* Retrieved 30-03-2021, from `https://www.meteoblue.com/nl/weer/historyclimate/climatemodelled/scheveningen_nederland_2747599`

Mouragues, A., Bonneton, P., Castelle, B., Marieu, V., Barrett, A., Bonneton, N., ... Sous, D. (2020). Field observations of wave-induced headland rips. *Journal of Coastal Research*, *95*, 578–582.

Murray, S. (1974). Trajectories and speeds of wind-driven currents near the coast. *Journal of Physical Oceanography*, *5*, 347–360.

Nummedal, D., & Finley, R. J. (1978). Wind-generated longshore currents. *Coastal Engineering*, *16*, 1428–1438.

Pattiaratchi, C., Olsson, D., Hetzel, Y., & Lowe, R. (2009). Wave-driven circulation patterns in the lee of groynes. *Continental Shelf Research*, *29*, 1961-1974.

Radermacher, M., de Schipper, M., Swinkels, C., MacMahan, J., & Reniers, A. (2017). Tidal flow separation at protruding beach nourishments. *Journal of Geophysical Research*, *122*, 63-79.

Reniers, A., MacMahan, J., Thornton, E., Stanton, T., Henriquez, M., Brown, J., ... Gallagher, E. (2009). Surf zone surface retention on a rip-channeled beach. *Journal of Geophysical Research*, *114*.

Roelvink, D. J., & Walstra, D.-J. (2005, 01). Keeping it simple by using complex models. In (Vol. 6).

Saylor, J. (1966). Currents at little lake harbor. *U.S. Lake Survey*, *1*.

Schlooz, G. (2012). *Convex coastline induced rip currents at the sand engine* (Master's thesis, Technical University Delft, Faculty of Civil Engineering and Geosciences, Department of Hydraulic Engineering, Delft, The Netherlands). Retrieved 01-10-2020, from `http://resolver.tudelft.nl/uuid:a947fb54-f14b-456d-b99c-321ee52a5c75`

Scott, T., Austin, M., Masselink, G., & Russell, P. (2015). Dynamics of rip currents associated with groynes — field measurements, modelling and implications for beach safety. *Coastal Engineering*, *107*, 53–69.

Signell, R., & Geyer, R. (1991). Transient eddy formation around headlands. *Journal of Geophysical Research*, *96*, 2561-2575.

Snedden, J. W., & Nummedal, D. (1990). Coherence of surf zone and shelf current flow on the texas (u.s.a.) coastal margin: implications for interpretation of paleo-current measurements in ancient coastal sequences. *Sedimentary Geology*, *67*, 221–236.

Sous, D., Castelle, B., Mouragues, A., & Bonneton, P. (2020). Field measurements of a high-energy headland deflection rip current: Tidal modulation, very low frequency pulsation and vertical structure. *Journal of Marine Science and Engineering*, *8*(7), 18-33.

Tomczak, M. (1988). Island wakes in deep and shallow water. *Journal of Geophysical Research*, *93*, 5153-5154.

Trouw. (2020, May). Vijf watersporters sterven aan de 'cappuccino coast'.

Van der Baan, A. (2013). *Developing a design criterion for the shoreline response to multiple submerged breakwaters* (Master's thesis, Technical University Delft, Faculty of Civil Engineering and Geosciences, Department of Hydraulic Engineering, Delft, The Netherlands). Retrieved 30-03-2020, from `http://resolver.tudelft.nl/uuid:33e22ec6-447a-45a7-a23c-17647a76be43`

Whitford, D. J., & Thornton, E. B. (1993). Comparison of wind and wave forcing of longshore currents. *Continental Shelf Research*, *13*, 1205–1218.

Wiseman, W. J., Coleman, J., Gregory, A., Hsu, S., Short, A. D., Suhayda, J. N., ... Wright, L. (1973). Alaskan arctic coastal processes and morphology..

A. Python scripts

A.1 Linear Lagrange Interpolation

```
import numpy as np

def Interpolation(I, T, t, x_cor, y_cor, x_val, y_val, x_id_1, x_id_2,
y_id_1, y_id_2):
    '''
    Interpolant for interpolation in both time and space

    Inputs:
    I           3D array in which value has to be found, floats
    T           Time after which interpolation starts, units=hours, integer
    t           Time at which interpolation takes place, units=s, integer
    x_cor       2D array with grid x coordinates, units=km, floats
    y_cor       2D array with grid y coordinates, units=km, floats
    x_val       x coordinate of interpolation, units=m, float
    y_val       y coordinate of interpolation, units=m, float
    x_id_1      Corner point 1 in x grid of x_val, units=-, integer
    x_id_2      Corner point 2 in x grid of x_val, units=-, integer
    y_id_1      Corner point 1 y grid of y_val, units=-, integer
    y_id_2      Corner point 2 y grid of y_val, units=-, integer

    Outputs:
    L_t_x_I     Interpolated value, float

    x_id_1                                  x_id_2
    y_id_1  c3------------------------c4    y_id_1    x1,y2------------------------x2,y2
             |                        |                |       |                    |
             |                        |                |       |                    |
             |  o <-- (x_val,y_val)   |                |-------o--------------------|
             |                        |                |       |                    |
             |                        |                |       |                    |
    x_id_1  c1------------------------c2   x_id_2      x1,y1------------------------x2,y1
    y_id_2                                  y_id_2
    '''

    x1 = x_cor[y_id_1, x_id_1]*1000
    x2 = x_cor[y_id_1, x_id_2]*1000

    y1 = y_cor[y_id_2, x_id_1]*1000
    y2 = y_cor[y_id_1, x_id_1]*1000

    #Time interpolation
    T1 = T
    T2 = T+1

    t1 = T1*3600
    t2 = T2*3600

    array_t_1 = np.array((I[T1][y_id_2, x_id_1], I[T1][y_id_2, x_id_2],\
                          I[T1][y_id_1, x_id_1], I[T1][y_id_1, x_id_2]))
    array_t_2 = np.array((I[T2][y_id_2, x_id_1], I[T2][y_id_2, x_id_2],\
```

```
                                I[T2][y_id_1, x_id_1], I[T2][y_id_1, x_id_2]))

    L_t_I = np.zeros(4)

    L_t_I =  array_t_1*(t-t2)/(t1-t2) + \
                array_t_2*(t-t1)/(t2-t1)

    #Calculate the velocity in the interpolation point (x_val, y_val) at time step
#     s1 = (x2-x_val)*(y2-y_val)/((x2-x1)*(y2-y1))
#     s2 = (x1-x_val)*(y2-y_val)/((x1-x2)*(y2-y1))
#     s3 = (x2-x_val)*(y1-y_val)/((x2-x1)*(y1-y2))
#     s4 = (x1-x_val)*(y1-y_val)/((x1-x2)*(y1-y2))

    S = [(x2-x_val)*(y2-y_val)/((x2-x1)*(y2-y1)),
         (x1-x_val)*(y2-y_val)/((x1-x2)*(y2-y1)),
         (x2-x_val)*(y1-y_val)/((x2-x1)*(y1-y2)),
         (x1-x_val)*(y1-y_val)/((x1-x2)*(y1-y2))]

#     L_t_x_u = L_t_I_1*s1 + L_t_I_2*s2 + L_t_I_3*s3 + L_t_I_4*s4
    L_t_x_I = np.sum(L_t_I * S)

    return L_t_x_I
```

A.2 RK4

```
def transport_pattern_RK4(T0, dT, x_cor, y_cor, u_cor, v_cor, depth,
                          x_pos, y_pos, dt):
    '''
    Function that returns the transport vectors between T and T+1

    Inputs:
    T           Time at start of integration, units=hours, integer
    x_cor       2D array with grid x coordinates, units=km, floats
    y_cor       2D array with grid y coordinates, units=km, floats
    u_cor       3D array with grid u velocities in time, units=m/s
    v_cor       3D array with grid v velocities in time, units=m/s
    x_pos       Initial x coordinate, float, units=km, float
    y_pos       Initial y coordinate, float, units=km, float
    dt          Numerical time step Delta t, units=s, integer

    Outputs:
    x_vector    1D array of length dT*60/dt with x position per time step,
                units=km, floats
    y_vector    1D array of length dT*60/dt with y position per time step,
                units=km, floats
    u_vector    1D array of length dT*60/dt-1 with u velocities per time step,
                units=m/s, floats
    v_vector    1D array of length dT*60/dt-1 with v velocities per time step,
                units=m/s, floats
    h_vector    1D array of length dT*60/dt-1 with h velocities per time step,
                units=m/s, floats
    d_vector    1D array of length dT*60/dt with depth d per time step,
                units=m, floats
    '''
    #Convert to seconds
    t = T0*3600
    nt = np.int((dT*60)/dt)

    #Courant definition:
    #sigma = h * delta_t / delta_x <=1

    x_vector = np.zeros(nt)
    x_vector[0] = x_cor[int(y_pos), int(x_pos)]*1000
    y_vector = np.zeros(nt)
    y_vector[0] = y_cor[int(y_pos), int(x_pos)]*1000

    u_vector = np.zeros(nt-1)
    v_vector = np.zeros(nt-1)
    h_vector = np.zeros(nt-1)
    d_vector = np.zeros(nt)

    for i in range(len(x_vector) - 1):
        #####---k1 = h*f(ti, xi)
        x_k1 = x_vector[i]
        y_k1 = y_vector[i]
```

```
k1_x_id_1 = find_nearest_x(x_cor[int(y_pos),:]*1000, x_k1)[0]
k1_x_id_2 = find_nearest_x(x_cor[int(y_pos),:]*1000, x_k1)[1]
k1_y_id_1 = find_nearest_y(y_cor[:,int(x_pos)]*1000, y_k1)[0]
k1_y_id_2 = find_nearest_y(y_cor[:,int(x_pos)]*1000, y_k1)[1]

d_vector[i] = Interpolation(depth, T0, t, x_cor, y_cor, x_k1, y_k1,
        k1_x_id_1, k1_x_id_2, k1_y_id_1, k1_y_id_2)
k1_u = Interpolation(u_cor, T0, t, x_cor, y_cor,
        x_k1, y_k1, k1_x_id_1, k1_x_id_2, k1_y_id_1, k1_y_id_2)
k1_v = Interpolation(v_cor, T0, t, x_cor, y_cor, x_k1, y_k1,
        k1_x_id_1, k1_x_id_2, k1_y_id_1, k1_y_id_2)

k1_x = dt * k1_u
k1_y = dt * k1_v

#####--k2 = h*f(ti + h/2, xi + k1/2)
x_k2 = x_vector[i] + k1_x / 2
y_k2 = y_vector[i] + k1_y / 2
k2_x_id_1 = find_nearest_x(x_cor[int(y_pos),:]*1000, x_k2)[0]
k2_x_id_2 = find_nearest_x(x_cor[int(y_pos),:]*1000, x_k2)[1]
k2_y_id_1 = find_nearest_y(y_cor[:,int(x_pos)]*1000, y_k2)[0]
k2_y_id_2 = find_nearest_y(y_cor[:,int(x_pos)]*1000, y_k2)[1]

k2_u = Interpolation(u_cor, T0, t+dt/2, x_cor, y_cor, x_k2, y_k2,
        k2_x_id_1, k2_x_id_2, k2_y_id_1, k2_y_id_2)
k2_v = Interpolation(v_cor, T0, t+dt/2, x_cor, y_cor, x_k2, y_k2,
        k2_x_id_1, k2_x_id_2, k2_y_id_1, k2_y_id_2)
k2_x = dt * k2_u
k2_y = dt * k2_v

#####--k3 = h*f(ti + h/2, xi + k2/2)
x_k3 = x_vector[i] + k2_x / 2
y_k3 = y_vector[i] + k2_y / 2
k3_x_id_1 = find_nearest_x(x_cor[int(y_pos),:]*1000, x_k3)[0]
k3_x_id_2 = find_nearest_x(x_cor[int(y_pos),:]*1000, x_k3)[1]
k3_y_id_1 = find_nearest_y(y_cor[:,int(x_pos)]*1000, y_k3)[0]
k3_y_id_2 = find_nearest_y(y_cor[:,int(x_pos)]*1000, y_k3)[1]

k3_u = Interpolation(u_cor, T0, t+dt/2, x_cor, y_cor, x_k3, y_k3,
        k3_x_id_1, k3_x_id_2, k3_y_id_1, k3_y_id_2)
k3_v = Interpolation(v_cor, T0, t+dt/2, x_cor, y_cor, x_k3, y_k3,
        k3_x_id_1, k3_x_id_2, k3_y_id_1, k3_y_id_2)
k3_x = dt * k3_u
k3_y = dt * k3_v

#####--k4 = h*f(ti + h, xi + k3)
x_k4 = x_vector[i] + k3_x
y_k4 = y_vector[i] + k3_y
k4_x_id_1 = find_nearest_x(x_cor[int(y_pos),:]*1000, x_k4)[0]
k4_x_id_2 = find_nearest_x(x_cor[int(y_pos),:]*1000, x_k4)[1]
k4_y_id_1 = find_nearest_y(y_cor[:,int(x_pos)]*1000, y_k4)[0]
k4_y_id_2 = find_nearest_y(y_cor[:,int(x_pos)]*1000, y_k4)[1]

k4_u = Interpolation(u_cor, T0, t+dt, x_cor, y_cor, x_k4, y_k4,
```

```
            k4_x_id_1, k4_x_id_2, k4_y_id_1, k4_y_id_2)
        k4_v = Interpolation(v_cor, T0, t+dt, x_cor, y_cor, x_k4, y_k4,
            k4_x_id_1, k4_x_id_2, k4_y_id_1, k4_y_id_2)
        k4_y = dt * k4_v
        k4_x = dt * k4_u

        #####--xi+1 = xi + 1/6*(k1 + 2k2 + 2k3 + k4)
        x_vector[i + 1] = x_vector[i] + 1/6 * (k1_x + 2 * k2_x + 2 * k3_x + k4_x)
        y_vector[i + 1] = y_vector[i] + 1/6 * (k1_y + 2 * k2_y + 2 * k3_y + k4_y)

        u_vector[i] = 1/6 * (k1_u + 2 * k2_u + 2 * k3_u + k4_u)
        v_vector[i] = 1/6 * (k1_v + 2 * k2_v + 2 * k3_v + k4_v)
        h_vector[i] = np.sqrt((u_vector[i])**2 + (v_vector[i])**2)

        t += dt

    x_id_1 = find_nearest_x(x_cor[int(y_pos),:]*1000, x_vector[-1])[0]
    x_id_2 = find_nearest_x(x_cor[int(y_pos),:]*1000, x_vector[-1])[1]
    y_id_1 = find_nearest_y(y_cor[:,int(x_pos)]*1000, y_vector[-1])[0]
    y_id_2 = find_nearest_y(y_cor[:,int(x_pos)]*1000, y_vector[-1])[1]
    d_vector[-1] = Interpolation(depth, int(T0), t+dT*60, x_cor, y_cor,
            x_vector[-1], y_vector[-1], x_id_1, x_id_2, y_id_1, y_id_2)

    x_vector = x_vector/1000
    y_vector = y_vector/1000
    return x_vector, y_vector, u_vector, v_vector, h_vector, d_vector
```

A.3 Find Nearest Functions

```
def find_nearest_x(array, value):
    '''
    Finds two x grid points in between which value lies

    Input:
    array    1D array with x coordinates
    value    Value around which x grid coordinates are to be found, float

    Output:
    idx1     x grid coordinate of left hand corner points, integer
    idx2     x grid coordinate of right hand corner points, integer
    '''
    array = np.copy(array)
    idx1 = 0
    idx2 = 0

    idx = np.nanargmin(np.abs(array - value))

    if array[idx] > value:
        idx1 = idx - 1
        idx2 = idx

    elif array[idx] < value:
        idx1 = idx
        idx2 = idx + 1

    elif array[idx] == value:
        idx1 = idx - 1
        idx2 = idx

    return idx1, idx2

def find_nearest_y(array, value):
    '''
    Finds two y grid points in between which value lies

    Input:
    array    1D array with y coordinates
    value    Value around which y grid coordinates are to be found, float

    Output:
    idy1     y grid coordinate of upper corner points, integer
    idy2     y grid coordinate of lower corner points, integer
    '''
    array = np.copy(array)
    idy1 = 0
    idy2 = 0

    idy = np.nanargmin(np.abs(array - value))
```

```
if array[idy] > value:
    idy1 = idy
    idy2 = idy + 1

elif array[idy] < value:
    idy1 = idy - 1
    idy2 = idy

elif array[idy] == value:
    idy1 = idy
    idy2 = idy + 1

return idy1, idy2
```

B. **Analysis, Regular Tide**

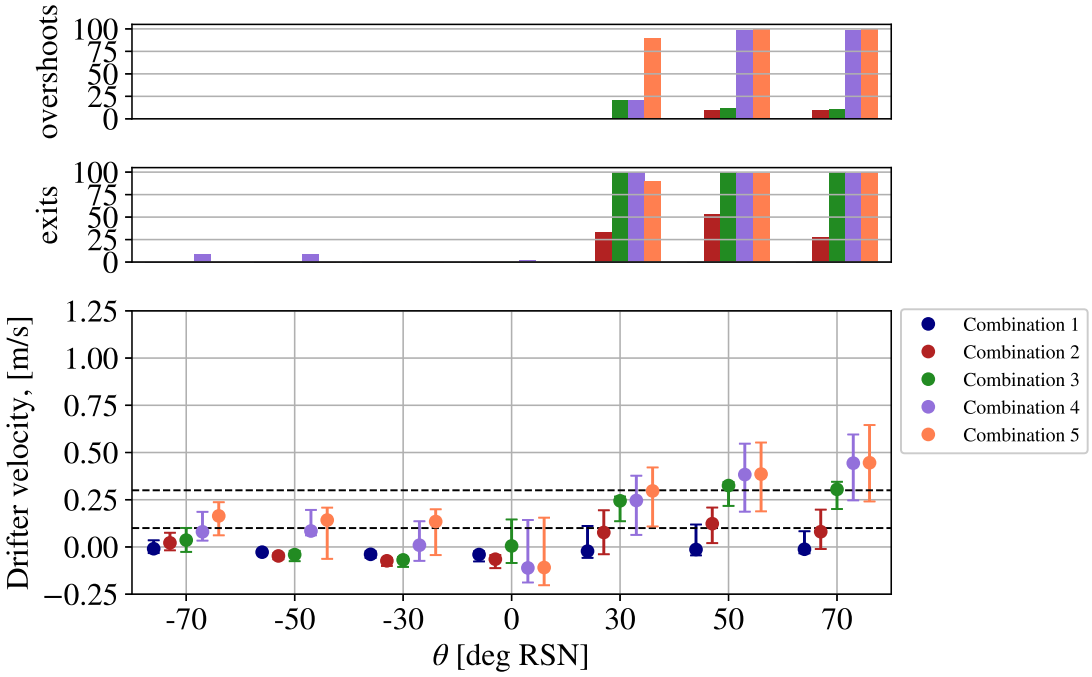

Figure B.1: Overshoots (upper panel), Exits (middle panel) and velocities at the harbour mole vicinity during high water minus two hours.

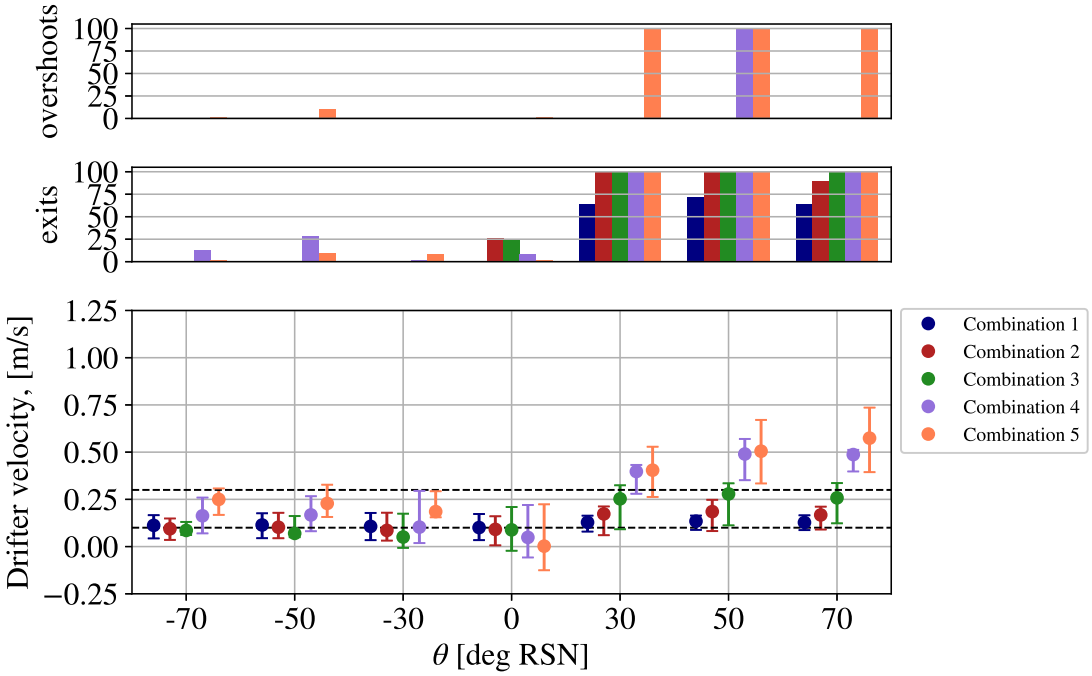

Figure B.2: Overshoots (upper panel), Exits (middle panel) and velocities at the harbour mole vicinity during high water.

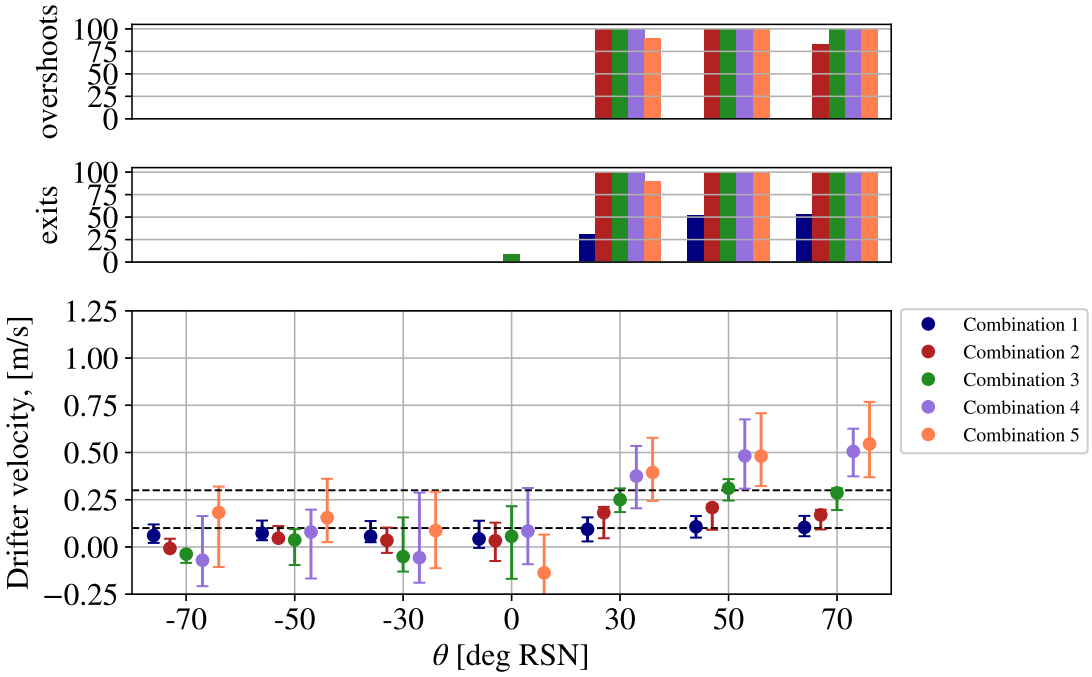

Figure B.3: Overshoots (upper panel), Exits (middle panel) and velocities at the harbour mole vicinity during high water plus two hours.

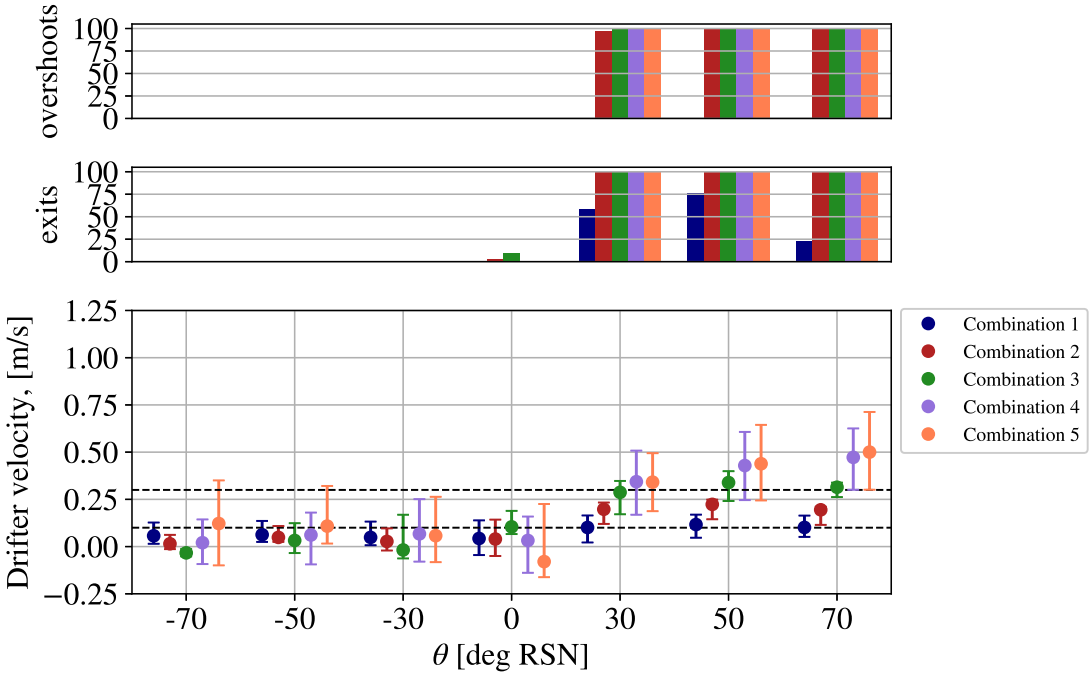

Figure B.4: Overshoots (upper panel), Exits (middle panel) and velocities at the harbour mole vicinity during mean water level.

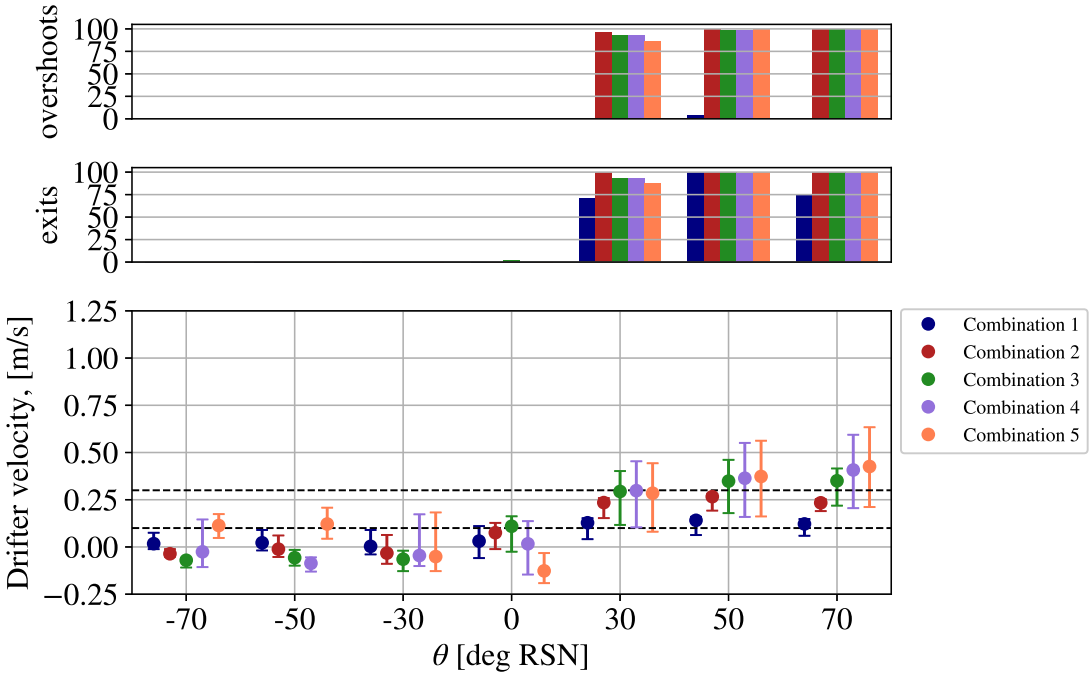

Figure B.5: Overshoots (upper panel), Exits (middle panel) and velocities at the harbour mole vicinity during low water minus two hours.

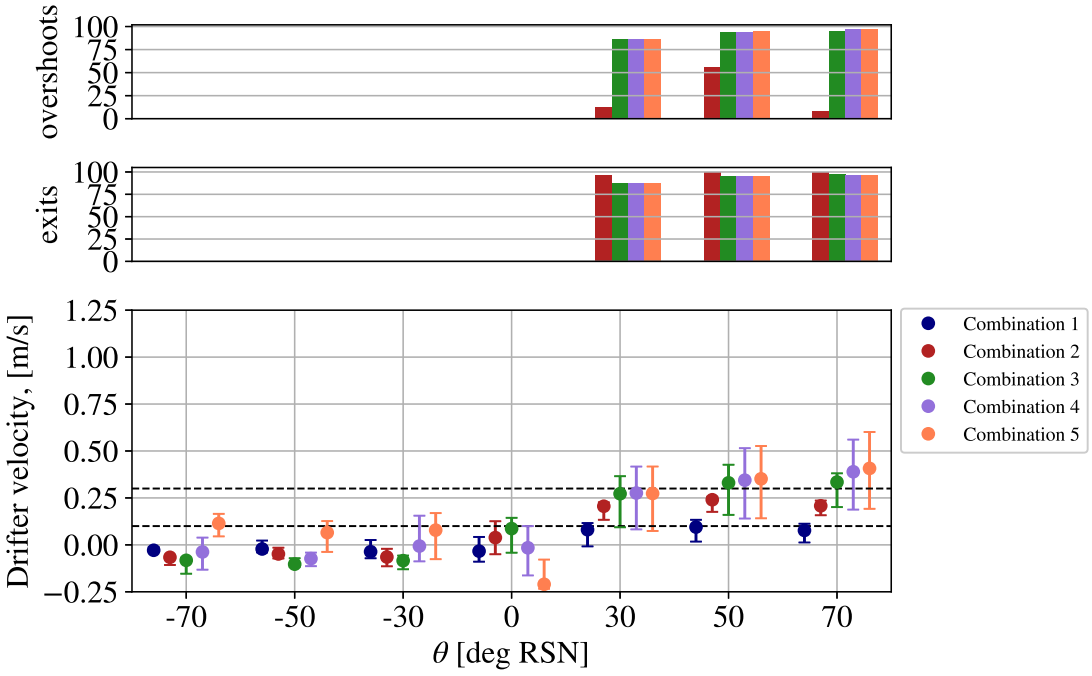

Figure B.6: Overshoots (upper panel), Exits (middle panel) and velocities at the harbour mole vicinity during low water.

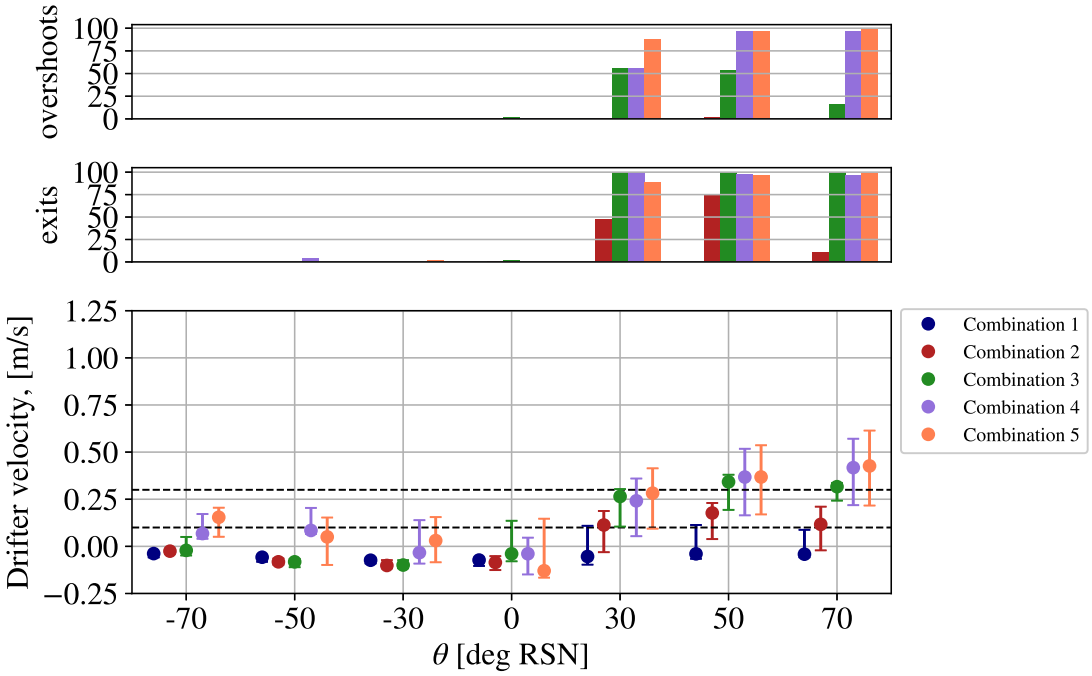

Figure B.7: Overshoots (upper panel), Exits (middle panel) and velocities at the harbour mole vicinity during low water plus two hours.

B.1 Drifter velocity boxplots for a regular tide for all cases during wind and waves from 30-70 deg RSN

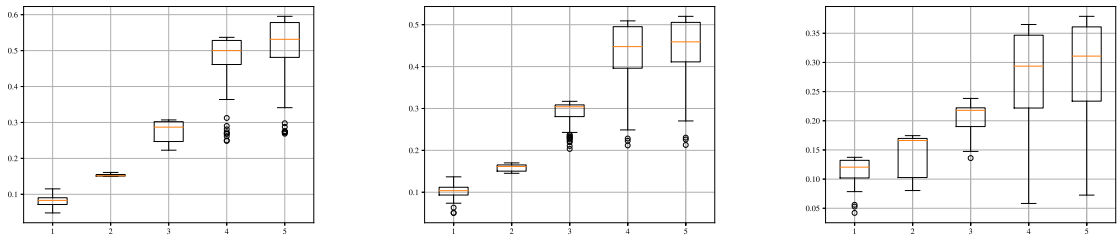

(a) (b) (c)

Figure B.8: T_{high}-2hr. a) 70 deg RSN. b) 50 deg RSN. c) 30 deg RSN.

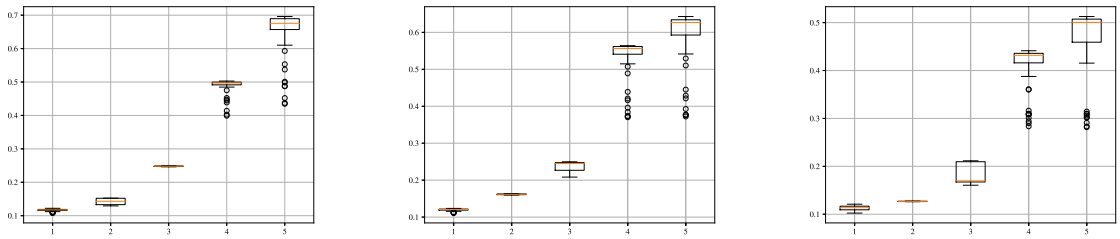

(a) (b) (c)

Figure B.9: T_{high}-2hr. a) 70 deg RSN. b) 50 deg RSN. c) 30 deg RSN.

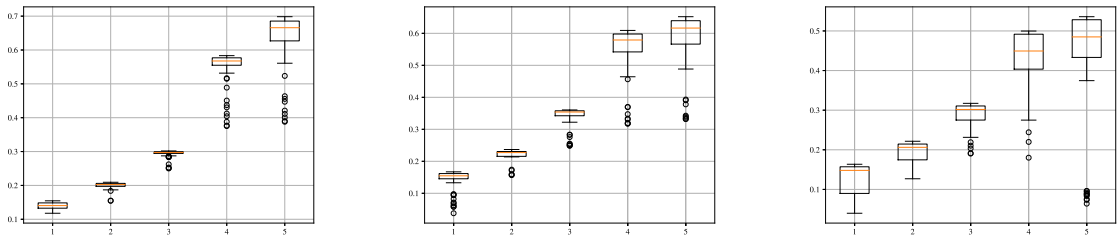

(a) (b) (c)

Figure B.10: T_{high}-2hr. a) 70 deg RSN. b) 50 deg RSN. c) 30 deg RSN.

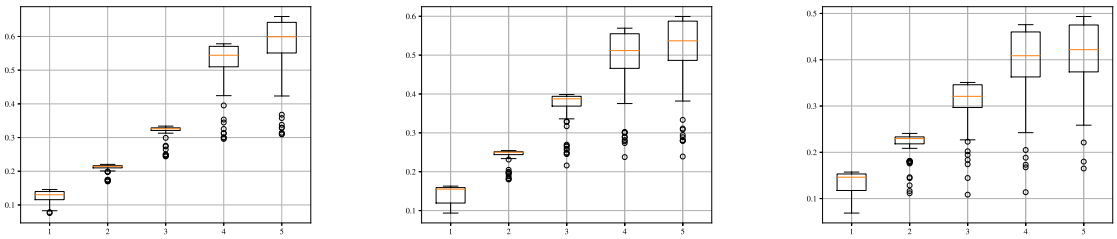

(a) (b) (c)

Figure B.11: T_{high}-2hr. a) 70 deg RSN. b) 50 deg RSN. c) 30 deg RSN.

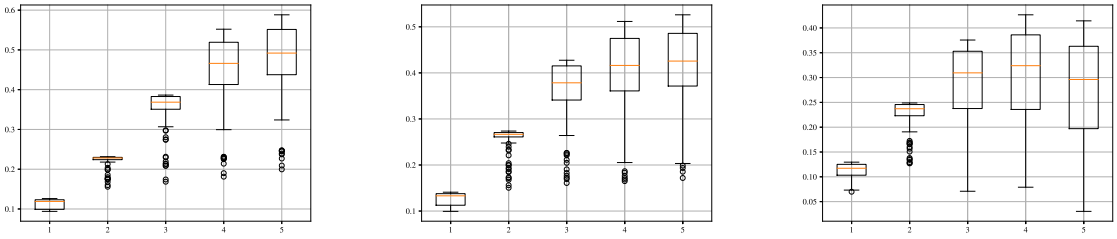

(a) (b) (c)

Figure B.12: T_{high}-2hr. a) 70 deg RSN. b) 50 deg RSN. c) 30 deg RSN.

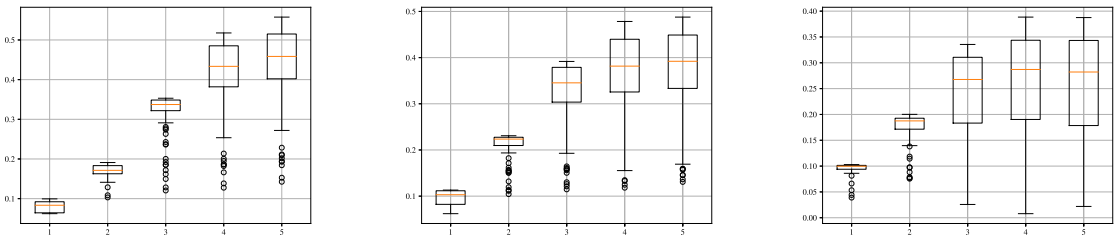

(a) (b) (c)

Figure B.13: T_{high}-2hr. a) 70 deg RSN. b) 50 deg RSN. c) 30 deg RSN.

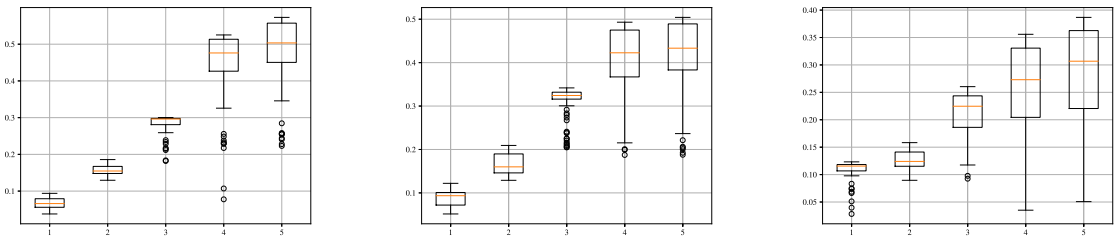

(a) (b) (c)

Figure B.14: T_{high}-2hr. a) 70 deg RSN. b) 50 deg RSN. c) 30 deg RSN.

C. **Analysis, Neap Tide**

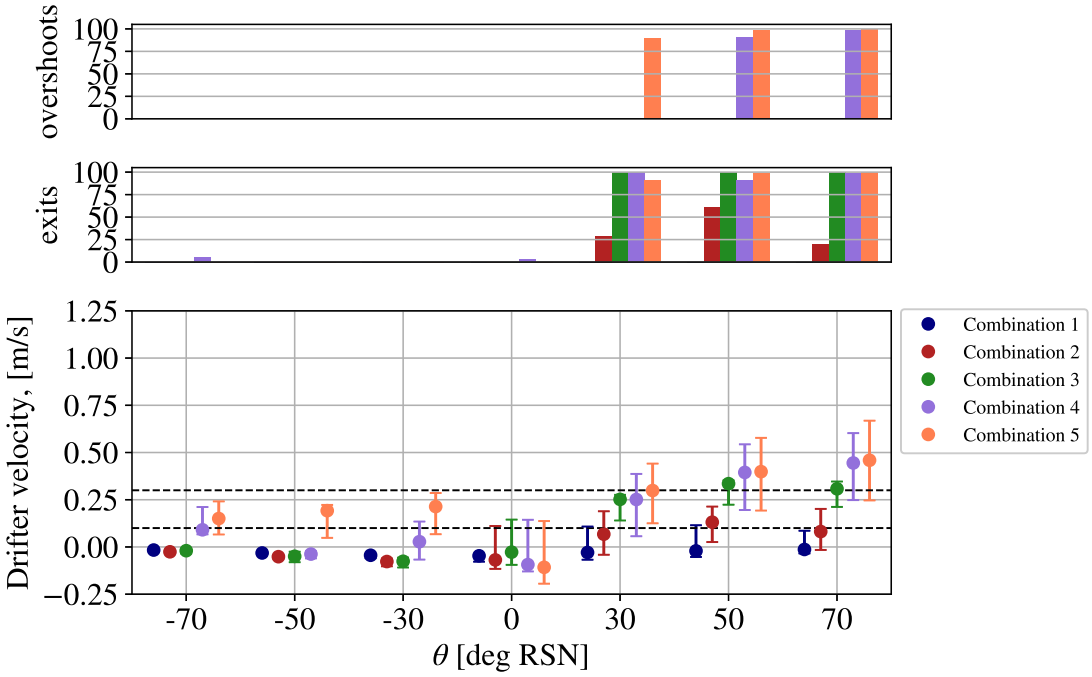

Figure C.1: Overshoots (upper panel), Exits (middle panel) and velocities at the harbour mole vicinity during high water minus two hours.

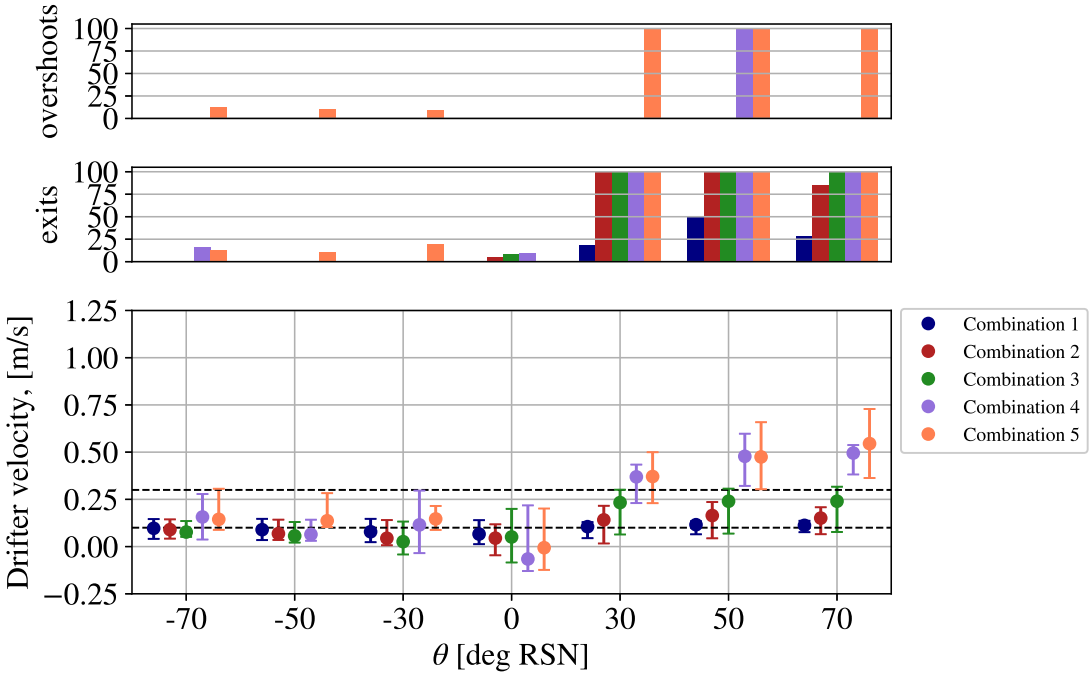

Figure C.2: Overshoots (upper panel), Exits (middle panel) and velocities at the harbour mole vicinity during high water.

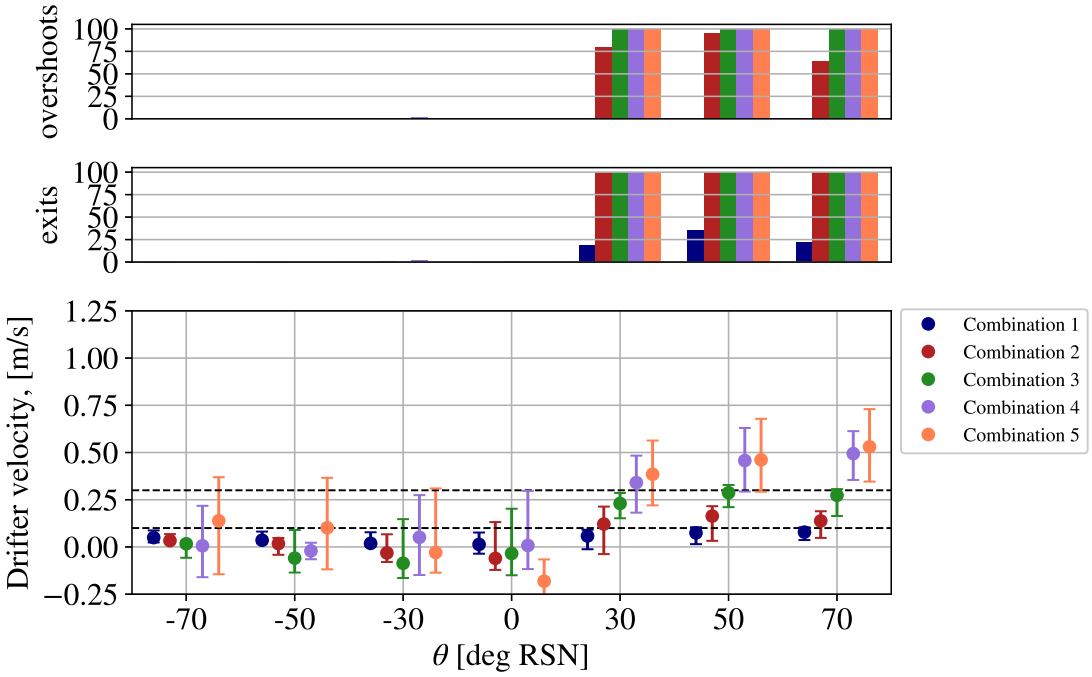

Figure C.3: Overshoots (upper panel), Exits (middle panel) and velocities at the harbour mole vicinity during high water plus two hours.

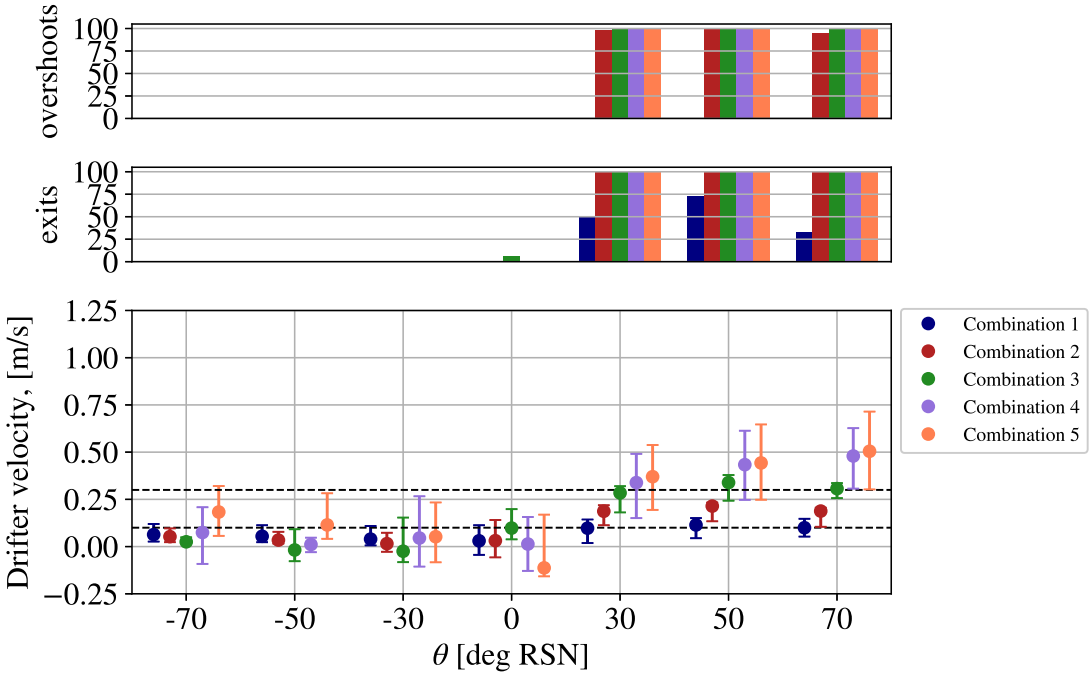

Figure C.4: Overshoots (upper panel), Exits (middle panel) and velocities at the harbour mole vicinity during mean water level.

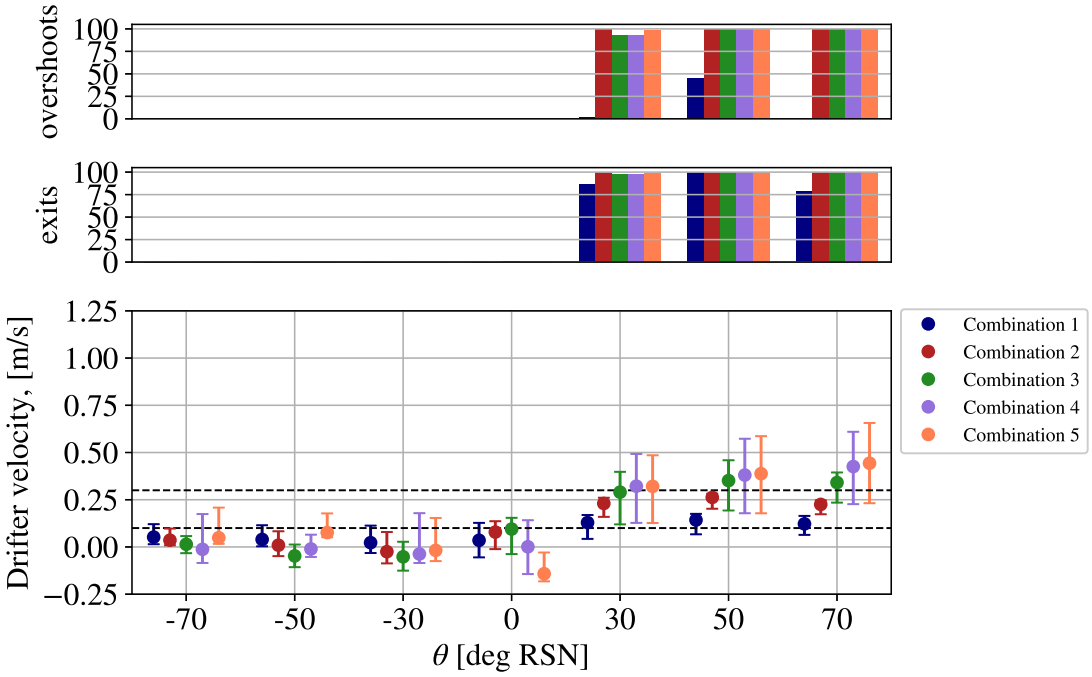

Figure C.5: Overshoots (upper panel), Exits (middle panel) and velocities at the harbour mole vicinity during low water minus two hours.

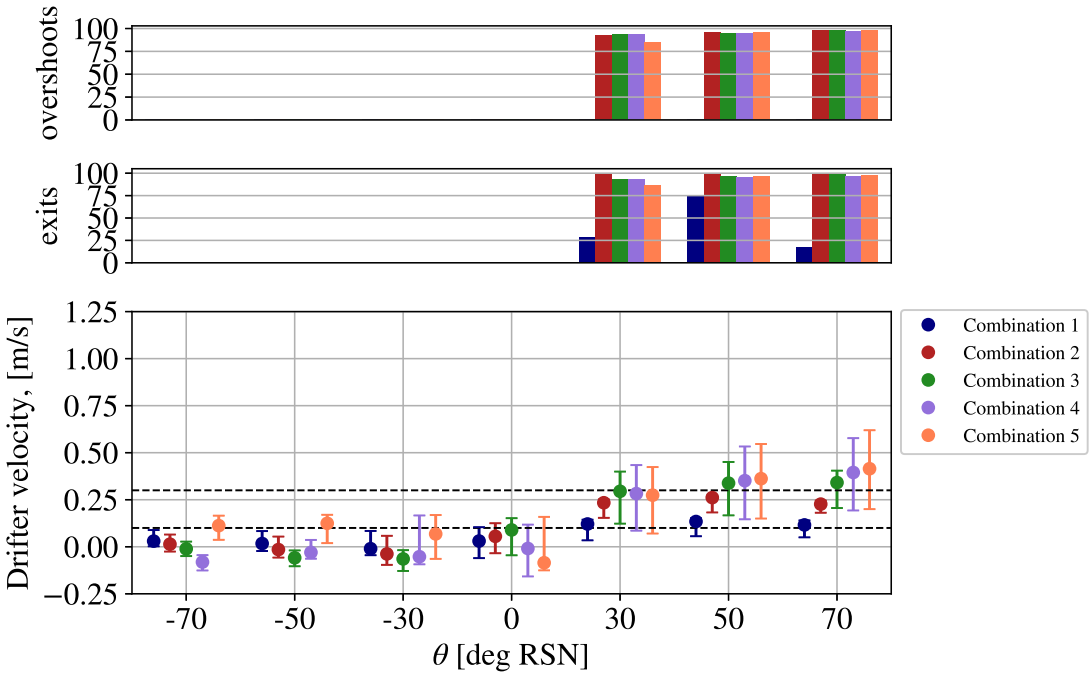

Figure C.6: Overshoots (upper panel), Exits (middle panel) and velocities at the harbour mole vicinity during low water.

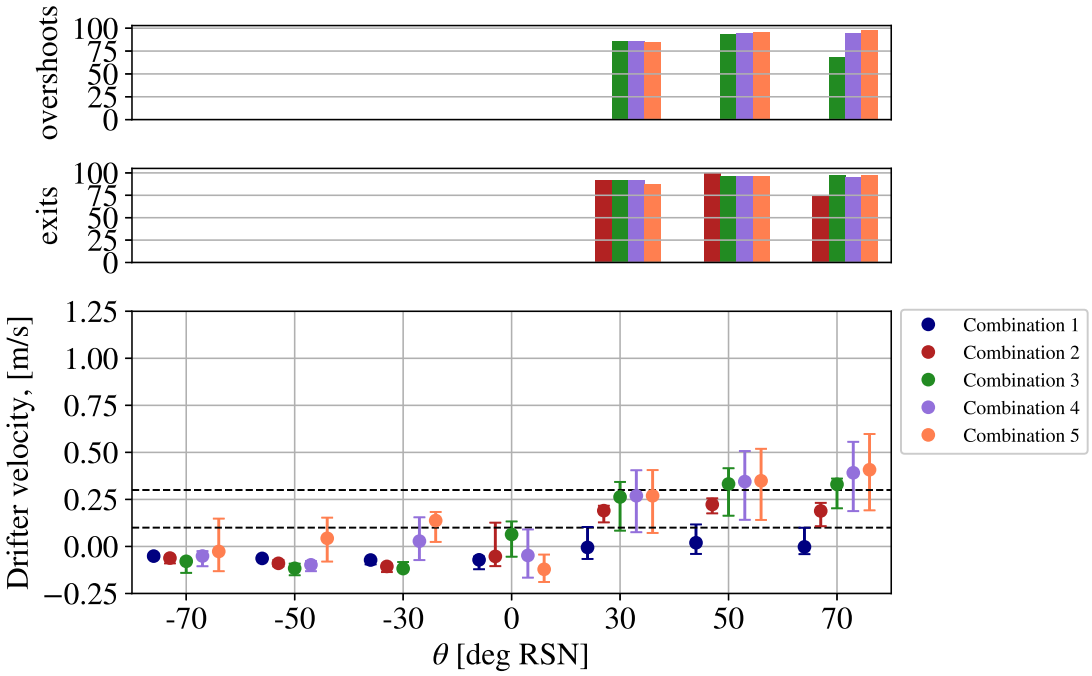

Figure C.7: Overshoots (upper panel), Exits (middle panel) and velocities at the harbour mole vicinity during low water plus two hours.

C.1 Drifter velocity boxplots for a Spring spring for all cases during wind and waves from 30-70 deg RSN

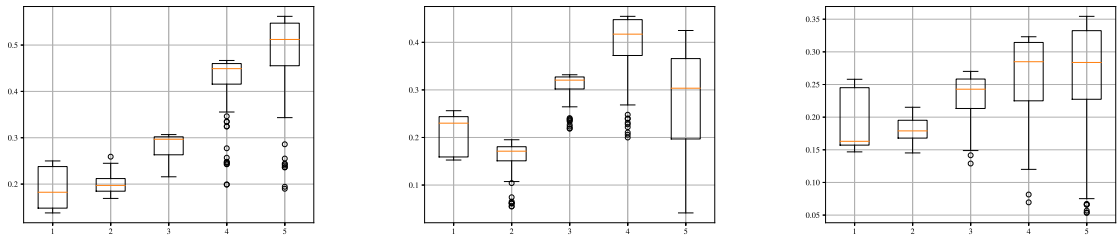

(a) (b) (c)

Figure C.8: T_{high}-2hr. a) 70 deg RSN. b) 50 deg RSN. c) 30 deg RSN.

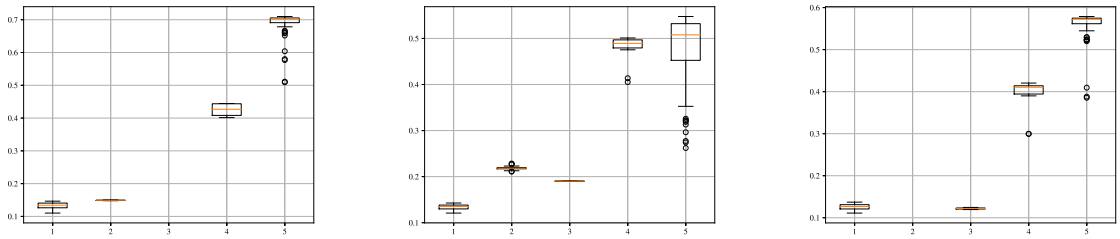

(a) (b) (c)

Figure C.9: T_{high}-2hr. a) 70 deg RSN. b) 50 deg RSN. c) 30 deg RSN.

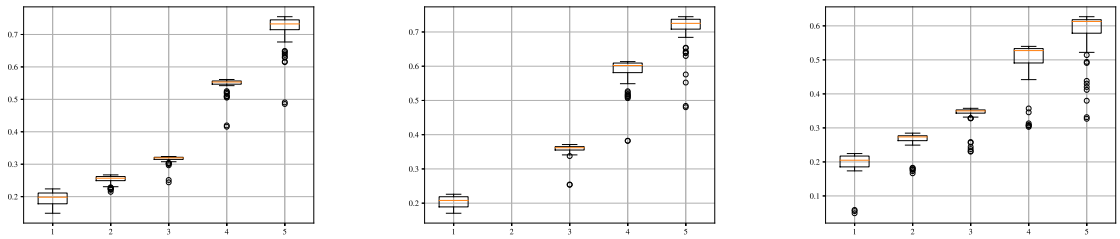

(a) (b) (c)

Figure C.10: T_{high}-2hr. a) 70 deg RSN. b) 50 deg RSN. c) 30 deg RSN.

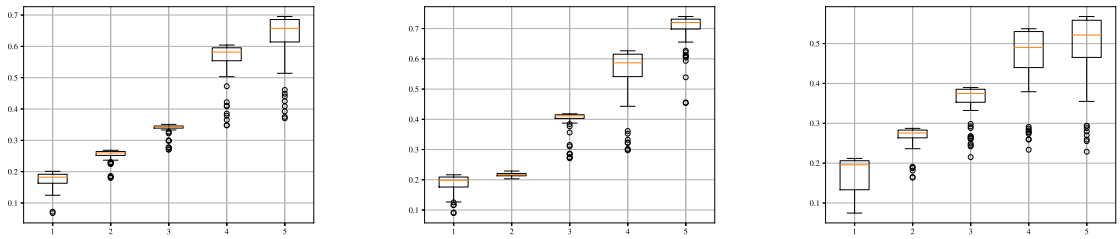

(a) (b) (c)

Figure C.11: T_{high}-2hr. a) 70 deg RSN. b) 50 deg RSN. c) 30 deg RSN.

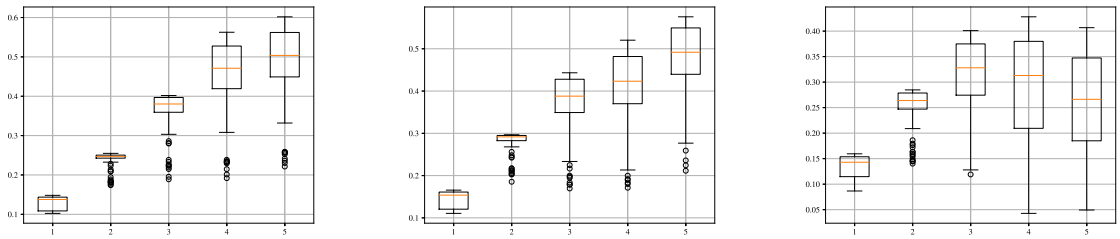

(a) (b) (c)

Figure C.12: T_{high}-2hr. a) 70 deg RSN. b) 50 deg RSN. c) 30 deg RSN.

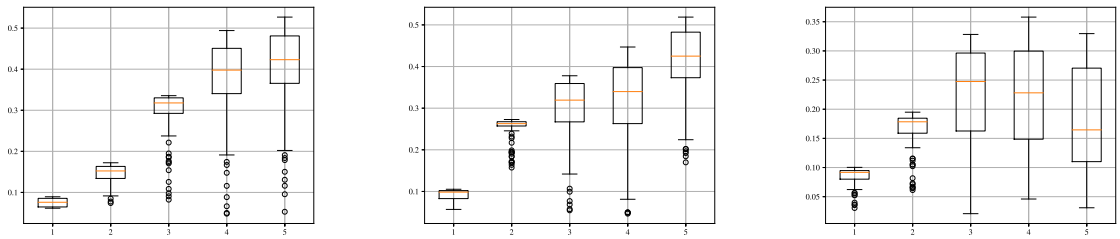

(a) (b) (c)

Figure C.13: T_{high}-2hr. a) 70 deg RSN. b) 50 deg RSN. c) 30 deg RSN.

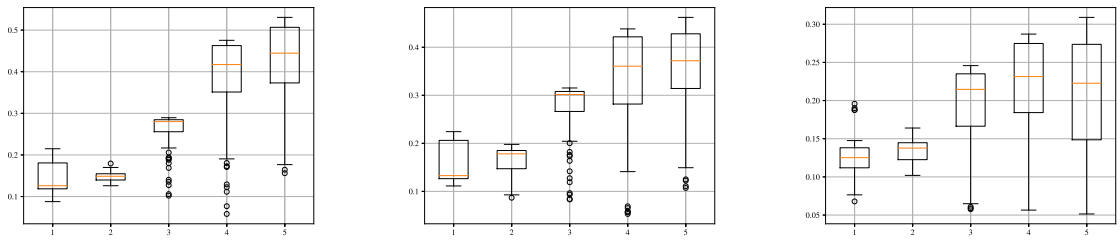

(a) (b) (c)

Figure C.14: T_{high}-2hr. a) 70 deg RSN. b) 50 deg RSN. c) 30 deg RSN.

D. **Analysis, Spring Tide**

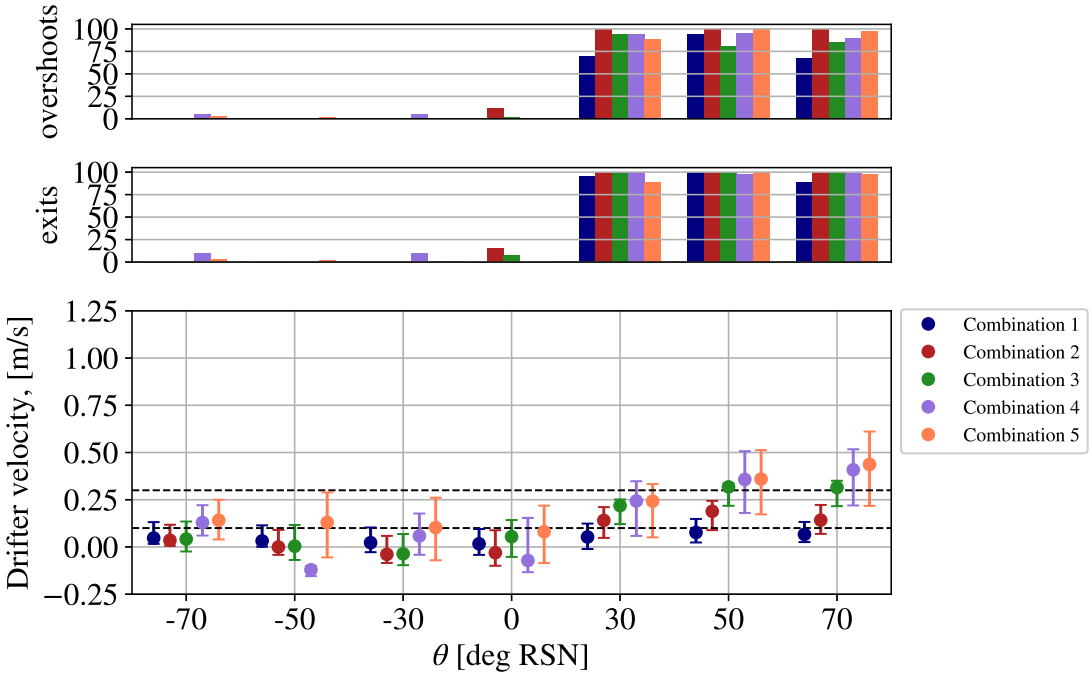

Figure D.1: Overshoots (upper panel), Exits (middle panel) and velocities at the harbour mole vicinity during high water minus two hours.

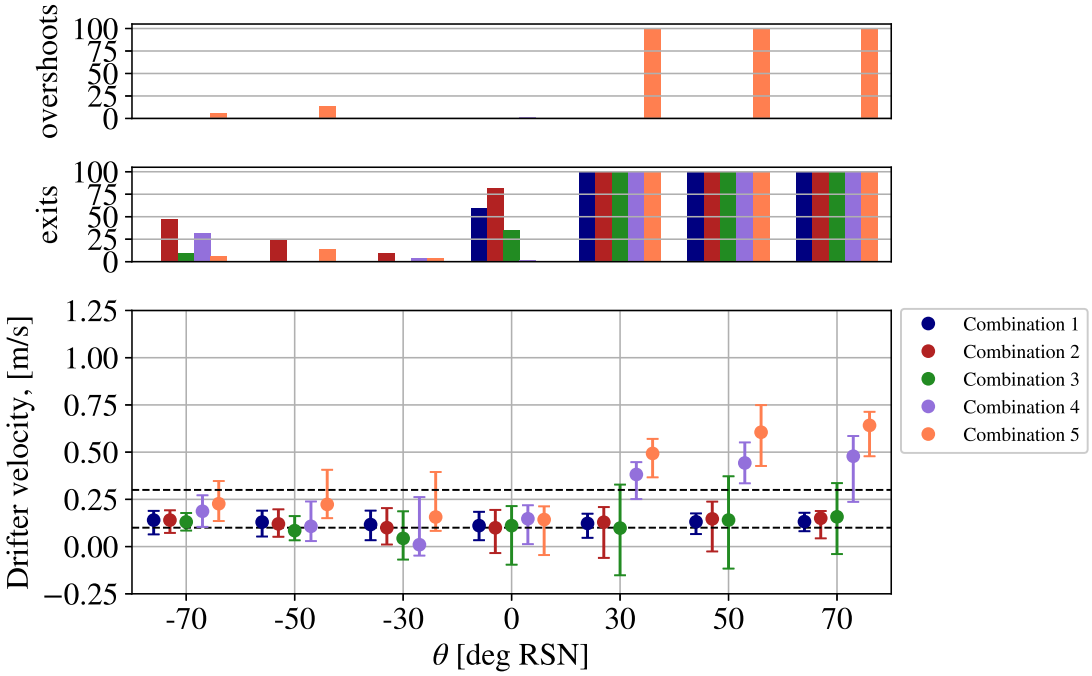

Figure D.2: Overshoots (upper panel), Exits (middle panel) and velocities at the harbour mole vicinity during high water.

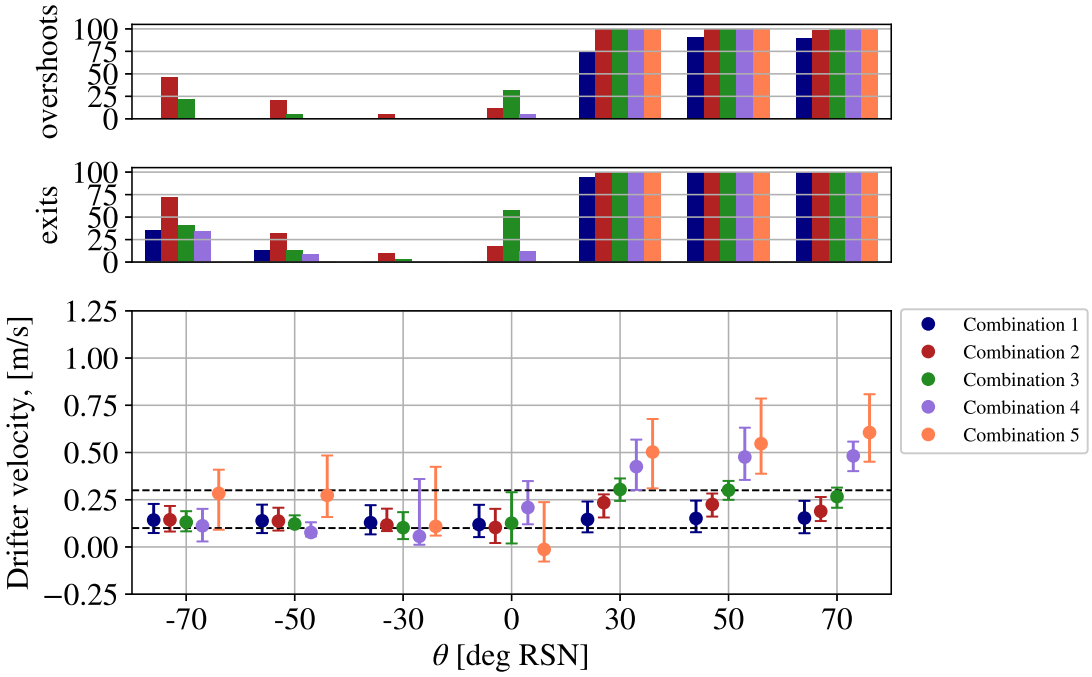

Figure D.3: Overshoots (upper panel), Exits (middle panel) and velocities at the harbour mole vicinity during high water plus two hours.

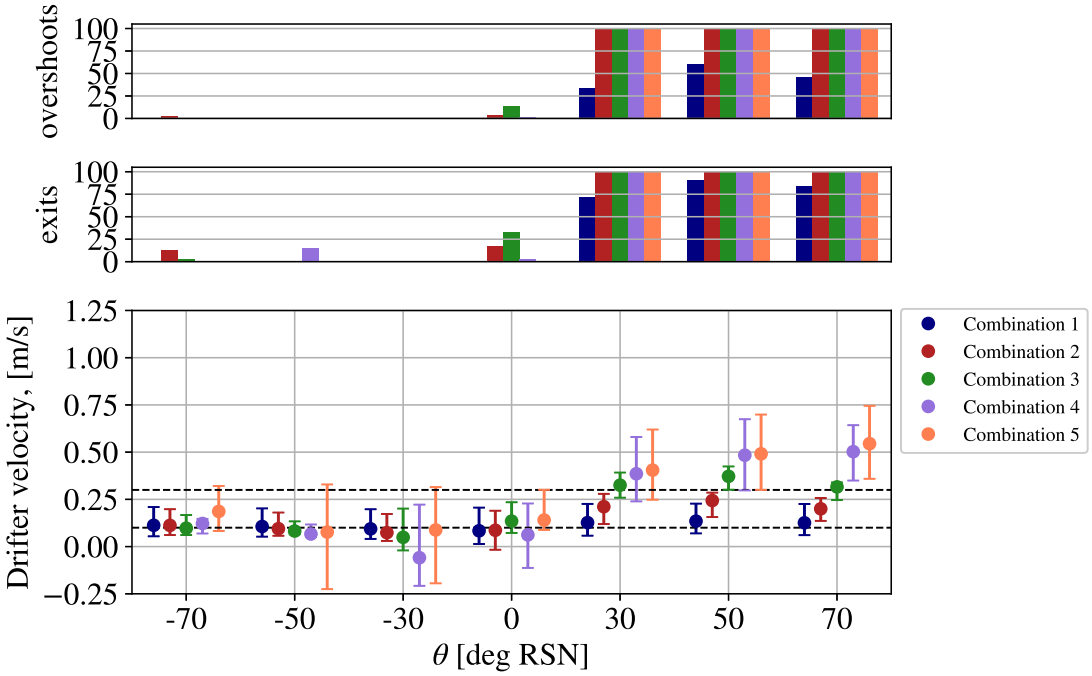

Figure D.4: Overshoots (upper panel), Exits (middle panel) and velocities at the harbour mole vicinity during mean water level.

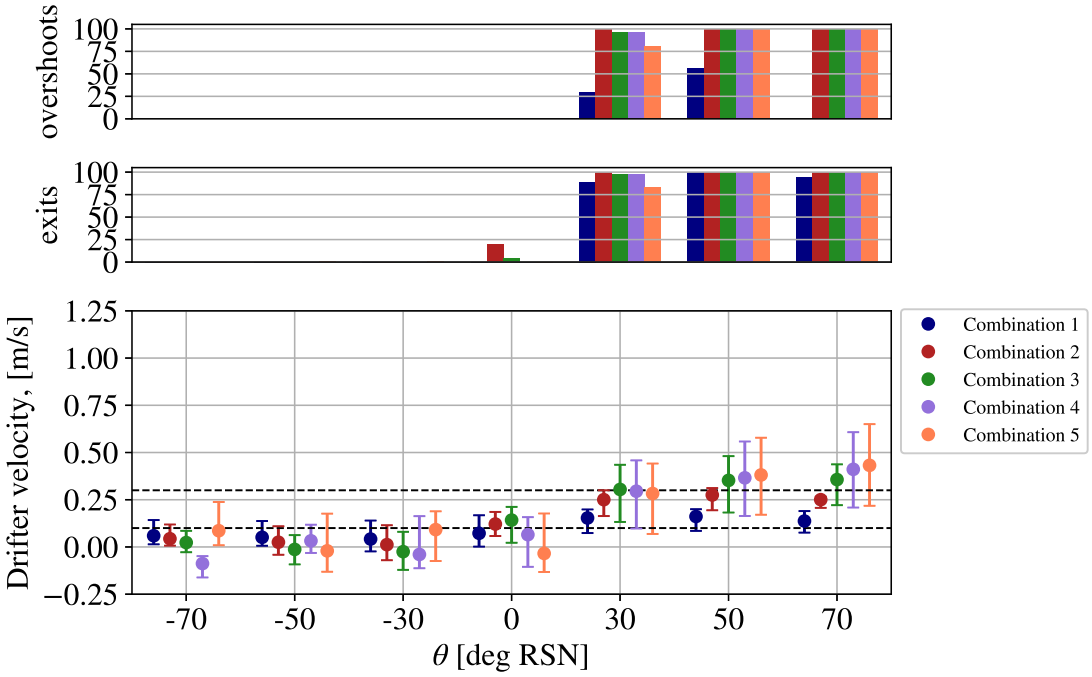

Figure D.5: Overshoots (upper panel), Exits (middle panel) and velocities at the harbour mole vicinity during low water minus two hours.

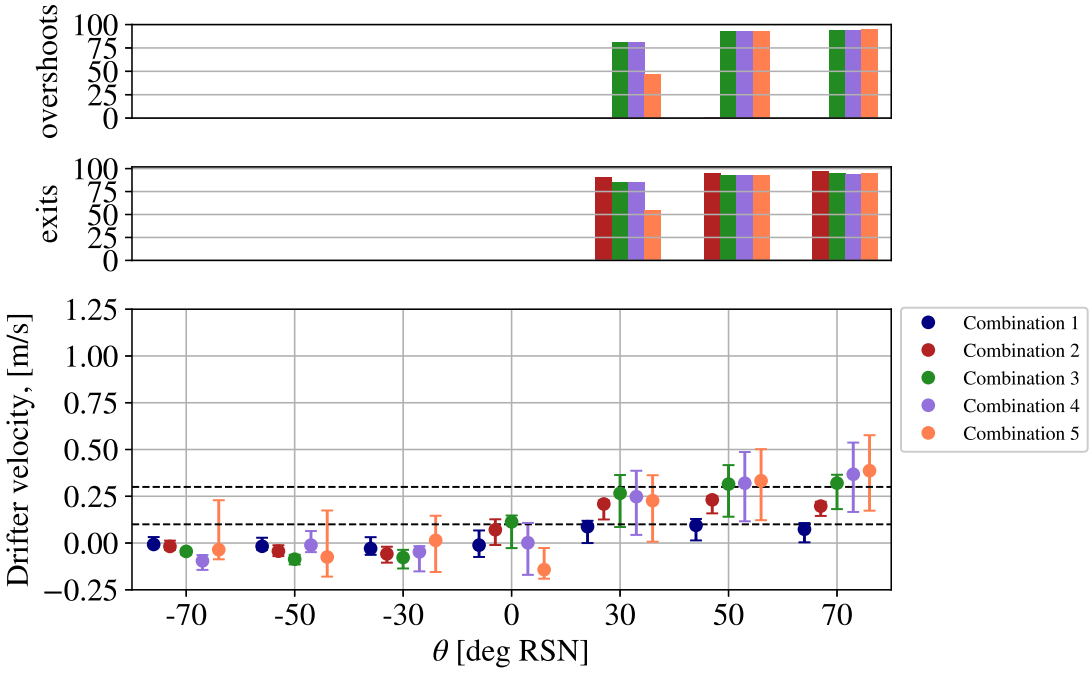

Figure D.6: Overshoots (upper panel), Exits (middle panel) and velocities at the harbour mole vicinity during low water.

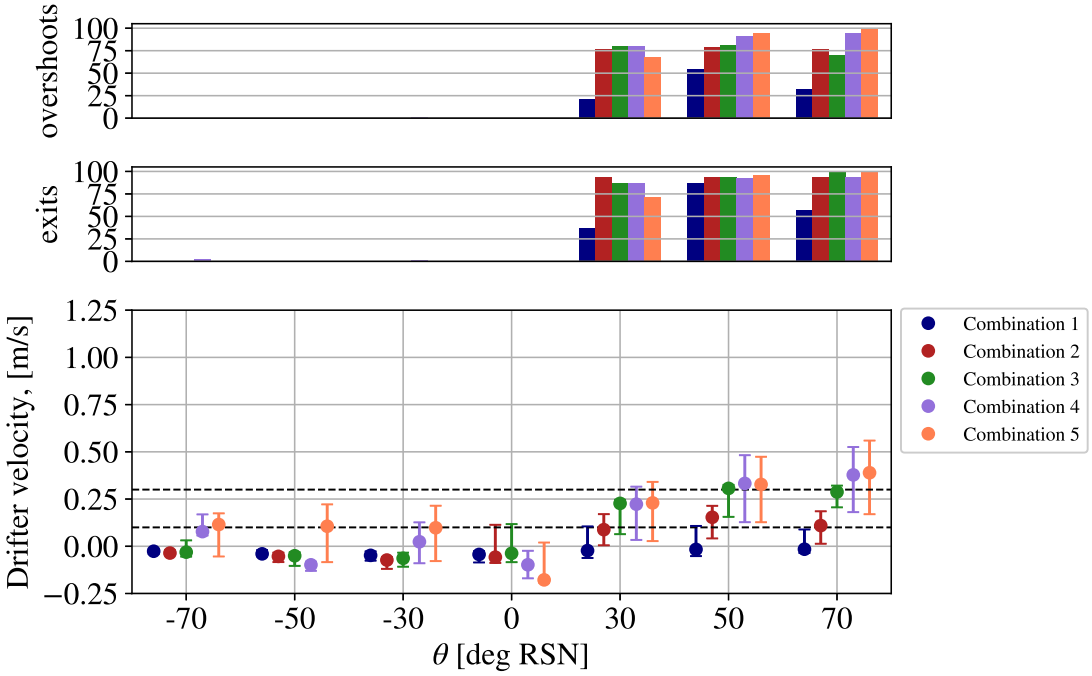

Figure D.7: Overshoots (upper panel), Exits (middle panel) and velocities at the harbour mole vicinity during low water plus two hours.